




Universitat Autònoma de Barcelona

ADVERTIMENT. L'accés als continguts d'aquesta tesi queda condicionat a l'acceptació de les condicions d'ús establertes per la següent llicència Creative Commons:  http://cat.creativecommons.org/?page_id=184

ADVERTENCIA. El acceso a los contenidos de esta tesis queda condicionado a la aceptación de las condiciones de uso establecidas por la siguiente licencia Creative Commons:  <http://es.creativecommons.org/blog/licencias/>

WARNING. The access to the contents of this doctoral thesis it is limited to the acceptance of the use conditions set by the following Creative Commons license:  <https://creativecommons.org/licenses/?lang=en>



**Universitat Autònoma
de Barcelona**

PhD THESIS

**Synthesis of defect free
 $\text{YBa}_2\text{Cu}_3\text{O}_{7-x}$ films over $1\mu\text{m}$
by CSD using Inkjet Printing**

Bohores VILLAREJO REINA

2018

Supervised by

Teresa PUIG

Xavier OBRADORS

Tutor: Jordi GARCÍA-ANTÓN



*Material Science PhD program
Chemistry department*



Teresa Puig i Molina, Científica Titular a l'Institut de Ciència de Materials de Barcelona, Xavier Obradors Berenguer, Científic Titular a l'Institut de Ciència de Materials de Barcelona, i Jordi García-Antón, Professor a la Universitat Autònoma de Barcelona

CERTIFIQUEN

que Bohores Villarejo Reina, Llicenciat en Química, ha dut a terme sota la seva direcció el treball que porta per títol "Synthesis of defect free $\text{YBa}_2\text{Cu}_3\text{O}_{7-x}$ films over $1\mu\text{m}$ by CSD using Inkjet Printing" i queda recollit en aquesta memòria per optar al Grau de Doctor.

I per a que així consti, signen el present certificat.

Prof. Teresa Puig Prof. Xavier Obradors Dr. Jordi García-Antón

Bohores Villarejo Reina

Bellaterra, Juny 2018

Acknowledgements

I would like to thank all the people who made this work possible through their dedication, advices and friendship.

First of all, I want to thank to my supervisors, Prof. Teresa Puig and Prof. Xavier Obradors to give me the opportunity to be a part on this project and to help me to grow up as a scientist. Thanks to you I consider myself ready to tackle any challenge.

Thanks to the thick film team, Dr. Cornelia Pop and Dr. Flavio Pino, for their work and dedication, who made this thesis possible.

To Dr. Marta Vilardell and these many hours of discussion about scientific and especially the not-so-scientific stuff.

To my PhD colleagues and the good vibes that only such an amazing squad can generate.

Special thanks to Dr. Pere Roura and Dr. Jordi Farjas from the GRMT group, UdG, for their hard work and expertise on the thermal analysis characterization of the YBCO process.

Thanks to Dr. Susagna Ricart and Dr. Mar Tristany for their advices, specially those on the chemical field.

To Mariona de Palau for all the support provided on the lab.

To all the SUMAN group, for the teamwork on this leading project.

To the Nanoquim platform for the patience demonstrated and their professionalism.

To the ICMAB technical staff for providing all the necessary support required during this work.

I want to acknowledge Kao Chimigraf company for providing the varnishes for the precursor ink.

To the funding received from EU-FP7 NMP-LA-2012-280432 EUROTAPES project, MP1201 Cost action, RTC-2015-3640-3 SUPERINKS project and MAT2014-

51778-C2-1-R national project.

Vull enviar un agraïment a tota la gent de fora de l'ambient de treball, que a la seva manera han fet que aquest treball fós possible, inclosos els amics i els companys d'equip.

Per últim, un agraïment molt especial a la meva família i a la meva parella, que han patit aquesta tesi pràcticament tant com jo.

A tots vosaltres moltes gràcies!

To all of you, thank you very much!

Contents

1	Introduction	1
1.1	The superconductivity phenomenon	1
1.1.1	Coated conductor architecture	3
1.2	Chemical Solution Deposition (CSD)	5
1.2.1	YBCO precursor solution design	6
1.2.2	Precursor solution deposition	7
1.2.3	Pyrolysis process for thick YBCO films	8
1.2.4	Nucleation and growth of YBCO film	11
2	Experimental procedure	15
2.1	Ink design and preparation	15
2.2	Solution characterization	18
2.2.1	Ink rheology characterization	18
2.2.2	Water content determination	20
2.3	Inkjet printing, drop generation and deposition	20
2.3.1	Drop pitch	20
2.3.2	Drop monitoring	21
2.3.3	Meniscus control	22
2.4	Substrate type and treatment	22
2.4.1	Single crystal substrate	23
2.4.2	Buffered metallic substrate	23
2.5	Pyrolysis process analysis	23
2.5.1	Tubular furnaces	24
2.5.2	Optical microscopy	24
2.5.3	Pyrolyzer	24
2.5.4	Mass and heat evolution	26
2.5.5	Thickness measurements	29
2.5.6	Mechanical properties testing	31
2.5.7	Film morphology analysis	34
2.5.8	Film structure characterization	35
2.6	Superconducting properties characterization	36

2.6.1	Superconducting Quantum Interference Device (SQUID) magnetometer	36
2.6.2	Transport measurements	37
3	Ink design and deposition by Inkjet printing	39
3.1	Principles of ink formulation and deposition	39
3.2	Drop formation	40
3.2.1	The piezoelectric printhead	41
3.2.2	Ink properties effect on drop ejection and deposition	42
3.2.3	Fluid dynamics	44
3.3	Theoretical parameters of the liquid-substrate interaction	46
3.3.1	Drop impact	47
3.3.2	Wetting	48
3.3.3	Liquid redistribution: Coffee stain effect	49
3.4	Organometallic YBCO ink deposition	50
3.4.1	Ink design	52
3.4.2	Solution deposition study with inks optimized for spin coating deposition	53
3.4.3	4B ink composition tuning for thick films deposition by inkjet printing	55
3.4.4	Ink composition change to improve liquid distribution homogeneity	59
3.5	Drop merging study	62
3.5.1	Merging study on X axis: Merging of drops	62
3.5.2	Merging study on Y axis: Merging of lines	63
3.5.3	Drop merging for 4C ink composition	66
3.6	Deposition parameters optimization	67
3.6.1	Waveform effect on the drop volume and drop speed	68
3.6.2	Substrate effect on the deposition process	72
3.7	Film solvent drying	73
3.8	Chapter summary and conclusions	74
4	Physico-chemical analysis of the pyrolysis process	79
4.1	Introduction to the pyrolysis process	79
4.2	Gel shrinkage and stress generation	81
4.2.1	Tensile stress release	82

4.2.2	Compressive stress: Film buckling	82
4.3	Pyrolyzed film requirements	83
4.4	Film morphology analysis during the pyrolysis process	84
4.4.1	Previous knowledge on thick films	85
4.4.2	Pyrolysis of thick films deposited with 4C ink	86
4.4.3	Morphology study of thick films deposited with 4C ink	87
4.4.4	Influence of the solution formulation on the pyrolysis	93
4.4.5	Summary of the morphology analysis	99
4.5	Mass and heat flow evolution study during the pyrolysis	102
4.5.1	In situ mass evolution analysis	102
4.5.2	Heat flow analysis	107
4.5.3	Released gas compositional study	108
4.5.4	Infrared spectroscopy analysis of the pyrolysis process	113
4.5.5	Summary of mass and heat evolution study results	118
4.6	In situ study on the thickness evolution during pyrolysis	120
4.6.1	Thickness evolution during pyrolysis	122
4.6.2	Film density evolution during pyrolysis	125
4.6.3	Thickness evolution in isotherm regime	128
4.7	Film mechanical properties	131
4.7.1	Film mechanical testing by nanoindentation	131
4.7.2	In situ mechanical properties study during pyrolysis	134
4.8	Results on the non cracked thick films synthesis	142
4.8.1	Thickness homogeneity effect on the film cracking	143
4.9	Chapter summary and conclusions	145
5	Reproducible inkjet printing of homogeneous YBCO thick films	151
5.1	Homogeneity problem	151
5.2	Possible approaches to improve thickness homogeneity	152
5.3	Viscosity increase for the homogeneity improvement	153
5.4	Photo polymerizable varnishes for the homogeneity improvement	154
5.4.1	Preliminary tests on the curable varnish	156
5.4.2	UV Curing	161
5.4.3	Ink design	165
5.5	Deposition of solutions with varnish	168
5.5.1	Drop generation	168
5.5.2	Liquid distribution homogeneity	169

5.5.3	Liquid distribution on metallic tapes	173
5.6	Pyrolysis physico-chemical analysis of films deposited with varnish	175
5.6.1	Pyrolysis performance	176
5.6.2	Thickness and mass evolution	177
5.6.3	In-situ mechanical properties study for films deposited with varnish	180
5.7	Synthesis of thick pyrolyzed films	181
5.7.1	Surpassing $1\mu\text{m}$ in one single deposition	184
5.7.2	Thickness increase through multideposition	186
5.7.3	Pyrolyzed film cross section and film compactness	187
5.7.4	BZO Nanocomposite and Ag addition for an enhanced YBCO performance	189
5.8	Growth of YBCO films	191
5.8.1	Pristine growth of YBCO films on LAO substrates	191
5.8.2	YBCO-BZO nanocomposite YBCO on LAO substrates	192
5.8.3	Growth of IJP YBCO thick films on metallic buffered tapes	195
5.9	Chapter summary and conclusions	196
6	Conclusions	201
A	Appendix	205
A.1	Calculations for the TGA theoretical final mass	205
A.1.1	IR mass determination	206
A.2	TMA viscosity measurement	206
	Bibliography	209

Abbreviations

acac	Acetylacetonate
AcO	Acetate
ADSA	Axisymmetric Drop Shape Analysis
BZO	BaZrO ₃ , Barium Zirconate
BYF	Barium Yttrium Fluoride
BYTO	Ba ₂ YTaO ₆ , Barium Yttrium Tantalate
CCs	Coated Conductors
CSD	Chemical solution Deposition
CZO	Ce _{0.9} Zr _{0.1} O ₂ Zirconium-doped Cerium Oxide
EGA	Evolved Gas Analysis
Er	Young's Modulus (reduced)
DEA	Diethanol Amine
DoD	Drop on Demand
DSC	Differential Scanning Calorimetry
dTG	derivative Thermogravimetry
FF	Fluorine Free
FIB	Focused Ion Beam
GADDS	General Area Detector Diffraction System
H	Applied magnetic field
Hr	Hardness
HTS	High Temperature Superconductors
IBAD	Ion Beam Assisted Deposition
I _C	Critical current
ICMAB	Institut de Ciència de Materials de Barcelona
IJP	Inkjet Printing
IR	Infrared (spectroscopy)
LAO	Lanthanum Aluminate
LED	Light Emitting Diode
MOCVD	Metalorganic Chemical Vapour Deposition
MOD	Metalorganic Decomposition

NPs	Nanoparticles
PEG	Polyethylene Glycol
PLD	Pulse Laser Deposition
PZT	Lead Zirconate Titanate
RABiTS	Rolling Assisted Biaxial Textured Substrates
SEM	Scanning Electron Microscopy
SF	Self Field
SQUID	Superconducting Quantum Interference Device
SUMAN	Superconducting Materials and Large Scale Nanostructures (group)
T	Temperature
TA	Thermal Analysis
T_C	Critical Temperature
TEA	Triethanol Amine
TEM	Transmission Electron Microscopy
TFA	Trifluoroacetate
TGA	Thermogravimetric Analysis
TMA	Thermomechanical Analysis
UV	Ultraviolet light
V	Varnish
YBCO	$\text{YBa}_2\text{Cu}_3\text{O}_{7-x}$
YSZ	Yttrium Stabilized Zirconia

Motivation

The discovery of High Temperature Superconductors (HTS) supposed a giant stride on the power applications technological development.

Among them, the c-oriented, epitaxial $\text{YBa}_2\text{Cu}_3\text{O}_{7-x}$ (YBCO) presents top-tier superconducting performances, making of this complex oxide one of the most studied superconductors.

In order to fully exploit the astonishing superconductor properties, the material should be produced obtaining the best performances at the minimum manufacturing cost, in order to make a competitive market product.

Chemical Solution Deposition (CSD) is presented as a low cost manufacturing methodology for the synthesis of many functional oxides, among them YBCO. It consists of the deposition of an organometallic precursor solution on top of a substrate, followed by a thermal treatment to pass from the deposited solution to a dense, crystalline YBCO film.

Besides the low cost characteristic of CSD, especially if compared with other popular techniques based on high vacuum approaches, such as PLD or MOCVD, this methodology allows a high flexibility and control during the solution synthesis, making of this synthetic route a perfect candidate for the YBCO large scale production in a cost effective process.

For the deposition of YBCO precursor solutions, we present the drop on demand Inkjet Printing technology as a deposition technique perfectly suited for the YBCO films deposition.

The high flexibility and deposition control, together with the scalability of the technique, makes of inkjet printing an appealing technology for the production of long length YBCO films by CSD.

In order to transport large amounts of current, the YBCO films must be thick to increase the critical current. However, to achieve high film thickness is one of the main challenges of the CSD route. The huge thickness reduction produced during the firing of the organic species, also known as pyrolysis process,

produces high stresses that leads to film cracking when the thickness surpasses a few hundred nanometres.

This has forced many researchers to increase film thickness by the multi deposition of thin films in order to avoid film cracking. This is not only time-consuming, but it could also lead to superconducting properties degradation due to the presence of copper segregated interlayers.

In addition to the stress produced during the pyrolysis process, the deposition of thick films is also a matter of study by itself. The large amount of deposited solution should be managed in order to obtain an homogeneous liquid distribution. Only by achieving thick and homogeneous films, the YBCO can display outstanding superconducting performances.

Thus, one of the most relevant objective of this work was to investigate how we can achieve a large thickness in the order of $1\mu\text{m}$ in one single coating, in order to maximize the YBCO superconducting performances in a fast and scalable low-cost process. To achieve this, we focused in the study of the deposition and pyrolysis of YBCO precursor inks deposited by inkjet printing.

Along this thesis we will describe the following results:

1. In chapter 3, we describe how we have designed YBCO precursor inks suited for its deposition using inkjet printing. The deposition of these inks has been studied in order to obtain thick and homogeneous depositions.
2. In chapter 4, we present an exhaustive analysis on the different physico-chemical properties of the films during the pyrolysis process in order to avoid the crack formation.
3. In chapter 5, we show how we have used the knowledge generated during the two previous chapters in order to surpass the micrometer thickness on one single coated YBCO films on top of several substrates in a reproducible way. This achievement demonstrates the high competitiveness of the CSD process for the synthesis of thick YBCO films.

Introduction

Nowadays, the technological development is not only a matter of improving our quality of life, but a race against time to recover the planet sustainability. In the last two centuries the world population has increased almost eightfold, and a 20% of this increase happened in the last 18 years. The demographic explosion came with an increasing demand of power, generated in a 85% from fossil energies, with its corresponding contribution on the global warming.

Considering these numbers, it is clear that we either have to drastically reduce our consumption level or we have to invent a power generation and supplying in agreement with the planet needs (or both).

In superconductivity we find a wide path towards the development of new ways to transport and generate safely and efficiently large amounts of power.

1.1 The superconductivity phenomenon

The superconductors, are materials that present 0 electrical resistance when cooled below a critical temperature (T_C) [1]. This implies that the electrical power can be distributed without any dissipation. In addition, the high electromagnetic performance of these materials can upgrade the efficiency of power generation and storage devices to a new level.

However, the first superconducting materials could only operate within 10K of the absolute zero, requiring liquid helium in order to achieve superconductivity [2].

The high price of the cooling media limited the superconductor utilities to small scale, high priced technologies.

A huge breakthrough came with the discovery of the High Temperature Superconductors (HTS), in the 1986, based on ceramic materials. The HTS display superconducting properties above the liquid nitrogen boiling point of 77 K, a readily available and inexpensive compound [3].

Of all the contemporary HTS, $\text{YBa}_2\text{Cu}_3\text{O}_{7-x}$ (YBCO, $T_C \approx 92$ K) exhibit one the most promising performance at both low/high field and temperature applications [4]. In figure 1.1 we show the comparison among different commercially available superconductors.

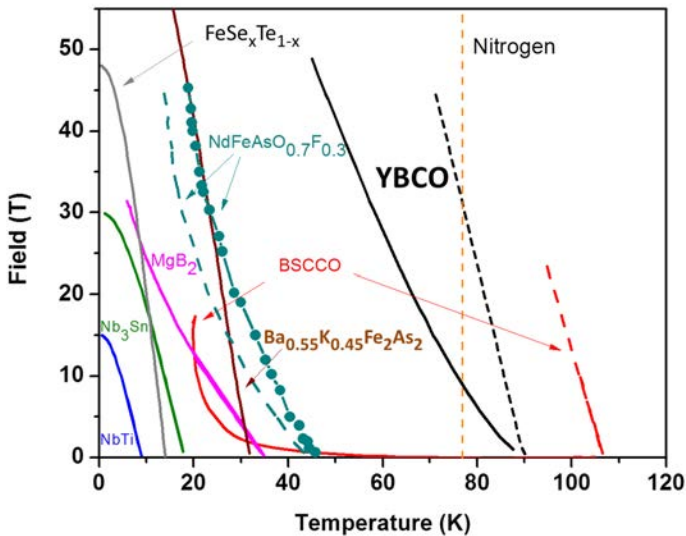


Figure 1.1: Comparison of the critical temperature (T_C) and critical field (H_C) among commercially available superconductors. the dashed line for YBCO and BSCCO represent the theoretical superconducting limits, while the solid line are the real barriers of the superconducting effect, known as irreversibility lines. Image obtained from [5].

Thus, numerous electric power and large scale applications are expected to be achieved through HTS, including power deliver systems, generators, transformers, motors, fault current limiters, SMES and high field magnets [4, 6–9].

1.1.1 Coated conductor architecture

The unit cell of the superconducting YBCO phase, displayed in figure 1.2, is based on a triple perovskite ABO_3 stacked vertically along the c -axis: a central $YCuO_3$ perovskite with two adjacent $BaCuO_3$ perovskites and some oxygen vacancies [10].

Only by achieving high epitaxy, with small angles between grain boundaries ($<2^\circ$) [11, 12], the YBCO (and superconducting cuprates in general), is able to display the highest superconducting performances.

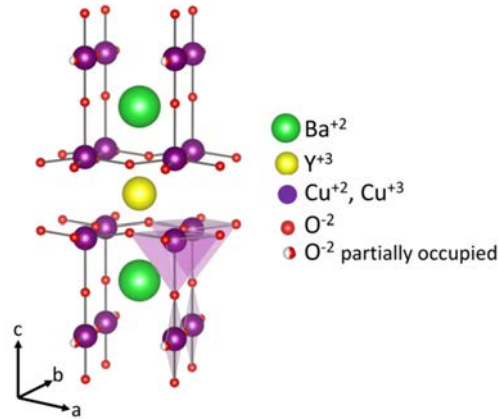


Figure 1.2: Superconducting YBCO phase (orthorhombic) unit cell.

The discovery of suitable methods to grow YBCO HTS phase as epitaxial films on top of bi-axially textured substrates following a multilayered architecture, i.e. coated conductors (CCs), enabled the progress towards the superconductor large scale synthesis [7, 13–17].

However, each layer of the CCs architecture is subject to a very specific structural conditions, which in turn, have to be compatible with the large scale production of a highly textured material.

Through the years, high-throughput methodologies were developed in the production of textured substrates with the lattice and orientation requisites for the YBCO epitaxial growth [6, 18].

The two main methodologies are the Rolling Assisted Biaxial Textured Substrates (RABiTS) [19] and Ion Beam Assisted Deposition (IBAD) [13, 20]. The former technique is based in a thermomechanical treatments and the latter, on the irradiation of a ion beam during the deposition of a buffer layer on top of a non textured metallic tape.

In figure 1.3 we show a schematic representation of the CCs architecture.

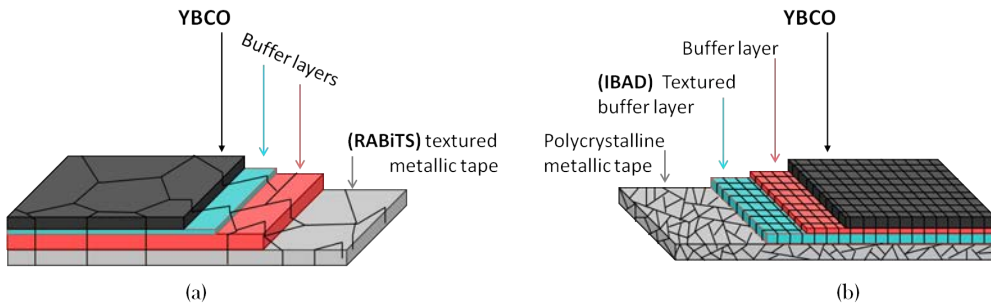


Figure 1.3: Coated Conductors (CCs) architecture. (a) RABiTS and (b) IBAD texturing approach.

These technologies allow for the low-angle grain boundaries YBCO growth required to percolate the superconducting current.

The next challenge is to fully exploit the opportunity that the CCs offers in the manufacturing of high-throughput and cost effective, high performance HTS [6, 21–23].

Several vapour based deposition techniques (sputtering, pulsed laser deposition (PLD), molecular beam epitaxy (MBE), chemical vapour deposition (CVD), etc.) have demonstrated its applicability on the long-length production of high performance for the different CCs layers [24–26].

Unfortunately, the highly pure environment and the sophisticated vacuum control required on these techniques, increase the material production price.

1.2 Chemical Solution Deposition (CSD)

The Chemical solution Deposition (CSD) presents a highly potential alternative for the low cost manufacturing of a wide range of functional oxides.

The epitaxial growth using CSD methodology have been demonstrated for complex oxides, including superconductors, electrolites, photovoltaics, piezo-electrics, etc. [27–30].

In addition, this methodology permits a strict control on the functional oxide composition through the chemical solution design. In this way, the film stoichiometry and composition can be modified (e.g. nanoparticles addition for nanocomposite films) [31–33], making of CSD a very flexible synthetic route.

The CSD methodology consist on four main steps:

- I **Solution design:** A solution containing the precursors of the material is prepared in the desired stoichiometry. The addition of gelators, nanocomposite precursors, polymeric reagents, surfactants, etc. during the precursor solution design, will determine the film physico-chemical properties during the next steps.
- II **Precursor solution deposition:** The solution is deposited using any of the techniques used for CSD. Some examples are: spin coating, dip coating, inkjet printing, slot die, among others. The deposition technique will strongly determine the solution rheological parameters required.
- III **Firing process:** When the functional oxide precursors are organometallic species, a low temperature process (300-500°C), known as pyrolysis, is required to remove all the organic mass, deriving in an amorphous or nanocrystalline film.
- IV **Film crystalization:** A higher temperature annealing (700-800°C) is performed on the film after the pyrolysis process, which will be crystalized into the desired ceramic phase. For some particular cases, as it is the YBCO, a post annealing process is required to achieve a determined crystalline phase.

Besides the manufacturing technique, there is another essential factor that determine the cost-performance of any superconductor: The film thickness.

Since the electric current transported through the superconductor will be determined by both the material performance and the cross section, in order to achieve a competitive product, a low $\text{€}/\text{kA}$ is required. The synthesis of coated conductors with the maximum YBCO thickness, maintaining a high quality crystal structure in order to obtain high a critical current (I_C), is mandatory for a large scale YBCO commercialization [8, 34].

As we will show, this is the great challenge that faces the coated conductors industry.

This thesis is devoted to the study and optimization of the first three phases of the YBCO synthesis of thick films using the CSD approach. In particular, the solution deposition was performed with a single nozzle inkjet printer with a piezoelectric lead zirconate titanate (PZT) drop on demand (DoD) actuator.

In the following sections we will shortly review the different steps of the CSD methodology, focusing on the YBCO synthesis.

1.2.1 YBCO precursor solution design

The ink formulation is the foundation to build up a YBCO film. The performance on any of the next steps (deposition, pyrolysis and growth) will be determined by the decided ink design.

The YBCO precursor solution can be separated in 3 parts: the organometallic precursors, the carrier solvent and the additives.

The three ink components must demonstrate a good compatibility in terms of solubility and stability in order to show a high robustness.

Traditionally, the precursor salts for the YBCO synthesis were based on short chain, fluorinated organometallic precursors [35–39]. The interest of fluorinated precursors lies in the formation of BaF_2 as an intermediate nanostructured phase, instead of BaCO_3 , a very stable compound that deteriorate the YBCO superconducting performance [35, 40].

Even though new YBCO synthetic routes based in fluorine free films [41, 42], during this thesis we have used inks based on low fluorine inks, where the fluo-

rine content is kept at a minimum value in order to avoid the BaCO_3 formation.

Barium and Copper acetates and Yttrium trifluoroacetates present a good solubility in polar alcohols and organic acids, the carrier solvents that we choose for the for the YBCO synthesis due its good wetting in metallic tapes and, suitability with the inkjet printing and low environmental impact [43].

In addition, these organometallic precursors can be decomposed without a trace within the 500°C [37].

The possibility to add compounds to the precursor solution in order to tune the different properties of the film on any stage is one of the biggest advantages on the CSD methodology.

The addition of UV curable polymer precursors [44] to obtain an homogeneous film during the deposition, of chelating agents that increase the mechanical resistance to crack during pyrolysis [45, 46] or the addition of nanoparticles to achieve improved superconducting performances by growing a nanocomposite film [32, 47], are some of the strategies used on this thesis to achieve homogeneous, thick, high performance YBCO films.

1.2.2 Precursor solution deposition

As we mentioned, several deposition techniques can be used for the deposition of solutions, with a demonstrated success on the YBCO synthesis. However, drawbacks as the non-scalability of the spin coating or the constant rheological and concentration changes that suffers the dip coating solutions, must be considered when deciding the most fitting technology.

Inkjet printing technology is presented as a scalable, highly flexible technique, which permits a strict control on the solution deposition and conditions. This, together with the wide gallery of materials that can be formulated as inks, and the possibility to deposit according to patterns are some key features that make inkjet printing technology an extremely effective deposition technique [48–52].

A more extensive introduction on the solution deposition by inkjet printing will be covered in chapter 3. But in general terms, during the deposition stage,

the precursor solution must be homogeneously distributed on the substrate.

The large liquid volume managed, specially in the deposition of thick films, tends to redistribute along the substrate causing inhomogeneities during and after the deposition process.

The solvent/s evaporation rate, the ink rheological parameters, the presence of a colloidal suspension and the liquid-substrate wetting may cause liquid redistribution, leading to thickness inhomogeneities [53–55].

In addition, the wet film curing to obtain a gel film, is also a source of liquid inhomogeneity. The capillary forces arisen from the wet film evaporation rate gradient, generate an edgeward liquid movement known as the "coffee stain effect" [51, 56–59].

Any thickness inhomogeneity generated during the deposition-curing stage, will have devastating effects on the film during the posterior thermal treatments, producing the formation of cracks during the pyrolysis stage and a poor crystalline structure during the growth of the YBCO.

For this reason, the solution and deposition parameters must be strictly studied and adapted in order to obtain an homogeneous liquid distribution during the deposition step.

1.2.3 Pyrolysis process for thick YBCO films

In the third stage of the CSD route, the organic mass from the organometallic YBCO precursors is decomposed in a process known as pyrolysis. During this step, the dried gel film containing the organometallic precursors is rearranged into an amorphous or nanocrystalline phase [60–62].

The organic mass decomposition causes the loss of more than the 50% of the film mass. The mass loss, together with the film densification caused by the gel transformation into a dense ceramic, leads to a huge film shrinkage.

Since the film volume reduction (figure 1.4) is hindered by the substrate dimensions, a strong tensile stress is generated in parallel to the substrate [63, 64].

This stress, with values in the order of hundreds of MPa [61, 65], causes the formation of cracks that are propagated along the film [62, 66], making the pyrolysis process, the critical step on the thick film synthesis through CSD [43, 67, 68].

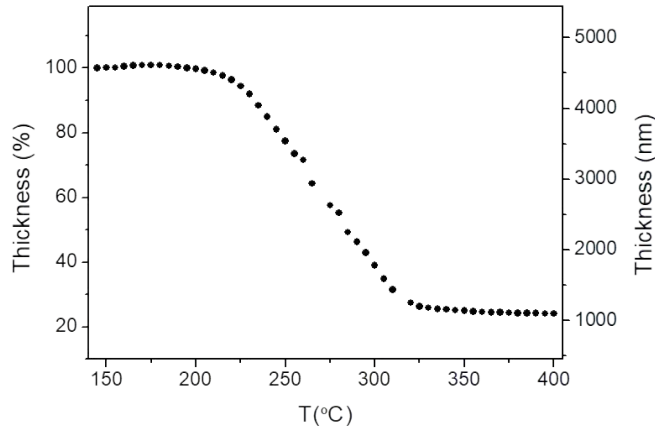


Figure 1.4: Example of the thickness huge reduction that suffers a film during the pyrolysis stage.

In the last four decades, the number of publications concerning the stress produced in thin coatings can be counted by thousands [69–72]. However, the problems arisen from this stress when the film thickness is increased have not found a successful solution.

Reviewing the most recent works regarding the functional oxide synthesis following the CSD route, we can obtain an idea of the challenge that supposes to achieve thick films in one single deposition.

The largest thickness achieved until now for YBCO films was reported by Rupich et al., demonstrating 800nm on a single coating [73].

This value is far above the main thickness obtained for the majority of the groups working on CSD manufacturing, which is often <200nm for non-silicate oxide films [74–77].

Another problem typically observed on the CSD film synthesis is the spontaneous generation of complex, ordered film buckling induced by a compressive stress. In figure 1.5 we display an example of the film surface after the buckling generation.

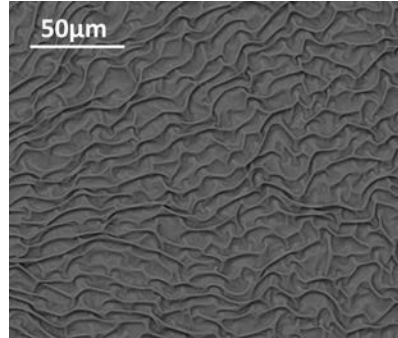


Figure 1.5: Scanning Electron Microscopy (SEM) image of a buckled YBCO film deposited on a Lanthanum Aluminate (LAO) substrate.

The thickness and elastic modulus will determine the periodicity of this structure, for this reason, the film buckling has become of interest in the generation of optical devices or for a fast determination of the elastic modulus of polymeric thin films, among other applications like elastic electronics [78–81].

However, when it comes to the superconductor synthesis, this phenomenon is highly detrimental. The difference between the highest and the lowest part of the wrinkle can be of several microns, making impossible an epitaxial YBCO growth. For this reason, this phenomenon must be strictly avoided.

To overcome the stress produced defects, many authors follow a repetitive deposition-pyrolysis cycle to increase the film thickness [82–84]. However this manufacturing route has two problems:

1. The production time is largely increased.
2. Copper is segregated in the interlayers, decreasing the superconducting performance [21].

Thus, achieving thick films in a single step is fundamental to advance in the

large scale superconductor manufacture at a low cost.

Not many works have focused their attention in the pyrolysis step during the synthesis of functional oxides synthesized by CSD. On these works it can be found the optimization on the thermal process parameters or on the ink formulation through the addition of compounds to improve the film mechanical resistance to crack. But until now, any in-depth study on the physico-chemical pyrolysis parameters has been carried out.

In order to achieve thicker films in one single process, further effort must be dedicated to comprehend the film evolution during the pyrolysis process. The critical zones where the stress release phenomena occurs, how the different chemical species evolve and their impact on the film structure and the evolution of the film mechanical properties, are fundamental factors to take into account during the design of the precursor solution and the pyrolysis conditions.

This is not only valid for the YBCO synthesis but for all the functional oxides manufacturing through the CSD route.

1.2.4 Nucleation and growth of YBCO film

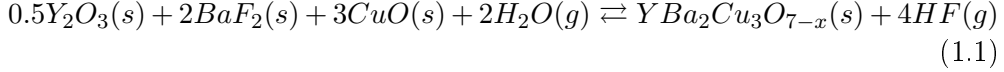
The last step of the film synthesis of the HTS film by CSD consist on a high temperature annealing to nucleate and grow *c*-oriented YBCO.

The conversion from an amorphous on nanocrystalline film to a fully epitaxial crystalline structure is delicate process, involving complex thermodynamics and kinetics.

The growth conditions are controlled through the pressure and temperature, selecting the phase diagram region with the better suited thermodynamic parameters to obtain the *c*-axis YBCO orientation.

But the window between the *c*-axis nucleation and the growth of any other YBCO orientation or secondary phase is generally really narrow.

The YBCO growth is a kinetic process based in a solid-gas diffusion, depending on the equilibrium $K = [HF]^4/[H_2O]^2$ according to equation 1.1 [36, 66]:



Thus, the film thickness will have a strong effect on the required growth conditions. Any thickness variation will require different annealing parameters (gas pressure, heating rate, temperature, time) in achieve a full YBCO epitaxy.

For this reason, the film resulting from the pyrolysis process must be a defect free film, with a very homogeneous thickness distribution.

Besides the synthesis of a high quality crystalline structure, there is another factor affecting the superconducting performance.

Despite of the existence theoretical critical temperature and magnetic field limits to obtain superconducting effect, the real barrier is located in the known as Irreversibility line [85].

The irreversibility line is determined by the motion of vortex of superconducting current induced by the quantized penetration of magnetic field. This motion, produced by Lorentz force, can be blocked by the introduction of controlled defects in the YBCO matrix, known as pinning centers [66].

The synthesis of nanocompositie films by the nanoparticles segregation has proven an effective way to block the vortex motion, displacing the irreversibility line to higher magnetic fields and temperature, and thus, improving the superconducting performance.

To overcome the different challenges presented by the CSD route, outlined in figure 1.6, is essential in order to achieve a cost effective production of High temperature Superconductors using the Coated Conductor architecture, bringing a great leap in the power technological development.

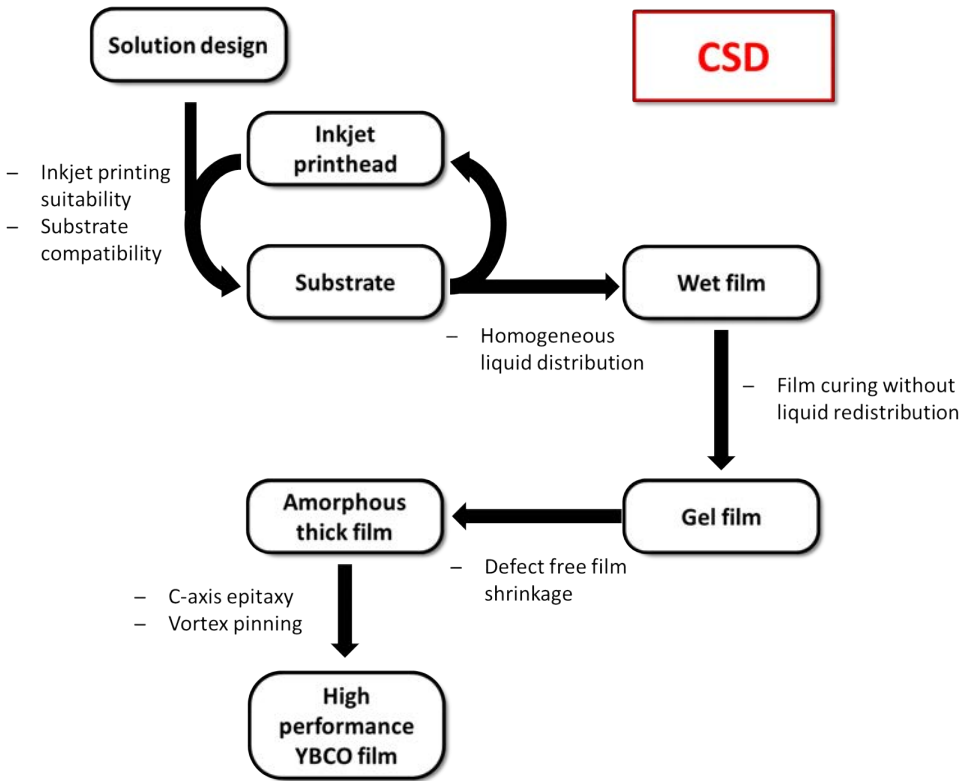


Figure 1.6: Road map of the different stage's milestones during the thick YBCO film synthesis following the CSD methodology.

Experimental procedure

During this chapter we will introduce the experimental methodologies used on this thesis. This includes the different instrumentation employed to obtain the results that we will discuss during the following chapters, as well as the protocols for the ink synthesis and the samples characterization.

2.1 Ink design and preparation

We based the ink design in the YBCO organometallic precursors following the low fluorine route.

All the low fluorine solutions were prepared using copper and barium acetates ($\text{Cu}(\text{AcO})_2$ anhydrous, Alfa Aesar - Cymit Quimica and $\text{Ba}(\text{AcO})_2$, Sigma Aldrich) and yttrium trifluoroacetate anhydrous ($\text{Y}(\text{TFA})_3$ anhydrous, Sigma Aldrich).

The used solvents for the solution synthesis were:

- Anhydrous Methanol (99.97%) from Scharlau.
- Anhydrous Ethanol (99.97%) from Scharlau.
- Butanol (98%) from Sigma-Aldrich.
- Propionic acid (99.5%) from Sigma-Aldrich.

Alcoholic solvents have demonstrated a good suitability as carrier solvent in SUMAN group at ICMAB as well as in other groups devoted to the YBCO synthesis by CSD [27, 86].

Alcohol based solutions display a good wetting on both stainless steel metallic and single crystal substrates.

In addition the wide range of boiling points of the alcohol depending on the carbon chain length, permit an accurate tuning on the ink drying conditions.

It is known that acetates are poorly soluble in alcohols, specially as the solvent carbon chain gets longer [87]. For this reason, all the solutions share a part of propionic acid in order to dissolve the acetates, otherwise hardly soluble in alcohols.

The addition of this propionic acid performs a ligand exchange of the acetates for the propionates that can be easily dissolved in alcohols [27].

Different YBCO precursor solutions have been used along this work. In next table (2.1) the different ink compositions are displayed, describing the nomenclature used for each solution:

Solution name	Solvent 1 (%V/V)	b.p. ($^{\circ}C$)	Solvent 2 (%V/V)	b.p. ($^{\circ}C$)
4B	Methanol (74)	64.7	Propionic acid (26)	141.2
4C	Propionic acid (100)	141.2	—	—
4D	Ethanol (100)	78.2	—	—
4G	Butanol (80)	117.7	Propionic acid (20)	141.2

Table 2.1: Solution nomenclature

The nomenclature shown in the previous table does not contemplate the additives. Thus, a solution with the solvent composition and proportions of the 4B solution will remain called the same even with the addition of a new compound.

The used solution concentration depends on the ink and its rheological properties, and it will affect the deposited liquid volume.

From now, on the concentration will be defined as the sum of Y, Ba and Cu salts in the corresponding 1 2 3 stoichiometry (i.e. 0.25M Y, 0.50M Ba and 0.75M Cu will correspond to a 1.5M solution).

The strategy for the ink synthesis consists on the organometallic precursors solution on a mixture of the propionic acid and the chosen alcohol at 30°C under stirring, over night and under an Argon atmosphere.

After the salts are solved, the additives are added to the solution on the required quantity before filling the solution to volume. The additives used on this thesis are presented in table 2.2

Additive	Additive effect
Diethanolamine (DEA)	Film mechanical resistance improvement
Tantalum ethoxide (Ta(EtO) ₅)	Nanocomposite synthesis by the ss-nanocomposites route
Zirconium acetylacetonate (Zr(acac) ₂)	BZO Nanocomposite synthesis by the ss-nanocomposites route
BZO nanoparticles	Nanocomposite synthesis by the ex-situ nanocomposites route
Polyethylene glycol (PEG)	Ink viscosity enhancing
UV curable Varnish	Film homogeneity and mechanical resistance improvement

Table 2.2: Additives used along this thesis and their contribution on the film synthesis; ss-nanocomposites route refers to spontaneously segregated nanocomposites route.

The presence of water over 1,5% in the solution becomes highly detrimental for deposition, pyrolysis and even growth [62]. For this reason it is important to reduce and control the water content inside the solution.

To remove the salts' water content, before the ink synthesis, the precursor salts are dried using a thermostatic vacuum dryer (Vacuo-Temp, from Selecta) operating at 10^{-2} mmHg and $T \sim 85^\circ\text{C}$ for 12 hours.

To maintain the ink in inert conditions, it is synthesized and stored under Argon atmosphere.

2.2 Solution characterization

The different ink parameters were studied in order to check the ink suitability on the different synthesis stages. This includes the ink rheological parameters and the water content of the solution.

2.2.1 Ink rheology characterization

The different parameters affecting the rheology of an ink (viscosity, surface tension, density) will determine every essential process during the ink deposition. This includes the drop generation by inkjet, the ink spreading and wetting [54, 88].

For this reason the characterization of these parameters is mandatory in order to optimize the ink design.

2.2.1.1 Density

The solution density was obtained by weighing 1 mL of solution in an analytical balance three times.

2.2.1.2 Viscosity

Viscosity values were measured using a HAAKE RheoStress RS600 (Thermo Electric Corporation) with the Controlled Rate method coupled to the software Rheowin 4 Job Manager.

The viscosity values for the solution characterization were made at 22°C in a clean room class 10000. In addition some measurements were performed at higher temperatures (up to 75°C), which required the saturation of a glass hood to avoid viscosity changes during the measurement due to solvent evaporation.

The measurement principle is based on detecting the shear deformation applied on the sample with a rotational plate.

For our measurements, we worked at a constant rotational speed. When the desired shear rate is achieved, the resulting shear deformation is related with viscosity.

2.2.1.3 Surface tension and contact angle

The contact angle and surface free energy of the inks were measured by Drop Shape Analyzer DSA100 (KRÜSS). This device has two operation modes, one for the measure of each property.

ADSA (Axisymmetric Drop Shape Analysis) method determines the fluid interfacial tensions by the meniscus shape, adjusting the drop shape using the software to generate a fitting curve [89].

The equilibrium shape of a liquid drop can be numerically determined by solving the Laplace equation of capillarity together with proper boundary conditions.

By using the Newton-Raphson method, the software minimizes the theoretical curve to the real drop shape and once the best fit is found, the real number for the surface tension and contact angle is calculated and provided by the software.

Surface tension is measured by the pendant drop method. This technique is based on determining the surface tension of a liquid by the shape of a pendant drop, which varies according to balance of surface/interfacial tensions and an external force, as is gravity in this case [90].

To obtain the measure, a video with a high resolution camera is recorded while several drops fall illuminated from the side. Once recorded, we select an image from the video when the meniscus is minimum and we fit the drop. If the fitting is good enough, the surface tension value is obtained.

Throughout this work, contact angle measurements were extracted from analysis of the images of $2\mu\text{L}$ digitized sessile drops photographs, performed by means of a DSA100 equipment (KRÜSS, GmbH) by using the ADSA technique. The tangent that determines the contact angle is obtained after the fitting described before.

2.2.2 Water content determination

The water content determination is measured by volumetric type Karl-Fisher titration [91].

This reaction takes place inside a hermetic glass vessel with dry methanol as the titration medium and under continuous stirring.

The relative quantity of water must be kept as low as possible, never surpassing a value of 1.5%_{wt}.

2.3 Inkjet printing, drop generation and deposition

With the exception of a few samples used for a specific analyses, all the films along this thesis were deposited by inkjet printing.

The employed inkjet printer was, for the most part, a home-made system with the incorporation of a commercial lead zirconium titanate (PZT) piezoelectric actuated dispenser (Microfab Technologies, MJ-AB-01-60) with a 60 μ m nozzle diameter.

The drop was generated using a bipolar squared wave, as we show in figure 2.1. The waveform is divided by segments (μ s) that can be individually modified in order to tune the pulse length.

The two other important parameters that can be modified are the wave pulse width (voltage), and the wave frequency.

Through the waveform (wave pulse width and length), the drop volume and speed can be tuned.

2.3.1 Drop pitch

The drop frequency is used to determine the drop distance in one direction.

Even if our inkjet printing systems works as a drop on demand, meaning that a drop is generated with each pulse, the drops are continuously being expelled. The nozzle is static, it is the platform that moves in two perpendicular directions.

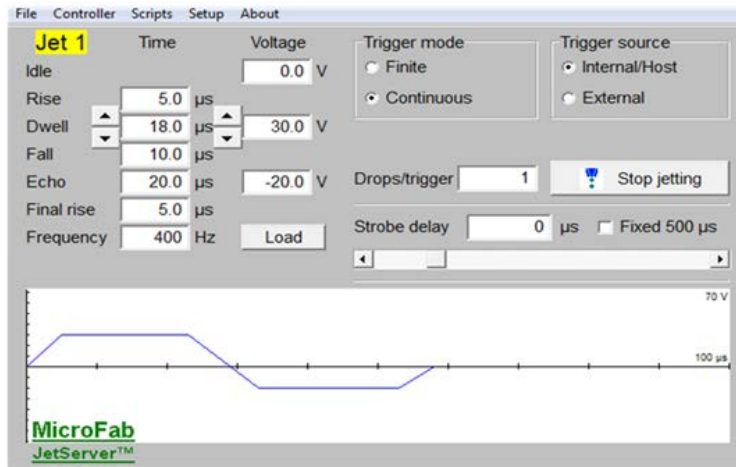


Figure 2.1: text

One motor moves the platform at a constant velocity of 1cm/s in what we define as X direction. The drop spacing in this direction, the frequency determines the drop spacing.

The other motor (Y) performs a lateral step, with a micrometer resolution. This lateral steps defines the drop distance in Y direction.

The spacing between drops defined in the X and Y is known as drop pitch. It is an important parameter to improve the deposition homogeneity since it will determine the overlapping among drops [92]. In addition, the drop pitch together with the drop volume is used to define the film thickness, since it will determine the number of drops that will be deposited on the substrate.

2.3.2 Drop monitoring

The drop is controlled through a stroboscopic camera. Through the piezo-electric actuator software (fig. 2.1) we can define the strobe delay in order to see the drop at different stages, as we display in figure 2.2.

For the drop image acquisition and volume calculation, we used a LabVIEW

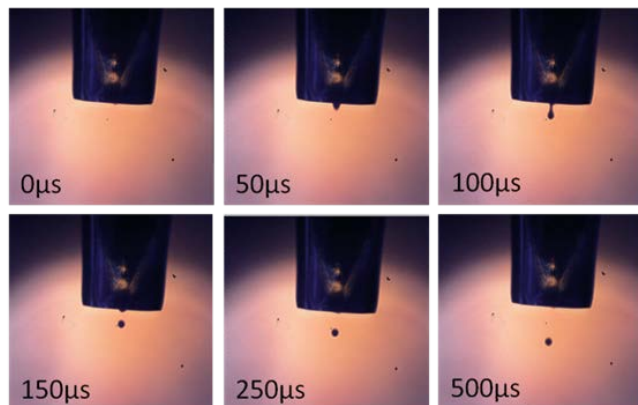


Figure 2.2: text

designed software based on the pixel count to determine the drop size: Taking as reference the nozzle orifice diameter of $60\mu\text{m}$, we establish the pixel size and with this we are able to determine the drop diameter.

2.3.3 Meniscus control

For the meniscus control, a pressure system based on a venturi tube was used. The working principle consist on the vacuum generation that results when a fluid flows through a constricted section of a pipe.

Using the pressure system, together with the waveform, the drop volume was tailored. Also by tuning the physicochemical ink properties such as the viscosity and the surface tension, the drop volume was modified.

2.4 Substrate type and treatment

The substrates used for this work can be classified in two types: Single crystal and buffered metallic substrates.

2.4.1 Single crystal substrate

In order to study the different stages of the YBCO synthesis by CSD, at laboratory scale, the films were deposited, for the most part, on a single crystal.

The single crystal substrate consist on a $5 \times 5 \text{mm}^2$ epitaxial monocrystal of lanthanum aluminate (LaAlO_3 , LAO) with a (001) orientation.

The flat and non-reactive LAO surface, together with an almost identical cell parameter to the YBCO one (-0.47 mismatch) makes of LAO a very suitable substrate for the YBCO growth [93].

In order to achieve a higher liquid homogeneity, we used an ozone substrate activation treatment for 15 minutes. The reactive ozone interacts at the molecular level with surface contaminants causing them to degrade [94]. This method is particularly effective with organic contaminants that are frequently found on AFM probes and surface [95].

The effect is an increasing on the surface tension, enhancing the solution wetting on both LAO and tape. Furthermore, the treatment guarantees an homogeneity on the surface conditions of the substrate.

2.4.2 Buffered metallic substrate

The second used substrate type were buffered metallic tapes from Bruker. This substrates consist on a RABiTS textured metallic substrate with a yttria stabilized zirconia (YSZ) deposited by PLD. A ceria stabilized zirconia (CZO) buffer was deposited at ICMAB by CSD.

Both substrates (single crystal and buffered metallic substrates) were cleaned with sequence of acetone - methanol - methanol, and dried with a N_2 pistol. The substrates are inspected with a microscope and the cleaning sequence is repeated until they are clean.

2.5 Pyrolysis process analysis

During te pyrolysis stage, the organic matter, which represents more than an 50% of the total mass, is decomposed leading to amorphous or nanocrys-

talline ceramic precursors for the YBCO synthesis.

The film shrinkage of the film during the decomposition causes a biaxial stress that is released by cracking or buckling the film.

To avoid the stress release phenomena, the film parameters during the pyrolysis process must be strictly controlled and characterized.

2.5.1 Tubular furnaces

The pyrolysis process consist on a heating treatment from 320°C to 500°C depending on the organic compounds present in the film.

The thermal treatment is carried out in a tubular furnace with a gas flow of 12L/min of umid oxygen (2% H₂O in O₂). The water vapour is used to avoid Cu sublimation of the copper compound by hydro-stabilization [96].

2.5.2 Optical microscopy

The main method to observe the film quality after deposition or pyrolysis is by checking the film morphology in an optical Olympus BX51 microscope.

It was used for as first characterization of the films at a any stage of the synthesis.

In addition, the microscope software allows the multi-time image acquisition. With this mode, we were able to assemble the pictures acquired during a time lapse in a video format. This tool was specially useful when coupled with the pyrolyzer, which we will describe as follows, in order to obtain a video of the film during pyrolysis process.

2.5.3 Pyrolyzer

For the in-situ visualisation of the film during pyrolysis treatment, a heating stage with a small window was used. Using this heating stage, we were able to observe and record the whole process through the optical microscope. We consider convenient to show an image of the pyrolyzer, displayed in figure 2.3.

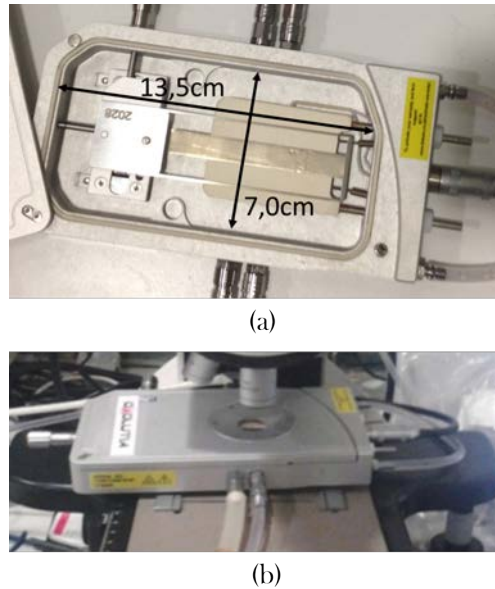


Figure 2.3: Picture of the heating stage (a) uncovered and (b) covered and coupled with the optical microscope, with the microscope objective pointing through the heating stage window.

The heating stage, that we call "pyrolyzer" has two main differences from the tubular furnace:

1) The pyrolyzer heating mechanism is transmission instead of convection. It uses a silver resistance that can heat up at $50^{\circ}\text{C}/\text{min}$.

2) The gas flux collides in the silver resistance distributing the gas around the sample, generating on this way the desired atmosphere undisturbing the film surface. For the tubular furnace case, the gas pass directly through the sample, dragging out the decomposition products, which in our case is the desired situation.

Even though this differences, the pyrolyzer has become a powerful analysis tool for the pyrolysis study, and the results have been demonstrated to be really similar for the ones obtained from the tubular furnace samples with the same

conditions.

2.5.4 Mass and heat evolution

Different thermal analysis techniques were used for the in-situ the mass and heat evolution during the pyrolysis process. By thermogravimetric analysis (TGA) and its derivative, we studied the film weight loss.

By different scanning calorimetry, the heat flow is studied, providing thermodynamic information about the decomposition/evaporation processes occurring during the pyrolysis.

The composition study of the released gases was studied by evolved gas analysis (EGA).

We complemented the mass study using Infrared spectroscopy (IR), for an accurate composition of the chemical species remaining on the film at different pyrolysis stages.

Unlike the other mass/heat analyses, the IR could not be in-situ performed during the pyrolysis process.

2.5.4.1 Thermal analyses

Simultaneous TG and EGA analysis was performed with a Mettler Toledo model TGA851eLF apparatus. For the weight measurement, the samples were placed on thermobalance, inside uncovered alumina crucibles to facilitate gas exchange.

The mass was corrected with a blank thermogram obtained under identical conditions by measuring a LAO substrate without any deposited film. But given the small measured weight, this correction is not enough.

In order to increase the measurement accuracy, the sample is measured at room temperatures using a microbalance (calibrated with $1\mu\text{g}$ weights) with an absolute accuracy of $1\mu\text{g}$. In other words, the microbalance has an accuracy of $1\mu\text{g}$ with a systematic deviation below $1\mu\text{g}$.

With this scale the sample is measured before and after the experiment. If the initial and final masses don not evolve, then a linear correlation can be established with the mass measured with the TGA microbalance values.

Sometimes the mass evolves from the moment when the sample is weighted to the begging of the experiment (due to solvent evaporation or water absorption, etc.). In these cases, the weighted mass curve is analysed and the measurements are corrected to match the values obtained with the calibrated microbalance [97].

Since the final mass is an oxide, it is very rare that the mass evolves once the pyrolysis process is finished.

The used sample masses in TG measurements were between 2 and 20 mg, usually deposited by spin coating or drop coating.

For EGA analyses, an MKS quadrupole mass spectrometer (Microvision Plus) was used for the released gases composition study. During this thesis, we were interested in the masses associated with water ($m/z=18$), propionates ($m/z=28, 29$), CO ($m/z=28$), acetic acid, acetone ($m/z=43$) and CO₂ ($m/z=44$).

Simultaneous TGA and DSC analysis was performed with a Setaram model Setsys Evolution 16 thermobalance. Placing the samples inside aluminum crucibles.

A gas flow rate of 50 mL/min was set inside furnaces, controlling the gas flow by mass flow meters. In order to imitate the pyrolysis process, humid atmosphere was achieved by bubbling O₂ in water at standard temperature and pressure (25°C, atm).

2.5.4.2 Infrared spectroscopy

For the chemical species measurement, we performed an Infrared spectroscopy (IR) of samples deposited by inkjet printing.

The mid- IR light ($4000-400\text{cm}^{-1}$) can excite the harmonic vibrations of the chemical bounds. The IR spectroscopy is based in detecting the light absorbed,

since each vibration mode absorbs a specific light frequency.

We used a Fourier-transform infrared spectroscopy (FTIR) spectrometer model Vertex 70 from Bruker, transmitting the IR light beam through the sample. This measurements can be performed if the film is deposited on LAO, which is transparent, from dried to fully pyrolyzed films.

To measure a sample, this is placed in a support, represented in figure 2.4, and the IR light beam is passed through the sample. The blanc was subtracted by measuring the LAO substrate without any film deposited on top.

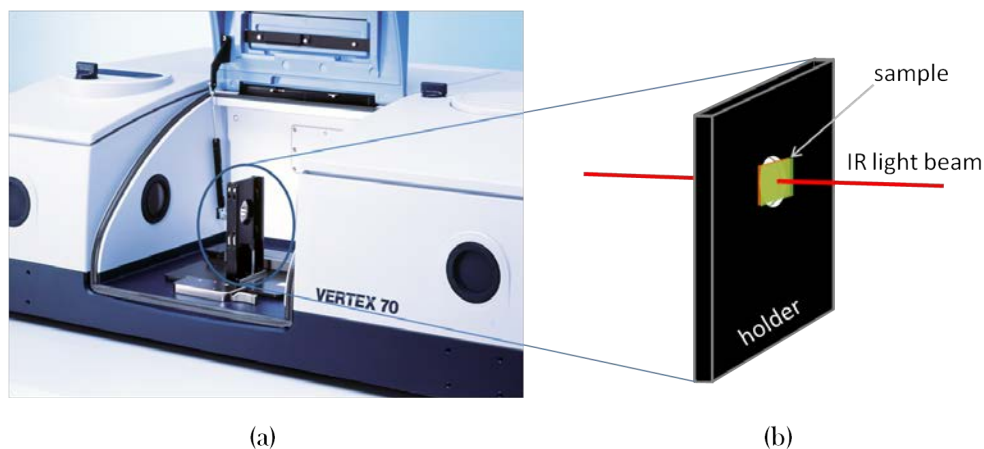


Figure 2.4: (a) Image of the used FTIR spectrometer with the cover lifted in order to see the sample holder. In (b) we show a schematic representation of how the sample is placed on the holder, and how the light travels through the sample.

The two chemical species studied during the mass analysis by IR were [98]:

- The propionate ligands, identified with the alkane absorbance of the stretching mode (sp^3 C-H str.), which presents a band between $2800-3050\text{cm}^{-1}$.
- The trifluoroacetate ligand, which presents a stretching mode absorbance in the fluoromethyl ligand (sp^3 C-F str.) between $1100-1200\text{cm}^{-1}$.

In order to obtain samples, the films were quenched at the desired temperature by retiring the samples from the furnace. For the IR study, the heating stage (pyrolyzer) was used.

2.5.5 Thickness measurements

The thickness measurement is one of the most important parameters to control during the pyrolysis, since the stress release phenomena are strongly associated to the film shrinkage.

In addition, the film thickness and homogeneity characterization in a non destructive way is mandatory in order to grow the film using the optimal crystallization parameters, which depends on the film thickness.

Using interferometry, we can measure the films during all the pyrolysis process (from dried gel films to the fully pyrolyzed films) in a fast, non destructive way.

An interferometer apparatus from Filmetrics, model F20-UV, was used for the thickness measurements. Film thickness from 1nm to 40 μ m can be measured using a wavelength range from 190 to 1100nm. In figure 2.5, a schematic representation of the interferometry principle is displayed.

The interferometry measurements are based on the constructive interference that superimposed electromagnetic waves of the same frequency create when the next condition is accomplished [99]:

$$2n_2d\cos\theta_2 = m\lambda, \quad (2.1)$$

since in our system $\theta_2 = \theta_1 = 0$, then:

$$\lambda = 2n_2d/m \quad (2.2)$$

We used this instrument for two purposes:

1. Characterization of the film thickness and the thickens homogeneity after pyrolysis.

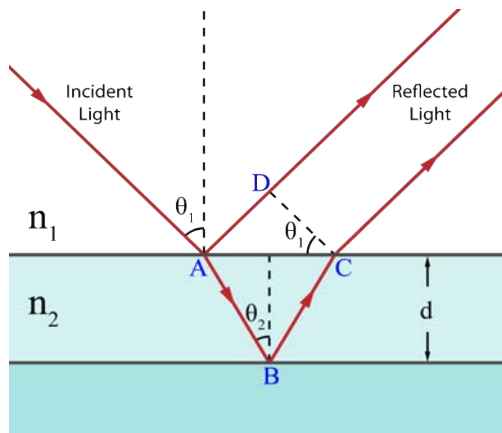


Figure 2.5: Schematic representation of the light travel through the film when a beam is emitted to a thin film. θ_1 and θ_2 are the incident light angles, n is the refractive index of each phase and d is the film thickness. In our apparatus, the incident light is perpendicular to the film surface, then $\theta_1 = \theta_2 = 0$.

2. In-situ study of the thickness evolution during the pyrolysis process by coupling the interferometer with the pyrolyzer.

To obtain a thickness measurement the optical parameters, refractive index n and the extinction coefficient k , must be known for each sample layer. By introducing these parameters, the software fits the interference pattern, calculating the film thickness.

If the optical parameters are unknown for a sample layer, they can be found if the film thickness is known by using the inverse process.

the optical parameter obtained for LAO substrate and for the YBCO precursor film after pyrolysis are described in table 2.3

The thickness values obtained by interferometry, using the optical parameters displayed in table 2.3, were compared with the values obtained by a Profilometer P16+ from KLA Tencor. The comparison showed a perfectly match among the values measured with both instruments.

Layer	Wavelength (nm)	n	k
LaAlO ₃	435.8	2.07	0.00
	632.8	2.07	0.00
YBCO precursors	435.8	1.44	0.06
	632.8	1.44	0.01

Table 2.3

2.5.6 Mechanical properties testing

The film resistance to be deformed (i.e. crack or buckling formation) is determined by three factors: the film thickness, the stress produced and the film mechanical properties [66].

To test the film mechanical properties two different techniques were used: the well know nanoindentation measurements and a novel technique used for the in-situ mechanical testing during the pyrolysis process based on a thermo-mechanical apparatus.

2.5.6.1 Nanoindentation

Nanoindentation is a technique developed in the 1970's, designed for the hardness testing of very small material volumes [100].

In nanoindentation, a hard tip with well known mechanical properties, is pressed on the material, recording the displacement during the tip load and unload.

The load is increased until the sample displacement reaches a pre-defined value, usually a 10% of the sample thickness.

From these curves, exemplified in figure 2.6, the material stiffness (Young's modulus) and hardness can be obtained from the dP/dh slope (defined in figure 2.6) and from the area of the residual indentation in the sample respectively.

The nanoindentation experiments were performed by gnm3 grup at UAB-ICREA using a Berkovich tip.

The samples destined for the nanoindentation measurements were pyrolyzed in the pyrolyzer and quenched at RT on the desired temperature.

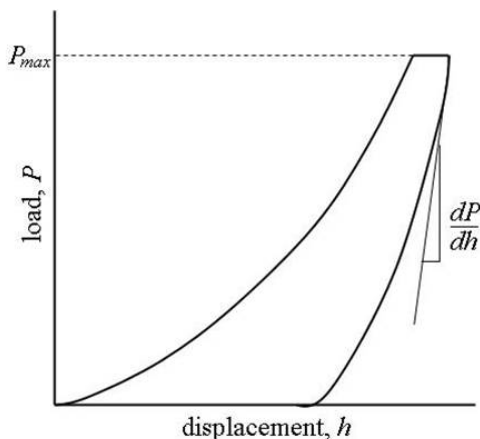


Figure 2.6: text

2.5.6.2 In-situ film mechanical properties measurements

The main problem with the nanoindentation measurements is that, in order to be analysed, the films were quenched.

To test the mechanical properties in the real film conditions, a novel mechanical testing technique was developed by our collaborators in the GRMT research group located in the Universitat de Girona (UdG).

This technique is based on the nanoindentation principle, in other words, on the film displacement response to an applied load. For this purpose, a thermo-mechanical analysis (TMA) apparatus was used, with the TMA quartz cannula acting as the tip of the nanoindenter.

For the sample measurement, a TMA SETSYS evolution from SETARAM was used. The film is placed on a quartz support below the apparatus cannula. Altogether is placed inside the TMA furnace, which permits an accurate temperature control. The TMA set-up is displayed in figure 2.7.

Besides the "indenter tip" dimensions, another difference of the TMA respect nanoindentation is that the load is keep at a constant value during all

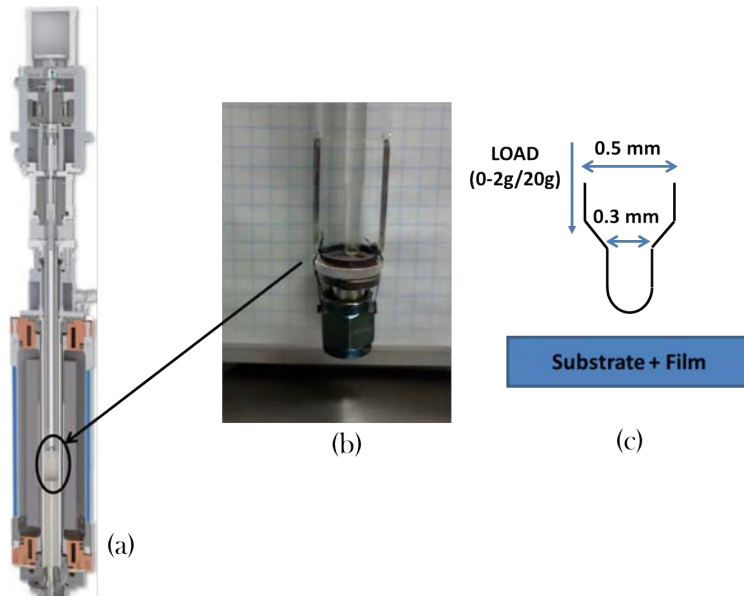


Figure 2.7: (a) Image of the cross section of the TMA apparatus, with the cannula inside the apparatus furnace. (b) Image of the cannula on top of the sample holder. The metallic block is used as a weight to fix the sample. (c) Schematic representation of the cannula dimensions.

the measurement for a specific temperature. In order to obtain a trustful information about the sample displacement, the load was kept for 1 minute at a constant load of 2g or 20g depending on the film stiffness.

The typical displacement curve obtained from the TMA measurements is displayed in figure 2.8.

The samples, deposited in $10 \times 10 \text{ mm}^2$ substrates, were heated up at a constant heating rate of $10^\circ\text{C}/\text{minute}$ and indented for 1 minute in the analysed temperature. This implies that a temperature shift of 10°C is produced between the beginning and the end of the indentation.

As we will show later in this thesis, the film displacement response to load, when the samples were tested at intermediate pyrolysis temperatures ($150\text{-}300^\circ\text{C}$), was defined as a liquid like displacement.

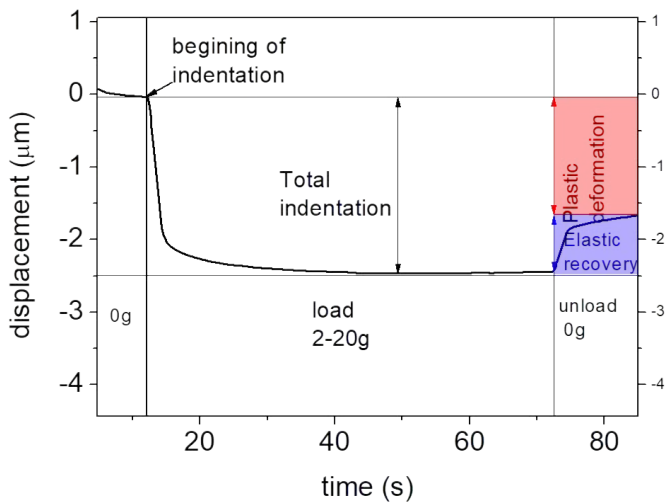


Figure 2.8: text

Using some mathematical approximations on the Stoke's law, which defines the viscosity force on a small sphere moving through a viscous liquid [101], we could measure the film viscosity values while the samples were in the liquid regime.

These approximations and the viscosity measurement equations can be found in the Appendix A.2.

2.5.7 Film morphology analysis

Conventional scanning electron microscopy (SEM) provides topographical and elemental information at magnifications of 10x up to 100000x. This kind of microscope is very suitable to obtain surface information about grain size, porosity, particle's distribution or material inhomogeneities, among other applications.

Since in this work we only focused our attention in pyrolyzed films, the interesting morphological information was located in the film cross section.

In order to obtain a clear cross section, focused ion beam (FIB) was used [102].

Cross-sectional images were obtained using a dual-beam scanning electron microscopy/focused-ion-beam (SEM, FIB) system (Zeiss, Model 1560 XB).

2.5.8 Film structure characterization

For the study on the film texture and composition for both pyrolyzed and grown samples were performed using X-ray diffraction.

When the X-ray waves strike an atom, an elastic scattering is produced. For a regular array of atoms, the waves cancel each other unless the Bragg's law is fulfilled :

$$2d_{hkl}\sin\theta = n\lambda \quad (2.3)$$

where λ is the wavelength of the incident X-ray, n is the reflection order, θ is the angle between the incident X-ray beam and the sample plane, and $d : hkl$ is the inter-planar spacing between the (hkl) family of planes.

A two-dimensional X-ray detector (2D X-ray) uses this principle to generate two-dimensional diffraction patterns. The sample is rotated in $\theta/2\theta$ to obtain information about the diffraction plane composition and texture, while the rotation in χ provides information about the texture out of plane [103].

With this measurement, besides the sample composition, we obtain information about the crystal orientation (i.e. epitaxial and polycrystalline). The signal of the reflections from an epitaxial phase will be detected as spots while the polycrystalline phases will be observed as rings because of the random scattering.

In figure 2.9 we show an example of a measurement with a 2D X-ray. The samples were analysed using a GADDS D8 Advance system from Bruker at ICMAB.

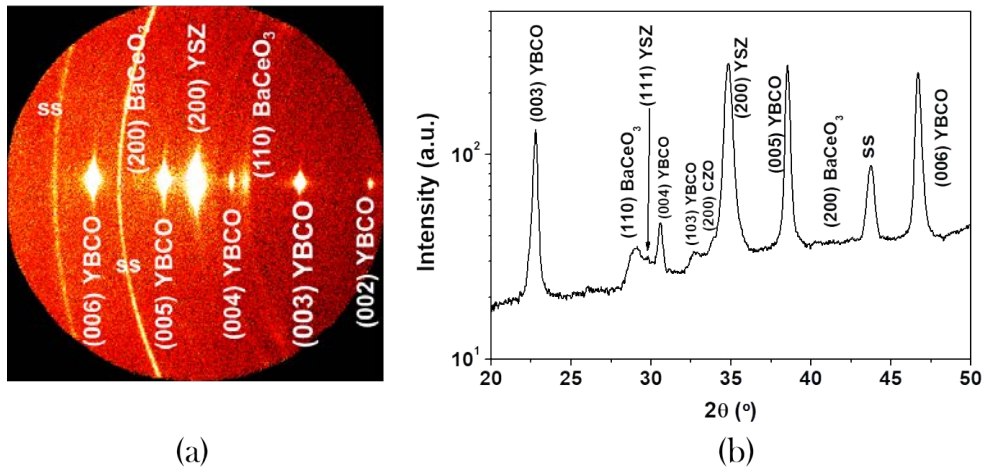


Figure 2.9: Example of YBCO film grown on a buffered metallic tape from Bruker analysed with a $\theta - 2\theta$ 2D X-ray diffraction. (a) 2D X-ray diffraction pattern. (b) Integrated 2D X-ray diffraction pattern.

2.6 Superconducting properties characterization

The grown thick films superconducting properties were characterized using two techniques: Superconducting Quantum Interference Device (SQUID) magnetometry, and transport measurements.

These analysis were performed at ICMAB by the scientific technical staff and by one expert member of our research group respectively.

2.6.1 Superconducting Quantum Interference Device (SQUID) magnetometer

DC-magnetometry was used to measure the electromagnetic response of superconducting YBCO films (after growth). This is a non-destructive, very sensitive technique to detect extremely small magnetic fields.

This instrument is a very sensitive magnetometer consisting of superconducting loops containing Josephson junctions [104].

A SQUID dc-magnetometer Quantum Design equipped with a 7T superconducting and a helium cryostat was used to measure the sample superconducting performance using the Bean critical state model of a thin disk[105].

For the measurement, the sample is placed inside the superconducting coil so that it is submitted to uniform magnetic fields applied parallel to its c-axis.

As a result, a current proportional to the magnetic flux variation is induced in them. The SQUID sensor, acts as a highly sensitive current-voltage converter detecting voltage variations proportional to sample's magnetization.

The main parameters were the critical current density (J_C) variations with temperature and magnetic field, and the critical temperature (T_C) value and transition sharpness (ΔT_C).

2.6.2 Transport measurements

The critical current density can be also calculated through electrical transport measurements using I–V curves, more specifically with the critical current - electric field (J–E) curves.

The transport measurements require of the sample lithography with a photoresist and the posterior film etching in order to obtain the tracks that will be measured. Unlike the SQUID magnetometry, this is a destructive technique.

Silver metal contacts are evaporated on the films and annealed, ensuring low resistance values. The I(V) curves of the YBCO tracks was measured in a four-point configuration. In this four point configuration, a dc-current was introduced until a desired value between two contacts and the voltage is read between the two other pads.

Magnetic field was applied to the current flow, parallel to the c-axis

The transport measurements were carried out in the Physical Properties Measurement System (PPMS) from Quantum Design equipped with a 9T magnet at ICMAB by an expert member of our group.

Using this measurements, the J_C dependence with the magnetic field intensity was characterized at different temperatures.

Ink design and deposition by Inkjet printing

3.1 Principles of ink formulation and deposition

The physicochemical parameters of an ink will determine how easily a drop can be obtained, its stability over large periods of time and how the liquid is distributed during and after the deposition on top of a specific substrate [106, 107]. This affects the performance of every essential process affecting deposition, as the drop ejection and impact, the merging of drops and the liquid - substrate interaction [88, 108].

For this reason, the ink formulation becomes the very first important step to obtain a high quality superconducting film. For a proper printing deposition, ink viscosity, surface tension, density, contact angle, evaporation rate of the solvent, drop volume and drop speed must be strictly met and adjusted [109].

When designing a new ink, the "ingredients" that carry all these physicochemical parameters, as well as the necessary components for the synthesis of the superconductor (or any material that we intend to print), are the following ones:

- **Functional material:** The main functional molecule that carries what will become the final material. It can be virtually any molecule from a metallorganic precursor for superconducting ceramics, to a conductive polymer for plastic electronics or a protein for a biomarker.
- **Carrier solvent:** The choice of the carrier solvent will strongly determine all the printing process. The solubility, boiling point and polarity of the

ink are the main parameters determined by the used solvent or solvents. The carrier solvent also affects to the rheology of the ink together with the additives. Furthermore, the solubility of the other ink components in the selected solvent and their effect on the other parts of the printer device (i.e. corrosion effects) is of great relevance.

- Additives: Rheological and wetting modifiers may also be simple molecules, monomers or polymers, which allow the control of the viscosity and/or the surface tension of the ink to enhance the jetting stability and/or the wetting behaviour onto the substrate. Again, there is a wide variety of additives that can be used; surfactant and wetting agents, dispersants, binders, rheology modifiers, humectants and photoinitiators are just some of the additives that we can find to modify the ink.

The control and tuning of all the parameters affecting deposition will lead to an homogeneous and reproducible film. However, the ink design should take into account the process that follows deposition, as will be the organic firing for this specific work: In CSD - MOD methodology, all the organic matter must be removed during the pyrolysis process, being the stress control caused by the film shrinkage the most challenging step of the thick film synthesis [67, 110].

The ink stability, the storage conditions, the interaction with the print-head of choice and its environmental impact will be factors to consider if we intend to facilitate the process, reduce its cost and demonstrate its applicability.

All these factors represent a great restriction on the available solvent and additives for the solution synthesis. Along this chapter we will discuss the ink composition that fits the most with thick YBCO films deposition with IJP.

3.2 Drop formation

The competing effects of inertial, viscous and surface tension forces determine whether the drop will be formed or not [111]. The output reflected from these parameters will be the drop volume and speed, both with a direct impact on the deposited film quality [74].

For the design of an ink, essential characteristics must be achieved in order to obtain successful depositions, demonstrating the applicability of the inkjet printing system for YBCO - CSD methodology [112, 113].

- Inks should be formulated to meet the specifications of viscosity and surface tension required from the manufacture
- Inks should be easy to handle with the suitable printhead and to modify their composition after additive tailoring to achieve the desired jetting performance.
- Inks should be compatible with the materials used in the printer set-up.
- For a constant and reproducible drop ejection process, inks must have well controlled fluid properties (viscosity, surface tension, density, concentration) and these characteristics must remain constant over a prolonged period of time.
- Solutes and other additives present in the ink must be soluble and do not precipitate during the lifetime of the ink (i.e. ink stability in time).
- During the ejection process, an adequate balance between the evaporation rate of the solvent(s) and the additives should be found in order to prevent partial or total nozzle clogging. On the other hand, a fast drying property is desired to achieve a good print quality of the coating or pattern onto the substrate.

3.2.1 The piezoelectric printhead

As mentioned before, the actuation of the piezoelectric material produces an oscillation on the liquid column resulting on the ejection of a drop. The input for this actuation is the waveform that we induce to the piezoelectric material. There are basically two parameters for the waveform: the wave amplitude and the length, both of them schematically represented in figure 3.1.

Several actuating waveforms can be designed, some examples are also represented in the figure 3.1, but the result will depend on the two parameters mentioned above.

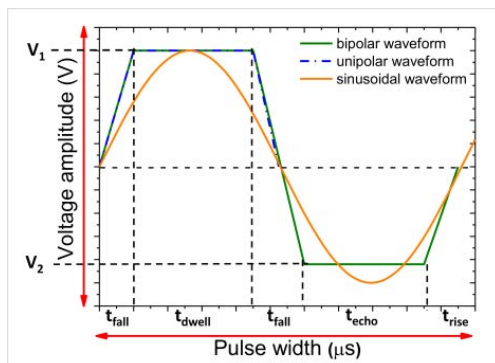


Figure 3.1: Schematic representation of an unipolar, a bipolar and a sinusoidal waveform.

MicroFab piezoelectric actuator consist of a lead zirconate titanate (PZT) material which works in a squeeze mode: the tube, which is polarized radially, is expanded or contracted (depending on the polarization) when a voltage differential is applied. The liquid oscillation resulting from this movement will result in the generation of a single drop for every pulse.

The wave amplitude is determined by the driving voltage, and determines the strength which will squeeze the liquid column, giving inertial momentum to the fluid. This inertial force must surpass the viscous dissipation in order to break the liquid thread, that once in the air will recoil under the surface tension force action to form a drop [114]. The wave width acts on the resonance of the liquid column and it also has effect on the drop volume and speed, shorter pulses will generate smaller and faster drops [115].

In figure 3.2 we show different stages during the drop generation by a piezoelectric actuator.

3.2.2 Ink properties effect on drop ejection and deposition

The main parameters that governs the fluid motion during printing are viscosity, surface tension and density. A short review of these parameters, focusing on their effect on the printing performance, is detailed below.



Figure 3.2: Sequence of images of a drop generated by a piezoelectric actuator.

3.2.2.1 Viscosity

Viscosity can be defined as the internal resistance of a liquid to spread when a shear force is applied. It plays a major role on the drop formation, becoming one of the first parameters to adjust on the ink design. Viscosity affects the drop stability by eliminating oscillations after the liquid thread breakup. Besides a poor drop stability, low viscosity inks will cause an air uptake into the nozzle.

On the other side, for high viscosity inks, the inertial momentum of the liquid will not be enough for the drop breakup due to viscous dissipation. In both cases the drop will not be generated or will be unstable [49].

Experimentally, for a Microfab PZT actuator, the ink must have a viscosity value between $1\text{mP}\cdot\text{s}$ and $20\text{mPa}\cdot\text{s}$ for the proper drop generation.

3.2.2.2 Surface tension

Surface tension is the driving force for the meniscus control and drop shape; it affects the solution wetting on the printhead components. Again, surface tension values must be kept between a certain range, specifically 20 and 70mN/m . A low surface tension can lead to air uptake specially if high drop speed is reached. Uncontrolled drop generation and satellites formation is also an indication of a low surface tension ink. On the other side, a large value on surface tension will difficult the drop formation due to a too high wetting of the inkjet components [49].

3.2.2.3 Density

Density has a direct impact on the energy required for the drop generation due to the larger kinetic energy of a more dense ink with the same rheological parameters. As a general trend, as ink density increases, wider pulses are required to oscillate the liquid column in order to obtain a drop.

3.2.3 Fluid dynamics

The actual drop formation occurs under certain conditions on the described viscosity, surface tension and density. In order to know the correct values that the ink must fulfil when it is being designed, the inkjet community leans on Navier-Stokes equations for the viscous fluid motion description [116]. By these equations we can predict the motion of a fluid with uniform density and viscosity.

The first equation 3.1 describes the fluid velocity field, u , changes over time, correlating the fluid movement over space along with any internal and external force acting on it:

$$\frac{\partial u}{\partial t} = -(\nabla u)u - \frac{1}{\rho}\nabla p + \eta\nabla^2 u + F, \quad (3.1)$$

where $-(\nabla u)u$ is a term originated from the momentum conservation. $-\frac{1}{\rho}\nabla p$ is the pressure term, being ρ the density of the fluid and p its pressure. Finally $\eta\nabla^2 u + F$ is the viscosity expression, being η the fluid viscosity term.

To simplify the mathematics, the liquid incompressibility assumption is imposed, which means that the liquid amount flowing into the chamber is the same that the liquid flowing out. This assumption leads to the second Navier-Stokes equation:

$$\nabla u = 0 \quad (3.2)$$

If the physicochemical fluid properties that govern fluid dynamics, such as density, surface tension and viscosity are included into independent dimensionless parameters, the mathematical analysis becomes plainer. There are three

forces acting on the fluid that are typically important in the drop generation by inkjet printing [117, 118]:

- Inertia: $\rho l^2 v^2$
- Surface tension: γl
- Viscous force: $\eta l v$

Where ρ is the density, γ is the surface tension and η is the viscosity of the fluid, l is a characteristic length (usually the nozzle diameter) and v is the velocity of a body of liquid.

When Navier-Stokes equation is non dimensionalized, the result is a set of well known groups in the inkjet community:

The Reynolds number (Re), which shows the ratio of inertial to viscous forces:

$$Re = \frac{\rho l v}{\eta}$$

The Weber number (We), is the balance between inertial and capillary forces:

$$We = \frac{\rho l v^2}{\gamma}$$

And the last grouping of physical constants is the Ohnesorge number (Oh), which relates the viscous to capillary and inertial forces.

The earliest work on the study of the drop generation mechanism establish this number as the appropriate expression to characterize the drop formation:

$$Oh = \frac{\eta}{\sqrt{\rho l \gamma}}$$

In the inkjet printing field, the inverse of the Oh number (Z) is currently found. It is a characteristic dimensionless number independent of droplet velocity which rates the inertial and surface forces with viscosity:

$$Z = Oh^{-1} = \frac{\sqrt{\rho l \gamma}}{\eta}$$

In the literature we can find some works that tried to define the appropriate working range regarding the Z number. Reis and Derby [119] postulated this range to be $1 > Z > 10$ and a latter work from Jang et al. [88] redefined the appropriated Z value as $4 > Z > 14$.

In any case what these ranges try to delimit is a value where the ink will be too viscous for its deposition (small Z values) or, on the opposite case, the satellite formation will be favoured due to the low ink viscosity, defined by a high Z value.

Further work on the definition of a printable ink lead Dunieveld to suggest a minimum velocity (v_{min}) for the drop ejection depending on the nozzle diameter (d_n) according to the next expression:

$$v_{min} = \sqrt{\frac{4\gamma}{\rho d_n}} \quad (3.3)$$

Derby used this expression in We number terms (using l as the nozzle diameter) together with the Z range defined between 1 and 10 in order to plot the limits of ink printability, represented in figure 3.3 [111].

In figure 3.3 it can also be observed the drop splashing onset, defined by Stow & Hadfiel [120] as:

$$We^{1/2} Re^{1/4} > f(R) \quad (3.4)$$

Where $f(R)$ is function of the substrate roughness. For a flat and smooth substrate this relationship is reported to have values around 50.

3.3 Theoretical parameters of the liquid-substrate interaction

The next step after the drop generation is the impact of that drop on top of the substrate that we intend to print. During the next section we will shortly review the parameters affecting to deposition.

The liquid distribution when the printed drop impacts the substrate and the liquid-liquid interaction of the many deposited drops are affected by the surface

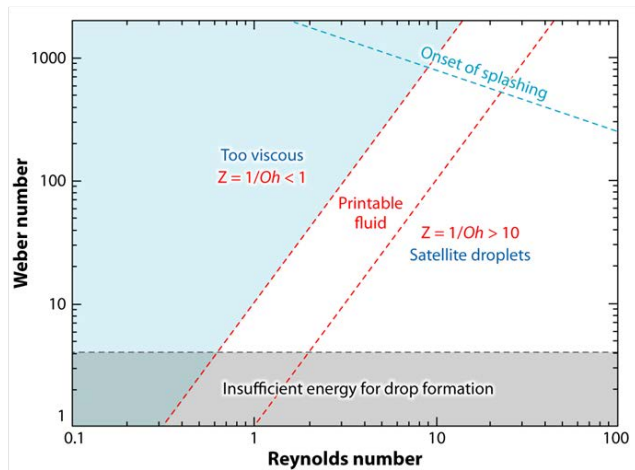


Figure 3.3: Printability limits represented on Derby review from 2010 [111].

energy of the different system components, the drop impact strength and the liquid evaporation [121]. Here we describe the influence of these parameters.

3.3.1 Drop impact

An impacting drop on a substrate is a complex system controlled primarily by capillary, gravitational and inertial forces [122].

Again, We , Re and Oh numbers are commonly observed to predict the ink behaviour. For the effect of a falling drop, usually the Bond number (Bo) is also taken into consideration,

$$Bo = \rho g a^2 / \gamma,$$

where g is gravitational force. But due to the small volume, surface energy and density of the drops ejected by inkjet printing, gravitational forces are neglected ($Bo \ll 1$). Thus the dominant forces for inkjet printing drops will be capillarity and inertia.

Schiaffino & Sonin studied the impact of relatively low We number drops on a substrate. They defined that the drop behaviour on impact could be driven by inertial or capillary forces, the transition between regimes depending on a

critical We number. They also considered the resistance of the impacting drop to spread depending on Oh number [123].

Summarizing, what we have in inkjet printing depositions are low viscosity inks with relatively high We numbers. From what was said before, this means that the deposition will be governed by an impact driven spreading.

3.3.2 Wetting

A good ink wetting for a specific substrate is a mandatory issue controlled by liquid-solid interaction and it is a requirement to obtain an homogeneous coating.

The wetting of an ink on top of a substrate results from the intermolecular interactions between the two systems. The ink wettability (wetting degree) will be a result of the adhesive forces that will make the fluid to spread vs the cohesive forces which will force the liquid to recoil minimizing the surface. This forces balance depends on the interfacial tensions of the system [124–126].

Contact angle measurement is an easily performed method to determine the relation between the adhesion and cohesion of a fluid. This measurement uses the angle defined between the substrate and the tangent of the drop just where the solid meets the liquid.

The contact angle of a liquid drop on a solid surface is defined by the mechanical equilibrium of the drop under the action of three interfacial tensions: solid-gas, γ_{SG} , solid-liquid, γ_{SL} , and liquid-gas, γ_{LG} by Young's Equation:

$$\gamma_{SG} - \gamma_{SL} - \gamma_{LG}\cos\theta_C = 0 \quad (3.5)$$

Where θ_C is the contact angle:

When the contact angle takes values lower than 90° , we can say that adhesive forces surpass cohesive forces and the fluid wets the solid, being a $\theta_C=0^\circ$ the perfect wetting (which is not necessarily the optimal wetting).

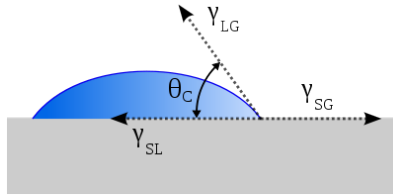


Figure 3.4: Contact angle scheme.

3.3.3 Liquid redistribution: Coffee stain effect

When a coffee drop is dried on top of a substrate, it leaves a dense solid ring at the drop perimeter. This is the result of the free surface constraining by a contact line, that moves the liquid outward to compensate the losses from evaporation [56, 59].

In the inkjet printing deposition of thick films, this phenomenon can be found in several scales:

- **On a single deposited drop:** After the deposition of a single drop we can observe the most typical case of the coffee stain effect. Still, there is a low probability to find the effect on a single drop since the ejection frequency is of hundreds of drops per second, so there is not enough time for drops to evaporate.
- **On a single line:** The coffee stain can also be present after the deposition of a line. Once a line is deposited, there is a time delay (around one second) while the liquid can be evaporated and redistributed given the small deposited volume. For this reason it is important to avoid evaporation during the deposition for several lines by using high boiling point solvents or additives that keep the film wet.
- **On a full deposited film:** The last case where we observe liquid redistribution due to the coffee stain effect is after the full deposition of a film, if the liquid has a low evaporation rate. If the film is completely wet it acts as a whole deposited drop, being the substrate borders a more effective contact line than the one found in a drop on top of an infinite substrate.

In figure 3.5 we show the coffee stain effect for the three cases described above.

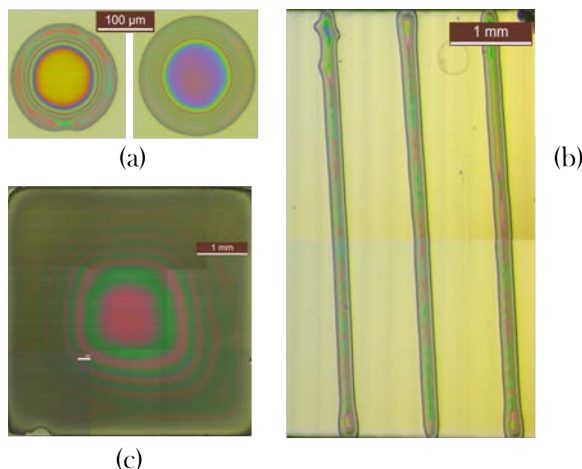


Figure 3.5: Coffee stain effect accumulation found on: (a) The perimeter of the drop on a substrate; (b) The edges of printed lines; (c) The perimeter of a whole deposited film.

3.4 Organometallic YBCO ink deposition

Along this section we will apply the described theoretical concepts. We will study how to modify the ink composition to improve the deposition homogeneity. In addition, we will show how to tune the waveform to obtain a stable drop or to change the drop parameters for a better deposition.

The different results in this section were obtained using a single nozzle MicroFab PZT dispenser.

The samples are printed line by line, moving a motorized platform in two perpendicular axes (X and Y) while the nozzle remains fixed. The X axis corresponds to the line printing direction, and it has a movement speed of 1cm/s. The Y axis is the lateral step that the platform makes once the line in X axis is completed. A schematic representation is shown in figure 3.6.

Although we work with a drop on demand system, the drops are constantly being generated at a certain frequency in the order of hundreds of drops per second. It can be noticed in figure 3.6b) that the lines in X direction end outside the substrate. This prevents on the one hand the drops generated in the time lapse in the lateral step (~ 1 second) to be deposited on top of the substrate, and on the other hand guarantees that the platform velocity is constant while the nozzle is over the substrate.

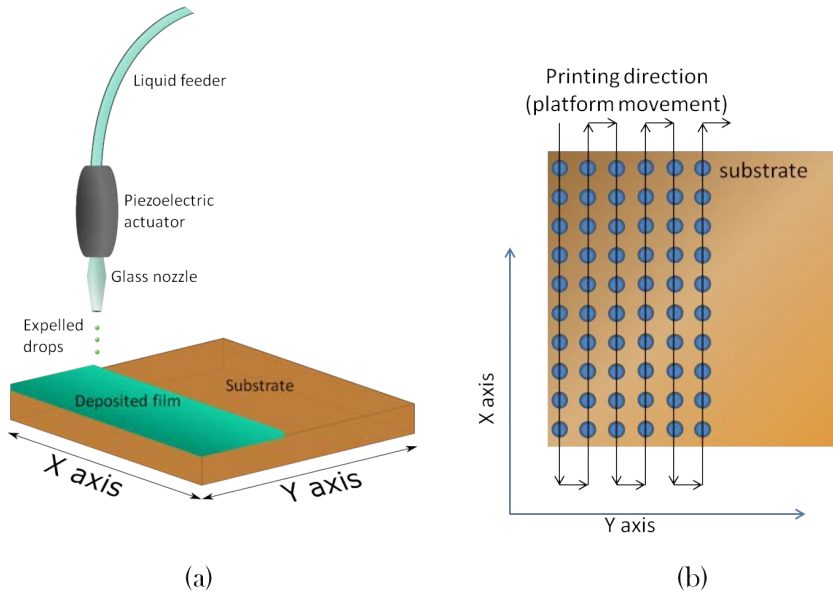


Figure 3.6: Schematic representation of single nozzle printing motion and of the reference axes. Blue circles represent deposited drops. We refer as "line" to the set of drops deposited in the X axis.

The drop pitch refers to the drop distances in micrometers for X and Y axes. We use the nomenclature "(XxY)" being X the drop distances in the axis X in μm and Y the drop distances on the axis Y in μm . Thus, (25x50) represents a matrix with a drop distance of $25\mu\text{m}$ on X and $50\mu\text{m}$ on Y.

3.4.1 Ink design

Before starting with the discussion of the results, in table 3.1 we present the different solutions used along this chapter and the criteria used for the choice of these formulations for the precursor solutions of thick superconducting films.

To remind the used nomenclature depending on the used solvent, the next table is rewritten:

Solution name	Solvent 1 (% V/V)	b.p. ($^{\circ}C$)	Solvent 2 (% V/V)	b.p. ($^{\circ}C$)
4B	Methanol (74)	64.7	Propionic acid (26)	141.2
4C	Propionic acid (100)	141.2	—	—
4D	Ethanol (100)	78.2	—	—
4G	Butanol (80)	117.7	Propionic acid (20)	141.2

Table 3.1: Solution nomenclature (b.p. being boiling point).

The basic criteria for the design of these solutions were:

- Precursor organometallic salts solubility - Up to solutions at 1.5M (sum of salts).
- Wettability - On $LaAlO_3$ and metallic substrate with oxide buffers.
- Water absorption - The solution water content must be kept below a 1.5% $_{wt}$.
- Viscosity - The solutions require a viscosity value between 1 and 20 mPa·s.
- Volatility - As will be explained latter on, the solvent boiling point is critical to obtain an homogeneous deposition. It cannot surpass 150 $^{\circ}C$ in order to not interfere with the pyrolysis process.

In table 3.2 we show the different ink parameters as well as Ohnesorge and Z numbers typically used to characterize the ink.

As can be observed from the different ink parameters, some values are out of the range $4 < Z < 14$ defined by Jang. What indicates a Z value above 14 (as

Solution	Density $\rho(g/mL)$	Viscosity $\eta(mPa \cdot s)$	Surface tension $\sigma(mN/m)$	Contact angle θ ($^\circ$)	Re We Oh	Z
4B 1.5M	1.12	12.00	25.12	33.7	0.29	3.4
4B 0,5M	0.89	1.08	22.44	12.5	0.03	32.1
4C 0,5M	1.02	1.67	25.37	<5	0.04	23.6
4G 0,5M	0.95	4.05	25.26	5	0.10	9.4
4G 1M	1.06	9.0	25.35	10	0.17	5.8

Table 3.2: Ink parameters for the different solution compositions and concentrations.

is the case for 4C) is a higher tendency for satellite formation. Even though, as we will show, due to the proper waveform tuning we were able to obtain a stable drop for all the described compositions for long time periods.

After this introduction, we proceed to explain how the different solution compositions were printed and their performance in the deposition on top of single crystal substrates and metallic substrates.

3.4.2 Solution deposition study with inks optimized for spin coating deposition

Up to now, the 4B composition has been the reference solution used in SUMAN, for the thin low fluorine films (250nm) deposition by spin coating [27]. This solution was designed to achieve the optimal parameters for the deposition of spin coating technique. Since the deposition of low fluorine thick films by inkjet printing is a novel topic in our group, the optimal ink composition for these films must be established.

A fast solution composition screening was performed on top of different substrates. The objective was to decide the most suitable ink for the deposition of films with a thickness range of 700-1000nm

The optimized solution used for spin coating deposition of low fluorine films was 1.5M 4B with 5% $_{V/V}$ TEA composition. For this reason 4B solution was the first to be tested. For inkjet printing, the concentration of the solution was decreased from 1.5M to 0.5M with methanol due to the solution high viscosity

($Z < 4$) and since the drop spacing required for a concentration of 1.5M was too large for the drops to properly merge and to avoid a too swift film drying induced by the small liquid volume.

The first test with this composition resulted in large inhomogeneities following a stripped pattern on both LAO and metallic substrates (Figure 3.7).

A film displaying this inhomogeneous liquid distribution would be hardly epitaxial due to the huge thickness differences. Even if it could be grown epitaxially, the film discontinuity will block any pass of current if these films were grown; an homogeneous film deposition is mandatory to achieve a high performance superconductor.

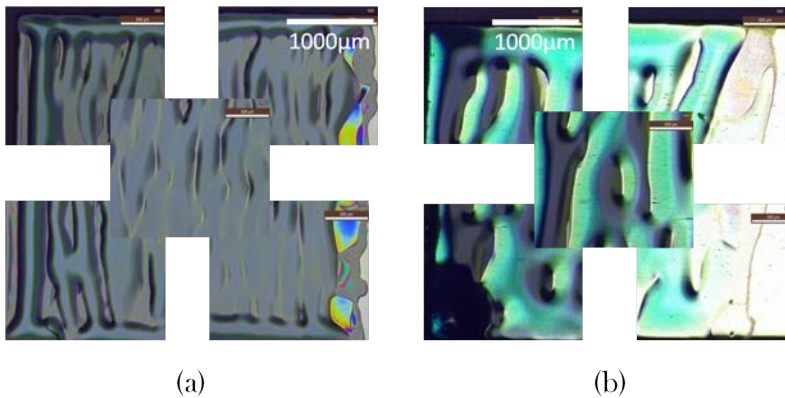


Figure 3.7: Liquid distribution for a 4B 0.5M solution deposited with a drop pitch of $17 \times 17 \mu m^2$ (estimated thickness after growth of 1000nm). The solution was deposited on top of (a) LAO single crystal and (b) Buffered metallic substrate from Bruker.

In order to understand this inhomogeneity, 4, 8, 16 and 32 lines were deposited with a drop pitch of $18 \times 18 \mu m^2$ using 4B 0.5M with 5% $_{V/V}$ TEA solution. The experimental results are displayed in figure 3.8.

When 4 lines are printed, it can be observed that the liquid covers more than $500 \mu m$ on Y axis. Taking into account that the nozzle is moved only $72 \mu m$ ($18 \mu m \times 4$ lines), we conclude that the deposited liquid is spread further away from the nozzle position.

As a result of the fast evaporation of the ethanol, after several lines the liquid is dragged on top of the already dried solution. This leads to the liquid accumulation at the beginning of the printing design by the action of capillary forces.

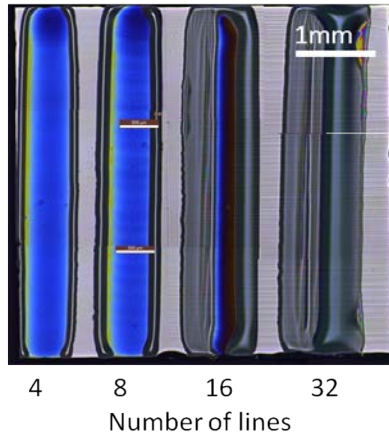


Figure 3.8: 4B 0.4M printed bands resulting from the deposition of several lines (according to the scheme presented in fig 3.6). From left to right, 4, 8, 16 and 32 lines were deposited with a drop separation (pitch) of (18x18). In the bands deposited with 16 and 32 lines, the liquid inhomogeneity formation can be observed.

Several drop pitches were tested in order to increase the volume of liquid to delay the solvent evaporation (closer drops) or to decrease the drop overlapping (more separated drops). We did not observe any improvement.

3.4.3 4B ink composition tuning for thick films deposition by inkjet printing

We increased the propionic acid proportion from 9% to 26% in order to slow down the solvent evaporation, since this acid has a boiling point of 141.2°C. With this formulation modification, the stripes disappeared on behalf of a complete and homogeneous wetting.

In addition, removing of the triethanolamine (TEA) additive, classically

used in SUMAN group to increase viscosity and the precursor salts stability [27], further improvement of the film homogeneity was observed.

By using propionic acid as the only solvent and removing the TEA from the composition we obtained the most satisfying result for the initial 4B composition.

In table 3.3 we describe the tested ink formulations and their effect on the deposition homogeneity.

To illustrate our assessment, in figure 3.9 we display the optical microscope images of the films resulting from the deposition of each ink from the table 3.9.

	Solvent1 (%)	Solvent2 (%)	Additive (%)	Deposition homogeneity
1	Methanol (86)	Propionic acid (9)	TEA (5)	Highly inhomogeneous deposition; substrate not fully wet.
2	Methanol (69)	Propionic acid (26)	TEA (5)	Inhomogeneous deposition; liquid recoiling and coffee stain effect.
3	Methanol (70)	Propionic acid (30)	—	Improved homogeneity, still not full substrate wetting.
4	Propionic acid (100)	—	—	High homogeneity, still some liquid accumulation; full substrate wetting

Table 3.3: Effect of the ink composition on the deposition homogeneity for 4 different ink formulations

The new composition (experiment 4 in table 3.3; figure 3.9 (d)), with propionic acid as the only solvent, was renamed as 4C. In figure 3.10 the deposition of this new solution on LAO is presented, showing a complete wetting and a greatly improved homogeneity.

3.4.3.1 Drop generation and reproducibility for 4C ink composition

We described the required ink parameters (We, Re and Oh numbers) to obtain a good deposition. We mentioned that the Z number (Oh^{-1}) range to

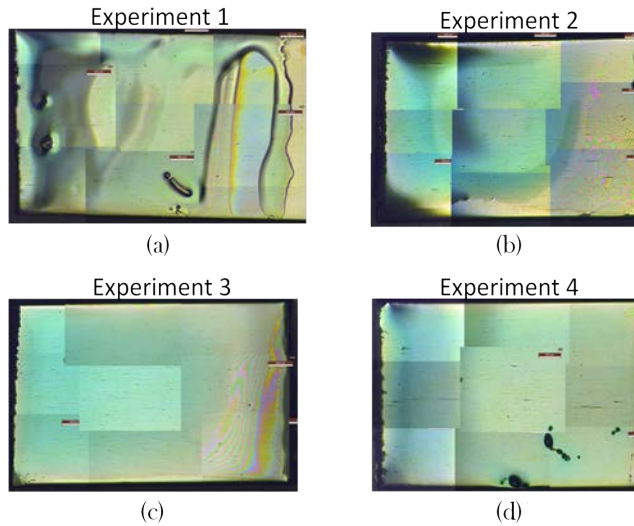


Figure 3.9: Effect of the ink composition on the deposition homogeneity on a Bruker buffered metallic substrate. The used drop pitch was 17x17 (1000nm of nominal thickness after growth: a) 9% propionic acid, 5% TEA. b) 26% propionic acid, 5% TEA. c) 30% propionic acid, 0% TEA. d) 100% propionic acid, 0% TEA (4C)

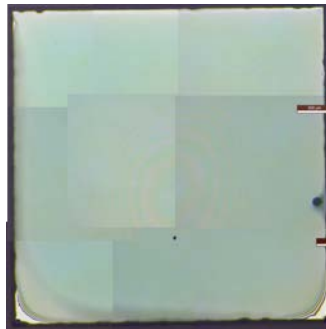


Figure 3.10: Optical microscopy image of a film after deposition on LAO using a 4C 0.5M solution (100% of propionic acid). The used drop pitch was (22x22), a nominal thickness of 700nm after growth.

generate a stable drop without satellites was between 4 and 14. However, the Z number value for 4C 0.5M solution is 25, which is in the range of satellite formation defined in figure 3.3 due to its low viscosity. Even so, the satellite

formation could be easily avoided by tuning the waveform parameters in order to tune the inertial factor.

The printing parameters used for 4C 0.5M were: Pulse length = $53\mu\text{s}$; pulse width = 23V,-13V.

In figure 3.11 we display the drop volume calculated for 27 days, always with the same waveform parameters, demonstrating that a reproducible drop volume can be obtained within $\pm 10\%$ of deviation. With these conditions, the printing was proved stable for hours without satellite formation.

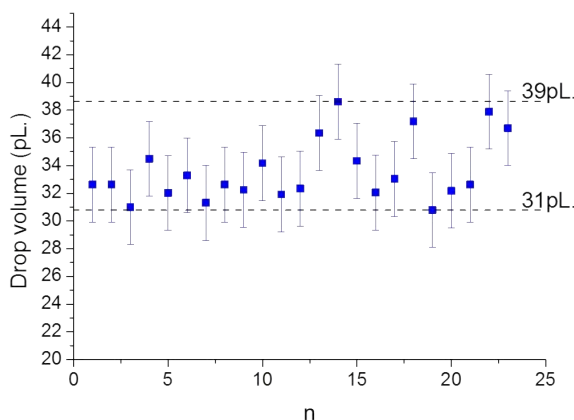


Figure 3.11: Drop volume reproducibility of drops generated using a 4C 0.5M solution. A difference of 1pL. implies 20nm of difference on the thickness of the grown film.

With 4C composition, the wetting is greatly improved respect the previously tested inks. However, the homogeneity of the films deposited with this composition still required further improvement. During the deposition, the liquid distribution is homogeneous, but during drying, the liquid is redistributed to the substrate edges, forming the well known coffee stain inhomogeneity.

In figure 3.12 the effect of the liquid movement on the film after deposition and pyrolysis is shown.

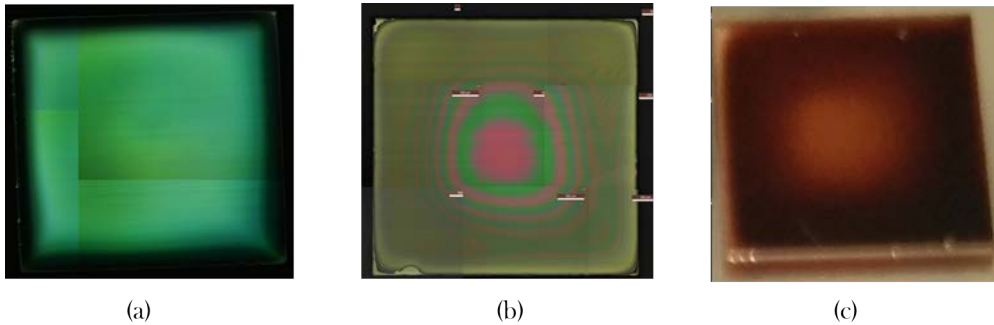


Figure 3.12: Coffee ring effect observed for films deposited with 4C 0.5M ink formulation. (a) Optical microscope image after deposition. (b) Optical microscope image after pyrolysis. (c) Conventional film of a pyrolyzed film. The coffee stain effect can be observed on the three images

3.4.4 Ink composition change to improve liquid distribution homogeneity

Since we observed large liquid movements in the 4C solution, we tried to modify the ink composition in order to enhance the deposition homogeneity.

We made two assumptions which we thought that could lead to better deposition performance of the solution 4C:

1. The homogeneity is improved due to a single solvent ink composition. The presence of several solvents may lead to liquid movements due to surface tension gradient (i.e. Marangoni effect) [56, 127, 128].
2. The high boiling point of the propionic acid (compared with methanol boiling point) leads to a slower drying. This solution does not dry during deposition, avoiding therefore the liquid movement due to solvent evaporation before the deposition is complete.

3.4.4.1 Single solvent approach

One possible hypothesis was that homogeneity enhancement was caused by the presence of a single solvent. To test this hypothesis a solution with methanol as the only solvent (4D) was deposited, using Ba and Cu propionates and $Y(TFA)_3$ as organometallic precursors.

This solution based on a single low boiling point solvent was deposited using the following waveform parameters: Pulse length = $40\mu\text{s}$; pulse width = 20V,-10V. The generated drop had a volume of 23pL., the smallest drop generated until now.

Several drop pitches were tested: (12x12), (16x16) and (20x20), with nominal thickness after growth of 1400nm, 780nm and 500nm respectively.

As can be observed in figure 3.13, the printing with the 4D demonstrated a strong increase of liquid distribution inhomogeneities.

This evidenced that the 4C homogeneity improvement was caused by the higher solvent boiling point respect 4B formulation.

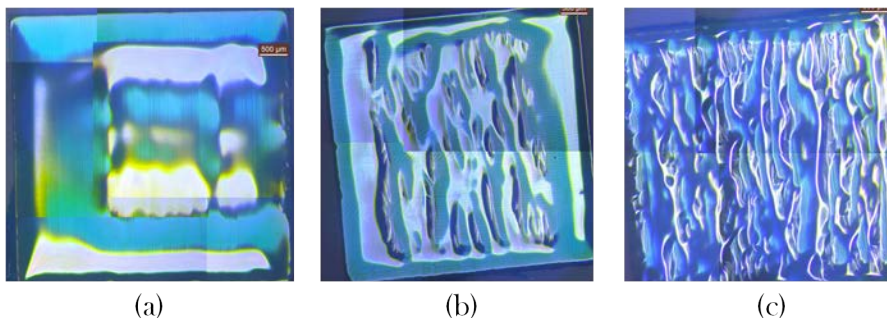


Figure 3.13: Optical micrographs of a 4D 0.5M composition on LAO substrate using different drop pitches: a)(12x12) for a nominal thickness of 1400nm after growth, b)(16x16) for 780nm and c)(20x20) for 500nm. All the depositions presented huge liquid inhomogeneities.

3.4.4.2 High boiling point approach

To demonstrate if the high boiling point of the propionic acid (141.2°C) is causing the higher film homogeneity, we designed an ink substituting the $80\%_{V/V}$ of the solvent for butanol (b.p. 117.2°C). This ink composition is referred as 4G.

The rheological parameters differ significantly from 4C solution (as can be observed in table 3.2), being 4G a solution more viscous and with larger contact

angle than the former solution. These two facts are important in order to avoid the huge liquid movements found in 4C composition [51].

A 4G 0.5M ink was deposited by inkjet printing. A stable drop was obtained using the following waveform parameters: Pulse length = $55\mu\text{s}$; pulse width = 30V,-15V. The resulting drop had a volume of 45pL.

To test the performance of this solution, several drop pitches were used ranging from (18x18) (1200nm of nominal thickness after growth)to (24x24), 680nm after growth.

The deposition of 4G 0.5M ink composition leads to films with a similar homogeneity degree to the films deposited with 4C 0.5M, demonstrating the need of high boiling point solvents.

The coffee ring formation is still a problem during the film drying, but a different liquid movement mechanism is observed. In addition, the 4G solution presents liquid movement during the deposition, where the liquid is moved to the first printed line, displaying a "C" shaped inhomogeneity. In the next section we will observe the formation of this inhomogeneity.

In figure 3.14 we display a film with the "C" shaped inhomogeneity (3.14a) besides an homogeneous film (3.14b). Both images are optical micrographs of pyrolyzed films where thickness differences are more clearly observed.

Again, the deposition homogeneity vary depending on the printing conditions(humidity, temperature, solution homogeneity and solution water content).

Still there are advantages on the 4G composition respect 4C. Since the solution is based in an alcohol, 4G presents a higher suitability for multinozzle printheads respect 4C.

Another advantage of 4G composition is a minor liquid spreading compared with 4C as it can be observed in figure 3.15. This factor is important when we want to print defined lines (i.e. patterning). In addition, having an alternative solution based in alcohol with a good printing performance opens a route to improve the solution through additive incorporation, as will be observed in chapter 5.

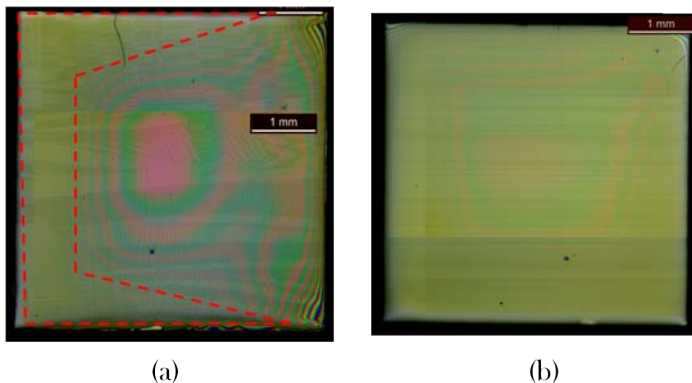


Figure 3.14: 0.5M 4G ink composition deposition homogeneity after pyrolysis. (a) Inhomogeneous deposition. The "C" shaped accumulation is surrounded with the dashed line. (b) Homogeneous deposition.

3.5 Drop merging study

We have shown the different inhomogeneities formed during deposition, depending on the ink composition. In order to understand the mechanism of liquid movement and to avoid the liquid distribution inhomogeneities, we performed a deeper study on the merging of drops.

In our inkjet system we define two printing directions, X and Y. In X direction we have a swift drop deposition, just with a few microseconds (from 1 to 10 depending on the required drop spacing) between drops. On the other side, the time lapse between two neighbour drops on the Y direction, varies from 2 to 3 seconds. In figure 3.16 we recall the printing scheme to facilitate the experiment description.

3.5.1 Merging study on X axis: Merging of drops

We started the study of the drop merging printing only lines in X direction. 4C and 4G solutions with a concentration of 1M were used for the study. For 4C solution we obtained a drop volume of 50pL. while for 4G the drop volume was 78pL.

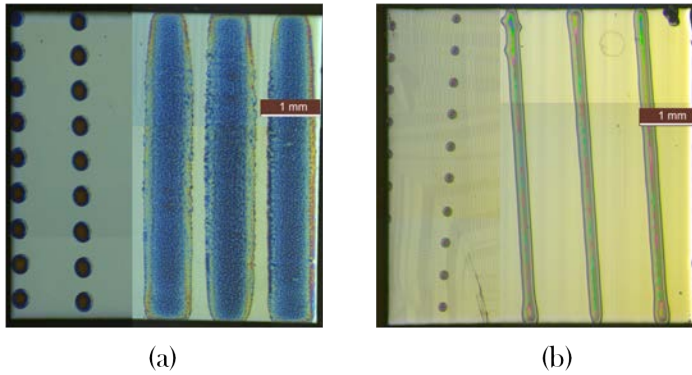


Figure 3.15: Liquid spreading comparison between 4C and 4G ink formulations using 1M concentration. The images corresponds to optical micrographs of a film printed using a drop spacing (pitch) of (500x1000) on the left and (50x1000) on the right. (a) Printing of 4C 1M solution and (b) Printing of 4G 1M solution. The larger spreading for the 4C solution can be clearly observed.

For the study on the X axis the used drop spacing in the X direction was 500, 200, 100, 75 and $50\mu\text{m}$ while the distance in Y was kept constant at $1000\mu\text{m}$.

From the study of the drop merging on X for both solutions, as it can be observed in figure 3.17. We concluded that, when the drop spacing is shorter than the drop diameter, the drops perfectly merge forming a continuous line.

From the merging study in the X axis we can observe important differences between the two compositions.

Despite having a smaller drop volume, the drop impact deposited by 4C solution presents a diameter of $315\mu\text{m}$ while the 4G drop impact diameter is $160\mu\text{m}$.

Another difference is a minor liquid movement to the edges observed in the drops and lines deposited with the 4C solution.

3.5.2 Merging study on Y axis: Merging of lines

From the drop merging experiment we conclude that the drop merging in X direction is homogeneous for the required drop distances for the thick film

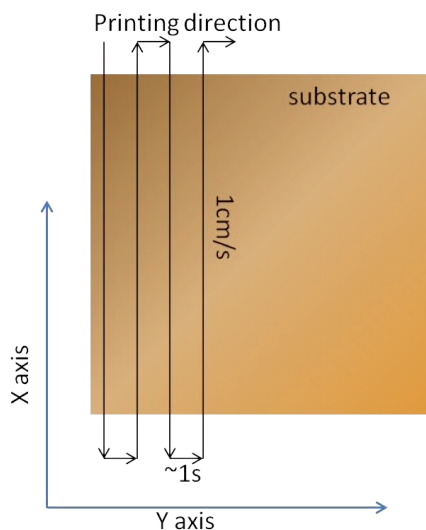


Figure 3.16: Scheme of the printing motion.

synthesis (from 15 to $100\mu\text{m}$ of drop separation).

Since it seems that the source of inhomogeneity comes from the Y direction we studied how the lines merge. The strategy consisted on printing lines (X direction) with a constant drop spacing of $50\mu\text{m}$, changing the distance on the Y axis.

3.5.2.1 Line merging study for 4G ink composition

The merging of lines using the 4G ink with a concentration of 1M is presented in figure 3.18.

We used a drop separation in X of $50\mu\text{m}$, obtaining thin, well defined lines when the separation among lines was of $1000\mu\text{m}$.

Interestingly, when the lines are printed closer, the line loses the definition: when the lines are printed at a Y distance of $500\mu\text{m}$, they become spread, even if there is not direct contact among lines.

This spreading flows towards the first printed line, as can be observed in the samples with Y distances below $200\mu\text{m}$, generating the "C" shaped inhomogeneity. This effect is not so drastic for films deposited with a 4G 0.5M

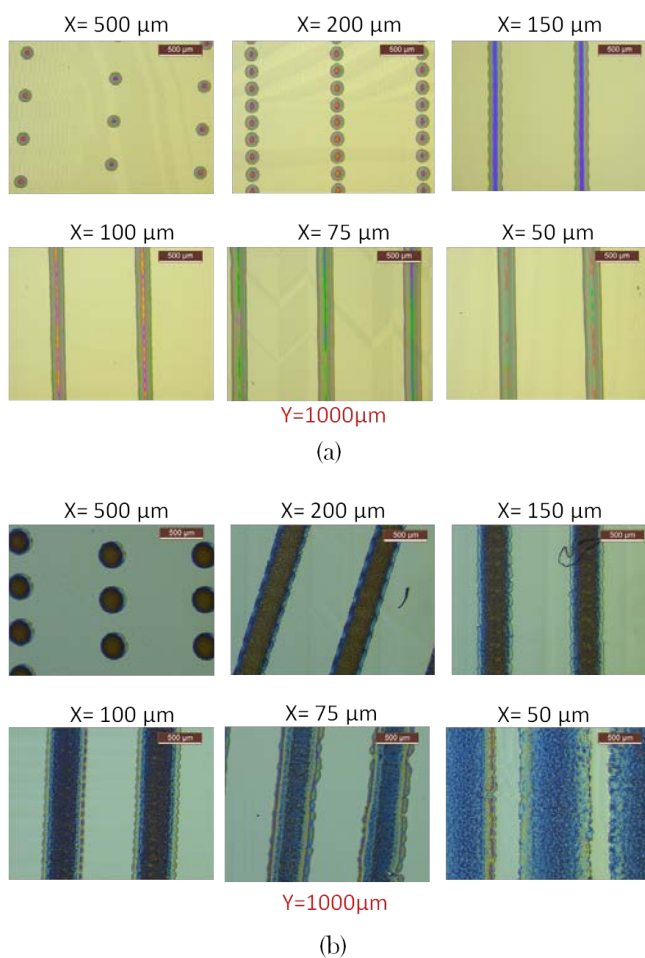


Figure 3.17: Optical microscope images of the merging of drop study performed for (a) 4G 1M solution and (b) 4C 1M solution. The drop spacing in Y is 1000 μm for all the samples. The drop spacing used in X direction is noted above each image.

solution, as could be observed on previous examples of films deposited with 4G 0.5M ink.

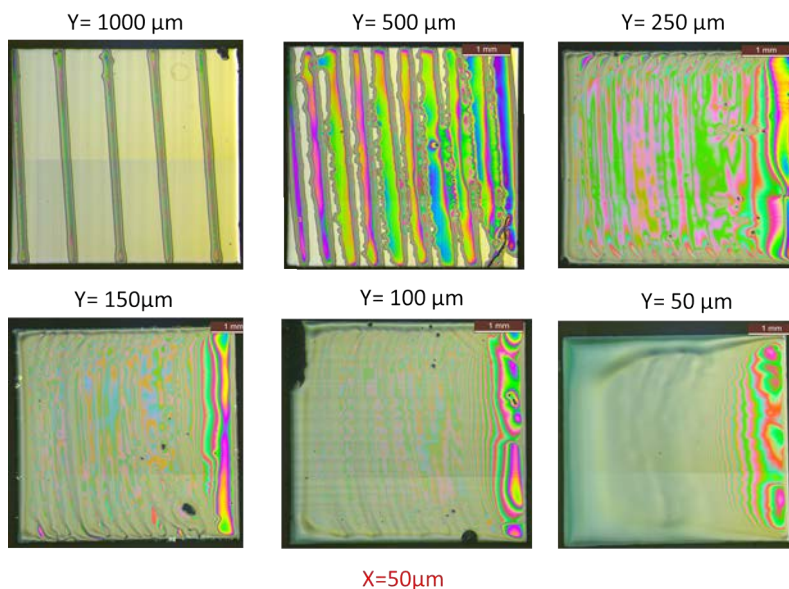


Figure 3.18: Line merging study of a 4G 1M solution using a constant drop spacing in X direction of 50μ . Above the optical microscopy images the drop spacing used in Y is indicated. From the images the liquid movement towards the first deposited line can be observed already in the (50x500) sample

3.5.3 Drop merging for 4C ink composition

As we have shown before in figure 3.17, the 4C 1M ink composition becomes widely spread when is deposited in a LAO substrate.

When the distance in Y axis is moved from 1000μ to 500μ , the substrate is completely covered by the ink. The results of the line merging are shown in figure 3.19.

For closer distances on Y axis we observe a full covered substrate with an homogeneous film.

From these experiments, we conclude that the liquid inhomogeneities on the deposited films using 4C solution are a consequence of the liquid movement

during the drying step due to the coffee ring liquid redistribution.

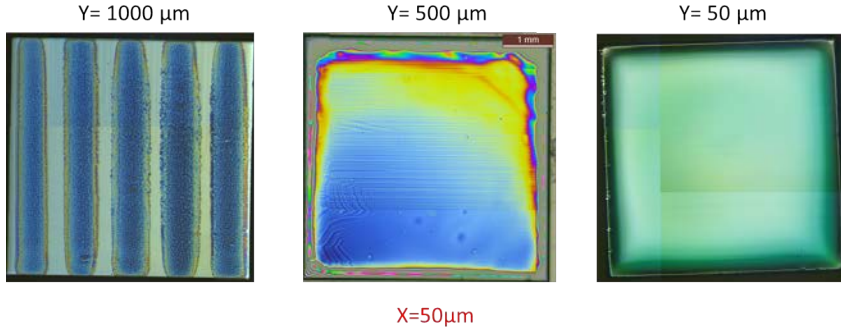


Figure 3.19: Line merging study of a 4C 1M solution using a constant drop spacing in X direction of 50μ . From left to right, the drop spacing in Y was 1000μ , 500μ and 50μ .

From the liquid merging study we could observe the source of inhomogeneities for 4C and 4G solutions.

With 4G the liquid is moved during the deposition, the liquid flows towards the first deposited line, forming a liquid accumulation in a "C" form. When the 4G concentration is reduced from 1M to 0.5M, the liquid homogeneity is greatly improved, as we observed in figure 3.14.

On the other hand, the 4C solution deposited as drops and lines becomes very spread. During the deposition the liquid is homogeneously distributed on the substrate, even if only a few lines are deposited, indicating the high liquid mobility of the 4C ink. The films deposited with 4C become inhomogeneous during the drying step.

3.6 Deposition parameters optimization

After the design of the most suited ink composition for the thick film deposition, we need to establish the optimal deposition parameters.

In this section we will show how to modify the drop volume by tuning the waveform parameters and its effect on the film homogeneity. Also we will explain the effects of the substrate type and the film drying process on the deposited liquid distribution.

3.6.1 Waveform effect on the drop volume and drop speed

As explained before, the piezoelectric actuator is regulated through the waveform. Drop speed and drop volume can be modified depending on the amplitude and length of the driving electrical pulse. For this work, a bipolar wave has been used to actuate the piezoelectric material.

The driving voltage determines the strength that will squeeze the liquid column, giving inertial momentum to the liquid. If the voltage is high enough, the liquid thread will break generating the two possible situations illustrated in figure 3.20:

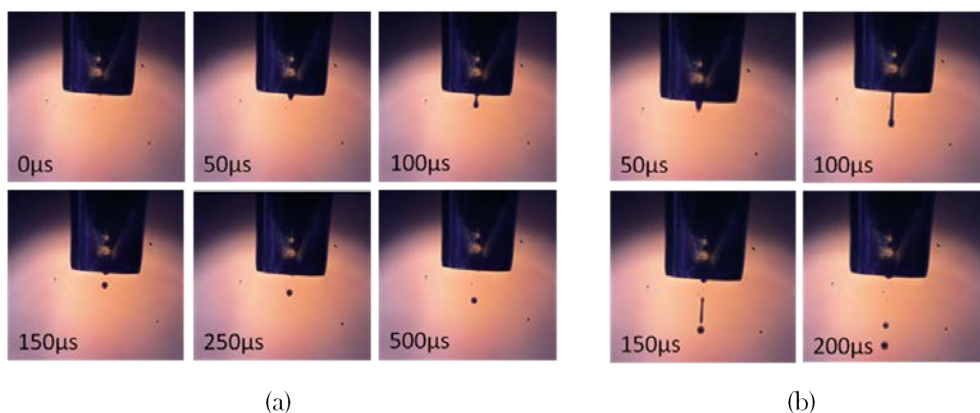


Figure 3.20: Liquid redistribution after the liquid thread breaking: a) Optimal situation with a single drop generation; b) Satellite formation after the thread breakup in several parts.

- (a) The liquid thread recoils due to the surface tension action in (almost) spherical single drops (3.20a).

(b) The thread is divided in several drops, generating satellites (3.20b).

An ink with higher surface tension and viscosity values leaves a wider window to avoid satellites formation [129].

The drop speed and drop volume tuning become of great usefulness for several applications on inkjet printing. The drop overlapping, drop spreading and the liquid evaporation rate are some of the factors that can be modified if the drop speed and drop volume are changed.

3.6.1.1 Drop volume effect on 4G solutions

To demonstrate the drop parameters modification only by the driving pulse action, the following experiments were performed for the 4G 1M solution:

	Wave length (μs)	Wave amplitude (V)	Drop Volume (pL.)	Drop impact (μm)
Experiment 1	23	36; -30	52	148
Experiment 2	49	30; -30	72	150
Experiment 3	70	40; -30	78	162
Experiment 4	90	55; -30	143	211

Table 3.4: Drop volume and impact diameter output depending on the waveform.

It is important to clarify that the degree of freedom on the waveform parameters is small. In practice, the driving voltage that we can select for a specific wave period is in the range of $\pm 3\text{V}$ if we want to obtain a single and stable drop.

In figure 3.21 we show the optical micrographs of the drops generated using the waveform parameters described in table 3.4 after impact on a LAO substrate.

With these experiments, the effect of the waveform parameters on the drop shaping is clear for this ink composition. To observe how the drop volume and drop speed influence the deposition, the drops generated from each experiment

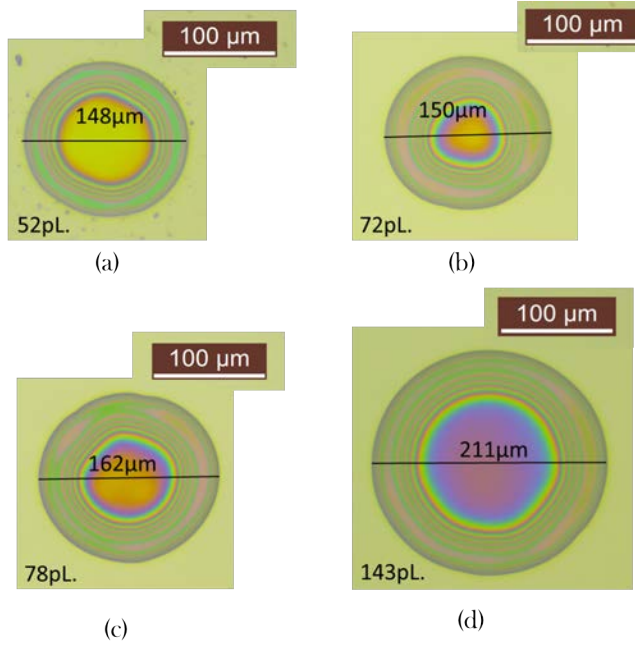


Figure 3.21: Drop impact of 4G solution 1M on a LAO substrate for the experiments presented on table 3.4. The number at the frame bottom corresponds to the drop volume.

were used to deposit a film with a nominal thickness of 700nm after growth.

In order to keep the same deposited liquid amount, the drop pitch must be changed to use a smaller or higher number of drops depending on the drop volume.

For a 4G 1M, the liquid amount required to obtain a specific film thickness after growth, assuming that the film is compact, is calculated from the following expression:

$$Deposited\ Volume = \frac{YBCO\ Volume * \rho_{YBCO}}{[YBCO] * MW_{YBCO}} \quad (3.6)$$

Where $[YBCO]$ is the YBCO precursor solution concentration in Yttrium, ρ_{YBCO} is the YBCO density if it is fully compacted and MW_{YBCO} is the YBCO

molecular weight.

If we use expression 3.6 to calculate the liquid required to deposit a YBCO film with a final thickness of 700nm with a 4G solution 1M, we find:

$$\begin{aligned}
 & \text{For 700nm thickness :} \\
 \text{YBCO Volume} &= \text{substrate surface} * \text{Film thickness} = (0.5)^2 \text{cm}^2 * 7 \cdot 10^{-5} \text{cm} \\
 & [\text{YBCO}] = 0.167 \text{M} \\
 \text{MW}_{\text{YBCO}} &= 666.2 \text{g/mol} \\
 \rho_{\text{YBCO}} &= 6.383 \text{g/cm}^3
 \end{aligned}$$

$$\text{Deposited Volume} = \frac{0.5^2 * 7 \cdot 10^{-5} * 6.383}{0.167 * 666.2} = 1.0 \cdot 10^{-6} \text{L}.$$

$$\boxed{\text{Deposited Solution Volume} = 1\mu\text{L}.}$$

To see the drop volume effect on deposition, a YBCO 700nm film (nominal thickness after growth) was deposited using different drop volumes of a 4G 0.5M solution. All the films were deposited using a square drop pitch, changing the drop pitch (and thus the number of deposited drops) according to the drop volume in order to obtain the same deposited thickness.

In Figure 3.22 the effect of increasing the drop volume is observed. The result is a great homogeneity improvement when the drop volume is increased. The reason of this improvement is the retarding of the evaporation induced by the higher liquid amount deposited per unit of time.

From these experiments we could observe the great impact on the film homogeneity that the drop parameters can have.

3.6.1.2 Drop volume effect on 4C solutions

When 4C solution is used, the drop volume has a minor impact on the films deposition. The reason is the low volatility of the solvent used on the 4C composition, that keeps the film wet until a thermal source is applied to evaporate

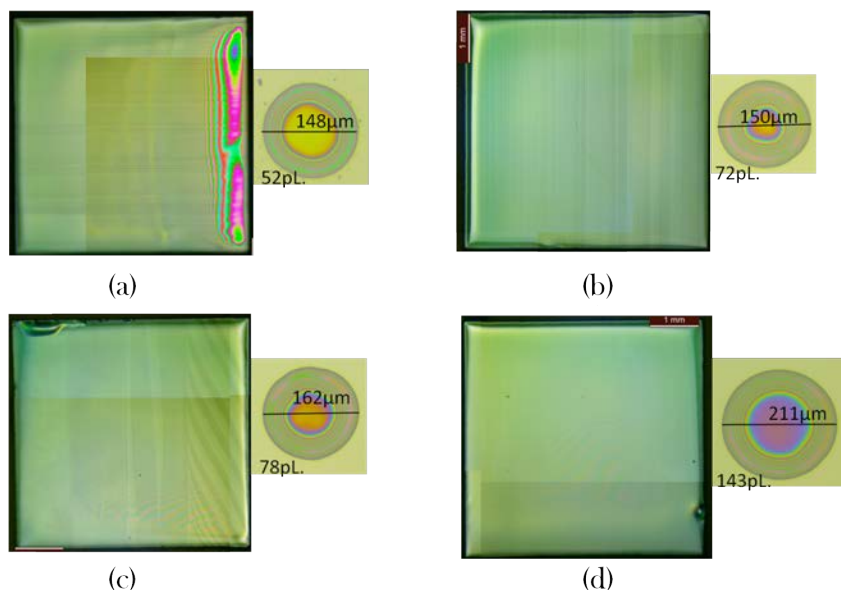


Figure 3.22: Effect of the drop volume on the film homogeneity. Drop pitch was adapted for each drop volume to achieve a nominal thickness of 700nm: a) Drop pitch (36 x 36), number of drops = 19300, drop volume = 52pL.; b)(42 x 42), number of drops = 14200, drop volume = 72pL.; c) (44 x 44), number of drops = 12800, drop volume = 78pL.; c) (60 x 60), number of drops = 7000, drop volume = 143pL.

the solvent.

At this point we have concluded that the homogeneity problem regarding 4C solution cannot be avoided by the deposition parameters since the films proved to be distributed very homogeneously during the deposition. It is when the film is drying that the liquid redistributes towards the substrate edges forming the coffee ring shape.

3.6.2 Substrate effect on the deposition process

The substrate effect on the deposition homogeneity is a consequence of the liquid interaction with the substrate at a molecular level and on the surface morphology of the substrate.

Contact angle analysis gives a measure of the affinity that a substrate has for an specific liquid.

Comparing LAO single crystal and buffered metallic substrates from Bruker, similar contact angle values (θ close to 0°) on both substrates were obtained for all the tested solutions. this indicates that the knowledge generated on the deposition for one type of substrate can be easily transferred to the other type. Nevertheless some differences could be found.

In figure 3.23 we show a deposition of a thick film printed with 4C 0.5M solution on a ABAD (Alternated Beam Assisted Deposition) textured metallic substrate from Bruker with the next architecture:

$\text{Ce}_{0.9}\text{Zr}_{0.1}\text{O}_2/\text{Yttria Stabilized Zirconia}/\text{Stainless Steel (CZO/YSZ/SS)}$,

where the CZO was deposited by CSD while the YSZ by ABAD.

For the deposition on metallic substrates, the liquid is better fixed due to its higher cap layer (CZO) roughness, hindering the coffee ring formation. But we observe a liquid accumulation on the substrate edge where we start to print. This accumulation causes a huge film cracking during the pyrolysis step due to the large film thickness on the edge.

Homogeneity can be greatly improved by starting the printing process 1.5mm away from the film edge as is illustrated in figure 3.23. Still some liquid accumulation is observed at the beginning of the deposition, but after 1mm from the edge, the film homogenizes.

3.7 Film solvent drying

The drying of the film after it is deposited is the main source of liquid distribution inhomogeneities. We opted for a smooth drying to minimize the liquid movement during the solvent evaporation. To dry the film, it was placed on a hot plate at 50°C , heated up to 145°C at $10\text{K}/\text{min}$ and kept at this temperature for 45 minutes.

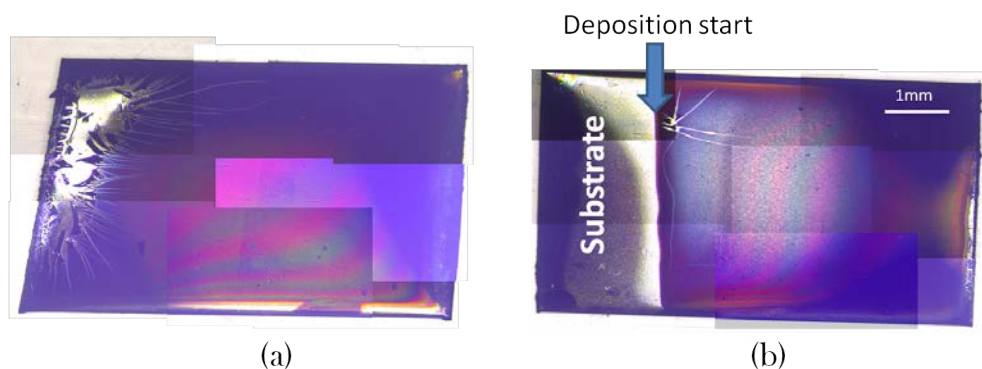


Figure 3.23: Effect of depositing a 4G solution on Bruker buffered metallic substrates (a) starting the deposition from the edge where severe cracking occurs due to an enhanced thickness, or (b) starting the deposition 1.5mm from the edge (b). Optical micrographs acquired after pyrolysis.

In order to see the effect on the mass of such a long drying at this temperature, a thermogravimetric experiment was performed on an already dried film.

From the experiment, only a 4% of mass reduction was detected after 1 hour at 145°C. We can conclude that the film can be dried for long times at this temperature without affecting the pyrolysis process. Thus, to ensure the complete evaporation, the film is dried at 145°C for 45 minutes.

Still, the coffee ring formation could not be avoided, just minimized, specially for 4C ink composition.

In order to overcome the liquid inhomogeneities produced during the film drying, in chapter 5 we will show an approach based on the UV polymerization of an additive during the drying step, which led to very homogeneous films.

3.8 Chapter summary and conclusions

Along this chapter we have shown the efforts done on the design and the deposition of inks adapted to inkjet printing in order to obtain homogeneous

film depositions with a thickness of 700-1000nm after growth. In this section we will gather all the conclusions obtained from this study.

- The solution optimized for the spin coating thin deposition based on the low fluorine precursors route ($\text{Y}(\text{TFA})_3$, $\text{Ba}(\text{AcO})_2$, $\text{Cu}(\text{AcO})_2$) was adapted for the deposition of thick films using the inkjet printing technology.
- The spin coated-designed solution composition was not suitable for the deposition of thick films. From our study we concluded that high boiling point solvents ($>100^\circ\text{C}$) were required. Otherwise, the liquid movements during deposition due to solvent evaporation led to large liquid distribution inhomogeneities.

An ink with propionic acid as solvent (4C) and an ink with a 80% of butanol and a 20% of propionic acid (4G) are presented as effective ink compositions to obtain enhanced homogeneity on the thick film deposition by inkjet printing.

Following this conclusion, the solution concentration was reduced from 1.5M to 0.5M in order to deposit larger liquid volumes, slowing down on this way the film drying.

- The two designed inks showed a full coverage on either single crystals and metallic substrates. Even though, by performing drop merging studies, we could observe that the liquid distribution was quite different for each ink composition:
 - The drop merging study showed that the 4C has a great tendency to spread when it is deposited on the substrate, covering the full substrate with just a small deposited volume. The low volatility together with the fast liquid distribution leads to very homogeneous films during deposition. However, the 4C ink showed a great tendency to form the coffee ring effect during the film drying.
 - On the other hand, the 4G ink composition presented a liquid movement towards the first printed line during the deposition process, originated from the lower solvent volatility.

An advantage of the 4G ink composition respect the 4C is the minor liquid spreading when it is deposited. If the liquid movement can be blocked during deposition of 4G solution, the coffee ring effect is smaller than for the 4C case.

- The driving waveform of the inkjet piezoelectric actuator was adapted to the solution parameters, achieving for both 4C and 4G ink compositions stable and reproducible drops. By changing the waveform we could modify the drop parameters, observing larger drop volumes when the wave pulse and width was increased.

We used the drop volume modification to test the effect of the drop volume on the film deposition homogeneity.

- Performing the deposit with large drop volumes using the 4G ink composition, leads to an enhanced liquid homogeneity. The reason is that the liquid drying is slowed down due to the larger deposited volume per unit of time, avoiding the problems associated to the solvent evaporation.
- There was no effect on increasing the drop volume for the 4C inks, since the films are very homogeneous during deposition. The inhomogeneity on the films deposited with 4C ink is produced during the film drying.
- When we use a buffered metallic substrate from Bruker, a liquid accumulation at the substrate edge is produced, causing a heavy cracking due to the large thickness during pyrolysis at the edge. By printing 1-1.5mm away from the substrate edge, the liquid accumulation is greatly reduced. Besides this accumulation, the printing on metallic substrates leads to less coffee ring formation due to a higher liquid pinning to the substrate. Therefore the knowledge transfer from the single crystal processing conditions to the metallic substrates, regarding the deposition step, is strongly facilitated.
- In order to minimize the liquid movement during the drying step, smooth heating ramps (10°C/min) were performed up to 145°C in order to ensure the complete solvent evaporation.

- Even if the deposition homogeneity was highly enhanced, still the reproducibility in obtaining homogeneous films is quite poor due to the liquid inhomogeneity produced during the film drying.

In order to overcome this problem, in chapter 5 we will present the use of a photo-sensitive varnish additive, which greatly enhances the film homogeneity, and thus large reproducibilities on the synthesis of thick YBCO films could be achieved.

Physico-chemical analysis of the pyrolysis process

4.1 Introduction to the pyrolysis process

Once the deposition is completed, the result is a wet film with the organometallic precursors for the YBCO synthesis. To proceed with the YBCO crystallization, we need to remove the organic mass present in the film. To achieve this, a low temperature treatment (up to 500°C) is performed in order to decompose the metal ligands and additives, leaving the oxide and oxyfluoride compounds that will crystallize on the final product, YBCO for this work. The organic mass firing process is known as pyrolysis.

Only considering the metal ligands (without counting any possible additive), the organic mass volume represents up to an 80% of the total volume as will be shown later on this chapter. The drastic volume reduction during the organic firing is the main thickness limiter for this synthetic route; since the film is clamped to the substrate dimensions, the film can only be compressed in the direction perpendicular to the substrate [61]. An axial stress evolves in the film due to this compression, leading to a structural relaxation that can evolve in crack formation [64].

As we mentioned during the introduction, several works show how only films thinner than 200nm could be obtained without cracks for oxide films [40]. In order to achieve thicker films by CSD, the usual protocol is a multi-coating of several thin pyrolyzed layers until reaching the desired thickness.

Nevertheless, this process is not only time consuming, but it may also deteriorate the final film properties due to the presence of segregated interlayers

[130]. In figure 4.1 we show the cross section difference for a film deposited by multiple coatings and a single deposited film about the same thickness. The segregated interlayers in this case are CuO.

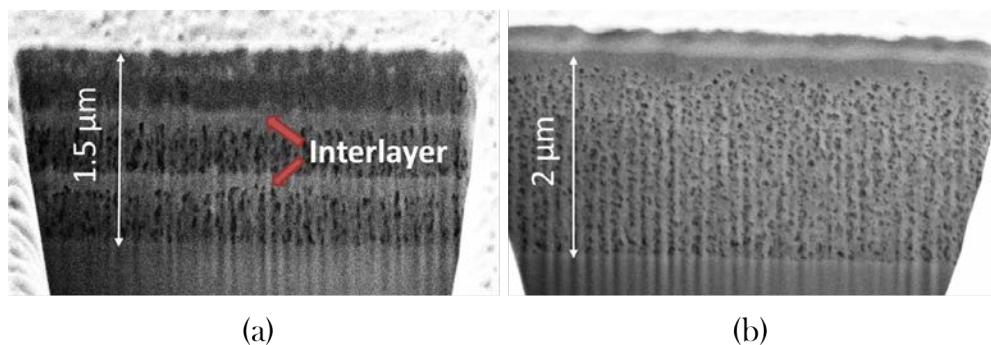


Figure 4.1: Scanning Electron Microscopy (SEM) micrographs of YBCO pyrolyzed films' cross section obtained by Focused Ion Beam (FIB). In (a) 3 coatings of 500nm were performed, with a strong CuO segregated interlayer presence. (b) shows the micrograph of pyrolyzed film with a single coating, presenting an homogeneous cross section.

Some works reported the use of UV radiation in order to decompose the organometallic species at low temperatures avoiding on this way the copper sublimation [131, 132], however, this treatment required the radiation of the sample during long periods of time.

Another used approach, was the pyrolysis of 30nm films to avoid the copper segregation in the interlayers ue the small volume processed [133], but requiring over 30 coatings to reach 1μm thickness.

Although this approaches propose interesting alternatives to increase the YBCO performance of thick films, the time required for this processes becomes a drawback for the industrialization of the process.

Therefore, in order to achieve the best material performances, not only in superconductors industry but also in piezoelectric, photovoltaics and many other functional materials with thickness dependent properties, we require the thickest films, with the best quality in a cost effective process, as it is the

chemical solution deposition. For this reason the films growth with micrometer thickness in one single coating is crucial for these projects.

Along this chapter we will present a thorough study of the physico-chemical properties of the organometallic YBCO precursor films performed on the different parameters affecting the film evolution during pyrolysis. The film morphology, mass, thickness and mechanical properties were analysed by means of several in-situ techniques to determine the critical phenomena that lead to the film buckling and cracking due to stress relief.

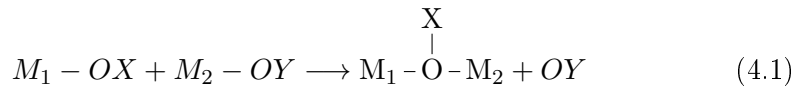
We will conclude showing how to avoid all the sources of inhomogeneity and also we will show that films with a thickness up to $2\mu\text{m}$ after pyrolysis can be obtained without cracks. This is a major achievement in the field of Chemical solution Deposition and it has open the route to use CSD in the production of thick YBCO films.

4.2 Gel shrinkage and stress generation

When a thermal process is applied to the deposited wet film, it starts to change its morphology. The first transformation that the film experiments is the solvent evaporation, which brings the film to a gel state [61].

Brinker and Scherrer defined a gel as "a continuous solid and liquid phases of colloidal dimensions" [63]. In other words, a gel consist of a continuous solid skeleton with cavities filled by liquid connected among them.

As temperature increases, the solvent is completely evaporated and the mass decomposition begins. Since organometallic compounds are good nucleophiles, condensation reactions occurs during this process, specially when thermal decomposition begins. In equation 4.1 we expressed the condensation chemical reaction:



In this expression, M is a metal, X and Y can be either H or an organic chain.

This reaction leads to the (now dried) pores collapsing, causing the film shrinkage. This shrinkage can suppose a loss up to an 80% of the initial thickness. Since the film cannot shrink in the parallel direction to the substrate, the huge thickness loss implies an in-plane stress generation that can reach values in the order of hundreds of MPa [65].

The poor understanding of this critical step, forced many authors to use non-optimized thermal processes (e.g. 24h pyrolysis) or to reduce the film thickness to <200nm in order to avoid the stress producing defect formation [134–137].

In the next lines we will describe in what those defects consist of.

4.2.1 Tensile stress release

When the intrinsic tensile stress overpasses a certain value, the film cracks in order to relax the structure. The layer mechanical properties will determine the critical thickness for the crack formation and propagation according to [43, 62]:

$$t_C = \frac{2G_C E}{Z\sigma^2(1-\nu)} \quad (4.2)$$

Where G_C is the energy needed for the crack propagation, E is Young's Modulus, ν is Poisson's ratio, Z is a dimensionless geometrical parameter and σ is the biaxial tensile stress of the film.

The Young's modulus, also known as elastic modulus, describes the tendency of a material to deform when two opposing forces are applied. Stiffer materials will present higher Young's modulus and, according to equation 4.2, to higher resistance to crack propagation [138].

4.2.2 Compressive stress: Film buckling

Besides the tensile stress generated during the film densification, the film can experience compressive stress. Some examples for the generation of this stress mode would be the film thermal expansion. Some examples are a faster substrate compression than the film or a layer density loss [139, 140].

The observed mechanism for the compressive stress release in thin films is a complex and coherent structure known as buckling. It consist of the film wrinkling with a periodic structure. In figure 4.2 we show Scanning Electron Microscopy (SEM) images that exemplify the huge deformations produced by buckling on a pyrolyzed YBCO film.

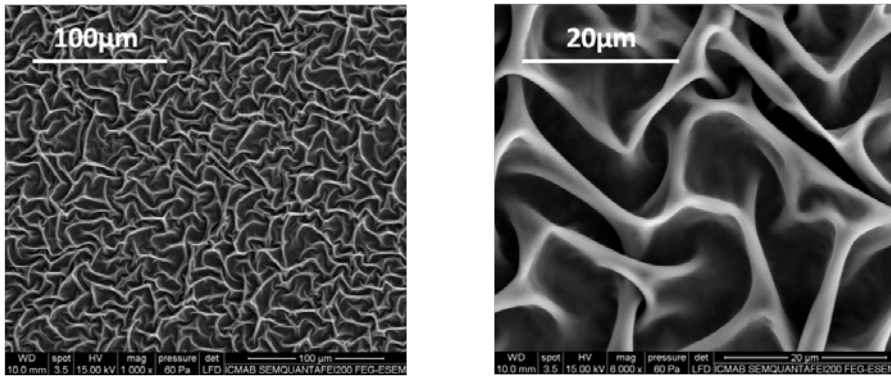
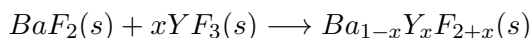
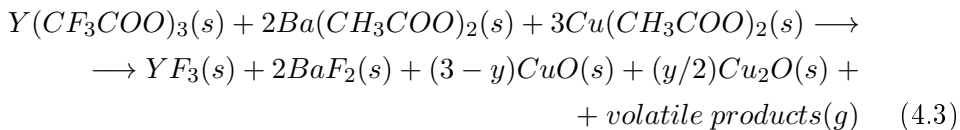


Figure 4.2: SEM images of a film surface buckled after pyrolysis magnified x1000 (left) and x6000 (right). Films deposited using a 4C solution with a nominal thickness of 700nm after growth.

Although this phenomenon results of interest for several applications due to the controlled pattern that results from buckling [141–143], it must be avoided on YBCO processing since it generates randomly oriented layers and decreases the effective area for the current flow.

4.3 Pyrolyzed film requirements

The required film composition before YBCO growth is an amorphous or nano-crystalline matrix resulting from the following reaction: [144]



The ratio between CuO and Cu₂O will depend on the used atmosphere (O₂, N₂).

Along this chapter, the different factors affecting the film during the organic matter decomposition will be discussed, as well as how to handle the stress release phenomena in order to obtain over 1μm homogeneous thick films without cracks or buckling in one single deposition.

The effort on thick film synthesis in terms of film properties during the process and optimal thermal treatment to achieve films without buckling and crack will be described in the next sections.

But the pyrolysis study is not only focused on the parameters affecting the film during the process, mainly furnace conditions and additives. We also have deeply studied the different phenomena influencing the films microstructure. The thickness and mass evolution during the organic firing, as well as the mechanical properties of the film, were analysed to understand and optimize the pyrolysis process in order to obtain thicker, defect free films.

4.4 Film morphology analysis during the pyrolysis process

Nowadays, understanding buckling and cracking formation is still a great challenge since these phenomena can only be observed once the process is completed or when the sample is quenched [62, 145, 146], which is hardly representative of what is happening during the thermal process.

Until now, not many authors have tried to identify in-situ where and when these phenomena occurs [64, 65].

In order to study and evaluate the critical zones of the film pyrolysis, the implementation of a heating stage with a small window is presented as a novel in-situ analysis technique which allows recording the film state during the pyrolysis process, undisturbing in any way such film. From now on, we will name this equipment the "pyrolyzer".

It consists of a furnace with controlled atmosphere having a silver resistance, that can heat up the film to 420°C at a maximum heating rate of 50°C/min.

The objective of this study was to identify the critical temperature zones of the pyrolysis process. Also we explored the effect that heating rate produces on the microstructure of the film.

4.4.1 Previous knowledge on thick films

Previous works from our group reported an optimized ink composition, called 4B, mainly used for spin coating deposition. In table 4.1 we recall the nomenclature for the low fluorine inks studied during the previous chapter.

Solution name	Solvent 1 (% _{V/V})	b.p. (°C)	Solvent 2 (% _{V/V})	b.p. (°C)
4B	Methanol (74)	64.7	Propionic acid (26)	141.2
4C	Propionic acid (100)	141.2	—	—
4D	Ethanol (100)	78.2	—	—
4G	Butanol (80)	117.7	Propionic acid (20)	141.2

Table 4.1: Solution nomenclature.

The used heating ramp rate for the synthesis of thin films deposited by spin coating with 4B 1.5M solution was the following:

- 5°C/min from RT to 240°C; 3°C/min from 240°C to 500°C. This thermal treatment is referred as 5/3 ramp.

To facilitate the description of the used pyrolysis conditions, from now on we will define the next table (4.2), where the ink, nominal film thickness after growth, and pyrolysis heating rate conditions are detailed.

	Solution	Additives	Nominal thickness	Heating rate ($^{\circ}\text{C}/\text{min}$)		
				160 $^{\circ}\text{C}$	240 $^{\circ}\text{C}$	500 $^{\circ}\text{C}$
1	4B 1.5M	5% TEA	250nm	5	5	3

Table 4.2: Experimental table used to describe the film and pyrolysis parameters

This was the heating ramp already used for full TFA solutions (all the precursors were metallic trifluoroacetates) [37, 147]. Due to the small thickness of the spin coated films, this thermal treatment also worked for inks with low fluorine precursors ($\text{Y}(\text{TFA})_3$, $\text{Ba}(\text{CH}_3\text{COO})_2$, $\text{Cu}(\text{CH}_3\text{COO})_2$). The effect of the heating ramp was previously studied in our group [144] for TFA, observing the heating ramp effect on the film by quenching the sample, and thus optimizing the thermal process. But as we will demonstrate, the in-situ observation of the different pyrolysis parameters evolution is mandatory to obtain trustful information and to increase the film thickness up to $1\mu\text{m}$.

4.4.2 Pyrolysis of thick films deposited with 4C ink

We studied the effect of the ramp optimized for TFA and 4B thin films on a thick film deposited with 4C solution using a tubular furnace.

	Solution	Additives	Nominal thickness	Heating rate ($^{\circ}\text{C}/\text{min}$)		
				160 $^{\circ}\text{C}$	240 $^{\circ}\text{C}$	500 $^{\circ}\text{C}$
2	4C	—	700nm	5	5	1

Table 4.3: Pyrolysis experimental conditions table n°2

Even if this thermal treatment worked for thin 4B films, for thick films deposited with 4C we observed that most of the films presented buckling and all of them were cracked. Some examples can be observed in figure 4.3.

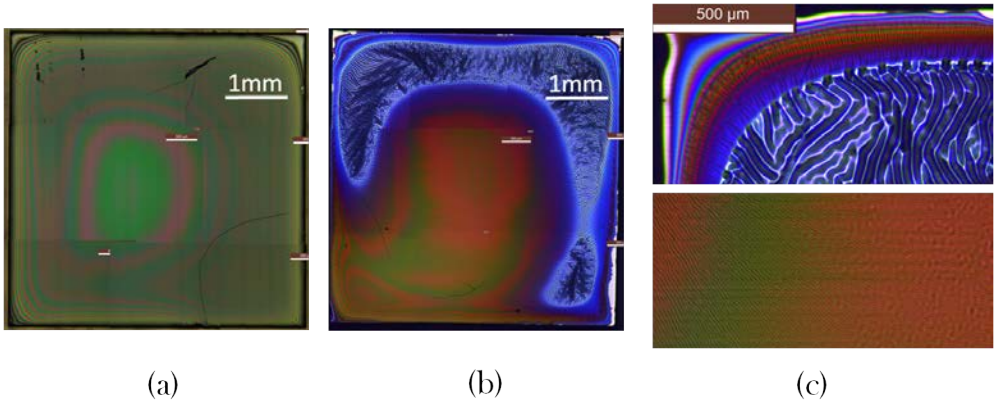


Figure 4.3: Examples of samples deposited with 4C 0.5M composition with 700nm of nominal thickness after growth (although the inhomogeneous samples have an heterogeneous thickness distribution from 500nm to 1500nm after growth). The samples were pyrolyzed using a 5/3 heating ramp. In (a) we show a film without buckling but with some cracks; in (b) a buckled film can be observed, the colour difference indicates a thickness inhomogeneity; in (c), higher magnification of the film thickest zone (blue) and thinner (green, orange) for a better buckling visualization.

The previous results obtained with the 5/3 ramp demonstrate the need to optimize the thermal process to obtain defect free films. In order to establish the proper pyrolysis parameters we used the pyrolyzer to study the film morphology evolution during the treatment.

4.4.3 Morphology study of thick films deposited with 4C ink

The analysis of a film deposited with 4C 0.5M solution, with a nominal thickness of 700nm after growth was carried out, using the 5-3 ramp.

Through several tests we observed that the film became buckled always in a temperature range between 180 and 200°C. Most surprisingly, in some of the films, the buckling was reversed recovering the original flatness.

From 250-260°C we could observe the crack formation, usually starting from an impurity or from the thickest region of the film. As temperature increased, more cracks were formed, which spread along the film. In figure 4.4 some im-

ages acquired during a pyrolysis where the buckling was partially reversed are shown. The complete video can be followed in the following link: [pyrolysis 5/3](#).

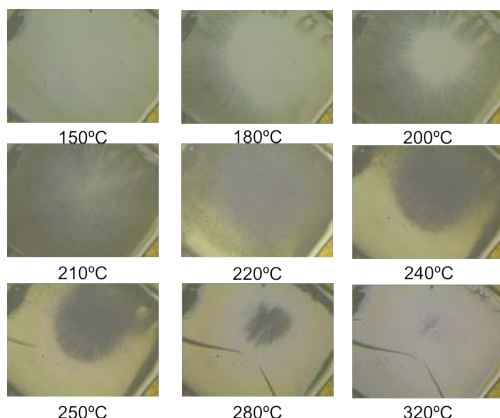


Figure 4.4: Sequence of images acquired during a pyrolysis performed in the pyrolyzer with a heating ramp 5/3. The black "stain" corresponds to the film buckling. In the image acquired at 320°C we can observe both the film cracking and a slight buckling presence (bottom-right corner of the image).

Thus, with these first analyses we were able to locate the buckling and crack formation in two very differentiated temperature ranges.

4.4.3.1 Heating ramp effect on the film morphology

To make a fast analysis of the heating ramp effect on the film we tested a slow ramp, 1°C/min, and a fast ramp at 15°C/min on a film deposited with 4C 0.5M. The film was recorded acquiring one micrograph every 4 seconds.

	Used solution	Additives	Nominal thickness	Heating rate (°C/min)		
				160°C	240°C	400°C
3	4C 0.5M	—	700nm	1	1	1
4	4C 0.5M	—	700nm	15	15	15

Table 4.4: Pyrolysis experimental conditions table n°3

During the thermal process, the films did not show buckling formation using 1°C/min heating rate. But what we can observe again is the film cracking, at 260°C, as happened using the 5-3 ramp. In figure 4.5 a sequence of the film cracking is shown, the video of the sequence can be watched in the following link: [Pyrolysis at 1°C/min](#) .

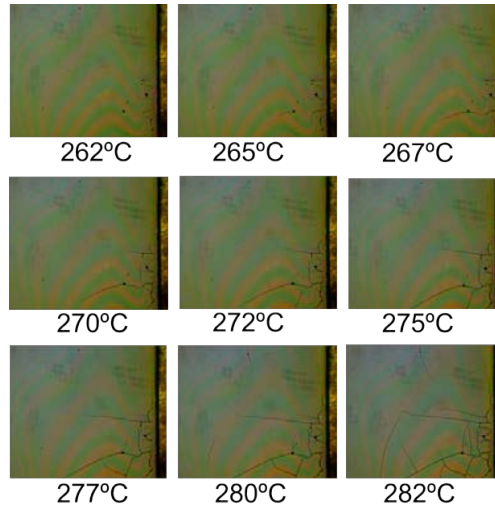


Figure 4.5: Sequence of images obtained with the pyrolyzer from 262°C to 282°C. It can be observed the crack formation during this time lapse.

The pyrolysis process using a ramp of 15°C/min produces the buckling formation around 180°C, in an irreversible way. In figure 4.6 we show the film during and after the process.

4.4.3.2 Buckling formation

Focusing on the buckling formation, we observe that the stress release phenomenon is initiated in the thickest parts of the film, spreading afterwards to the rest of the film. This is the case for the film presented in figure 4.6. Another example of irreversible buckling can be watched in the following video: *Irreversible buckling*). On the contrary, if the film thickness is homogeneous,

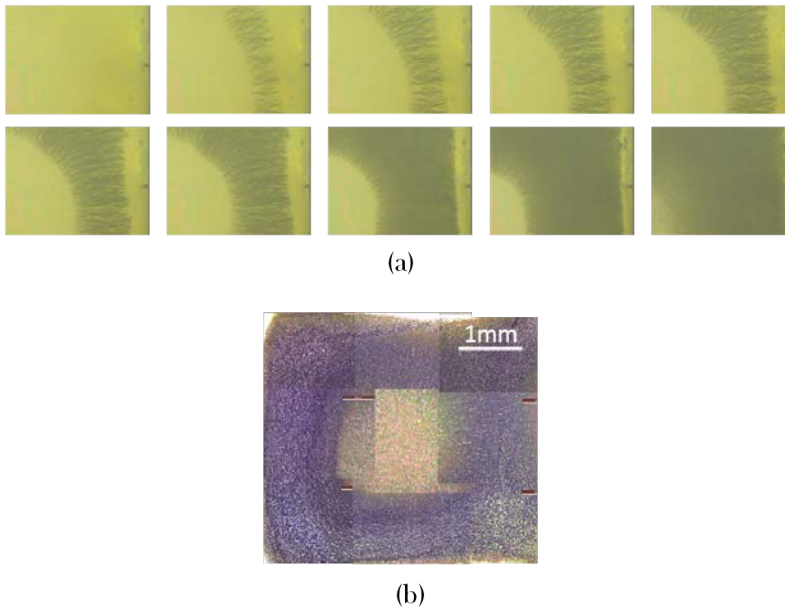


Figure 4.6: Optical micrographs of buckling produced with a heating ramp of 15K/s. (a) images acquired during pyrolysis from 178°C to 190°C (48 seconds). (b) The same film after completing the pyrolysis at 15°C/min; the darker ring indicates a larger thickness than the center (coffee stain after deposition).

the buckling is formed on the film centre at the same temperature.

We studied the surface and the cross section of a buckled film by SEM, the cross section obtained by Focused Ion Beam (FIB), SEM micrographs are displayed in figure 4.7.

What we observed was a huge film deformation: the buckling wrinkles cover all the surface, with more than $2\mu\text{m}$ thickness difference from the wrinkle crest to the thinnest part of the film.

4.4.3.3 Complete pyrolysis view from the pyrolyzer study

For the 4C composition, we studied the heating rates described in table 4.5.

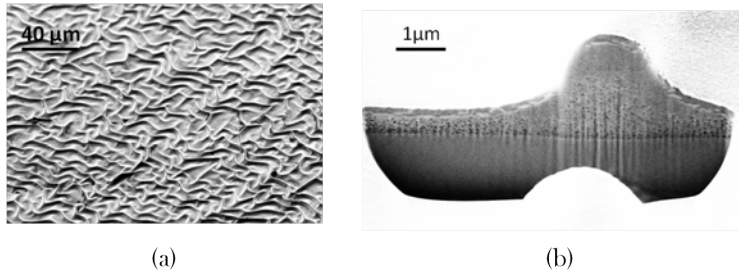


Figure 4.7: SEM images of a film buckled with a heating ramp of $15^{\circ}\text{C}/\text{min}$ deposited with 4C solution. (a) SEM micrograph of the film surface. (c) SEM micrograph of the film cross section obtained by FIB

	Solution	Additives	Nominal thickness	Heating rate ($^{\circ}\text{C}/\text{min}$)		
				160 $^{\circ}\text{C}$	240 $^{\circ}\text{C}$	500 $^{\circ}\text{C}$
5	4C 0.5M	—	700nm	25	1	1
6	4C 0.5M	—	700nm	25	1	5
7	4C 0.5M	—	700nm	25	2	2
8	4C 0.5M	—	700nm	25	5	5

Table 4.5: Pyrolysis experimental conditions table n°4

- Experiment 5 from table 4.5, presented crack formation but the film was not buckled in any moment of the pyrolysis. We did not observe any change in the film in the region from RT to 160°C even with this high heating rate.
- Experiment 6 corresponds to a pyrolysis where neither buckling nor cracks were observed in the first test. However, when this heating ramp was reproduced, some cracks appeared on the film at 260°C .
- Experiment 7 presented buckling formation at 185°C which was completely removed at 220°C . The film cracked around 260°C .
- Experiment 8 presented permanent film buckling, which was formed at 180°C .

From these experiments we could identify 3 critical temperature zones in

our system, which can be easily observed in the next video *pyrolysis zones*:

From RT to 160°C- After drying of the film, there is a first stage, up to 160°C, where the film is not affected by any applied heating rate (up to 50°C/min).

From 180°C to 220°C- We can observe buckling of the film if the heating rate is too high. Surprisingly, the surface buckling can be dragged back, recovering the film flatness if the heating rate is not too high.

For 4C composition without any additive, the buckling is formed if the heating rate is $\geq 2^\circ\text{C}/\text{min}$. It can be reversed if the heating rate does not surpass a value of $5^\circ\text{C}/\text{min}$.

From 250°C to 280°C- Cracking of the sample occurs. We did not observe a specific heating rate that avoids crack formation with a higher probability, but, surpassing a heating rate value of $5^\circ\text{C}/\text{min}$ will always lead to the film cracking. Beyond 280°C we never observed crack formation.

Crack nucleation occurs preferentially on the thickest part of the film and on impurities (i.e. precipitates). When the sample presents a clean and homogeneous image, film cracking is greatly reduced or avoided.

From this, we could conclude that crack formation is rather a product of surpassing the critical thickness for the crack propagation, than a heating ramp problem, even if this thickness is only surpassed in a part of the film. The farther we are from the critical thickness, the easier is to obtain a crack free film.

Cooling down- All the tested samples never presented any cracking during cooling down at any rate if they were completely pyrolyzed. This is not the case for the samples quenched or fast cooled below 270°C, which completely delaminated in a high percentage.

The problems from each stage are graphically represented in figure 4.8.

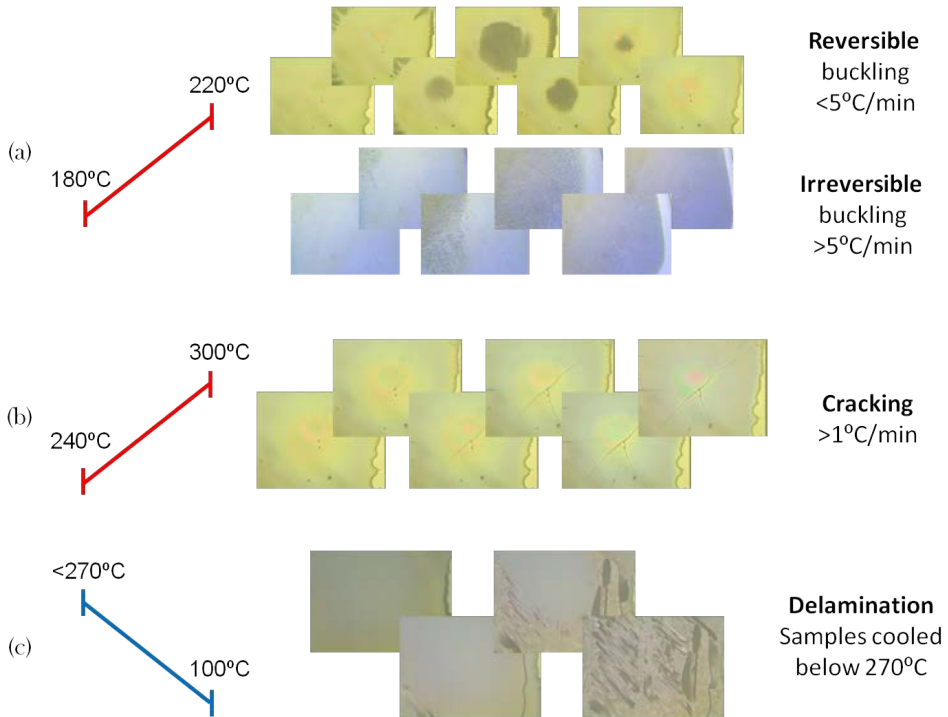


Figure 4.8: Graphical scheme of all the stages found using the pyrolyzer for films deposited with 4C 0.5M with 700nm of nominal thickness. (a) Buckling sequence formed between 180°C and 220°C for both reversible (top) and irreversible (bottom) cases. (b) Sequence of the cracking formed in the zone between 250 and 280°C (c) Sequence of film delamination when the film was cooled down from temperatures below 270°C .

4.4.4 Influence of the solution formulation on the pyrolysis

As we defined before, the ink consist of 3 main components: functional material precursor, carrier solvent and additives.

To test the heating ramp effect on other formulations we repeated the pyrolyzer study changing one of the three ingredients:

- **Fluorine free solution:** This ink is the precursor solution for the YBCO synthesis through fluorine free route. The only change respect 4C is the substitution of $\text{Y}(\text{TFA})_3$ for $\text{Y}(\text{AcO})_3$ (the propionic acid is

maintained as the only solvent).

- **4G solution:** 4G uses a 80% of butanol and 20% of propionic acid, changing the carrier solvent properties.
- **4C solution + diethanol amine (DEA):** This additive was selected due to the good performance shown during printing. As we have demonstrated in chapter 3, other additives, such as triethanol amine and polyethylene glycol, resulted in large liquid inhomogeneities during deposition.

4.4.4.1 Precursor effect on pyrolysis

We monitored a film deposited with a fluorine free (FF) 0.5M, with 700nm after growth. Fluorine free ink composition: 100%_{V/V}; Y, Ba and Cu acetates (propionates after the ligand exchange).

The temperature zones defined for 4C are maintained if fluorine free solution is used. The main difference found respect to the low fluorine is the higher film susceptibility to buckle; even at 1°C/min the film is permanently buckled as is shown in figure 4.9 (pyrolysis video: *Fluorine free buckling*). Some of the tested films presented film cracking besides the permanent buckling.

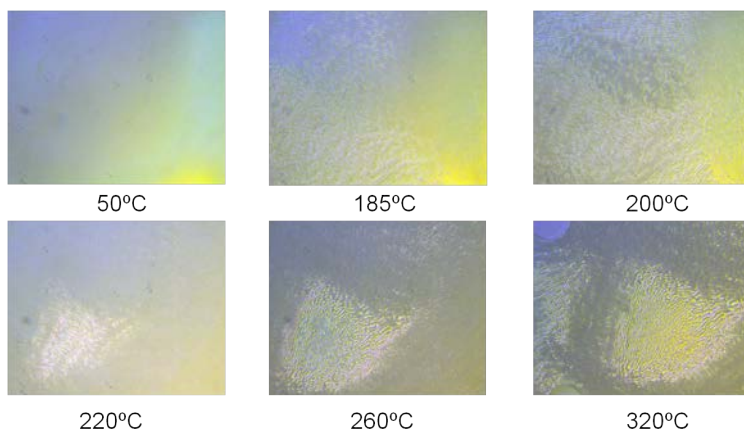


Figure 4.9: Sequence of images from 50°C to 320°C of a film deposited with fluorine free solution 0.5M using a heating ramp of 1°C/min.

From this experiment we could observe the great importance of the used precursors. The lack of the TFA precursor seems to make the film more susceptible to stress release phenomena.

4.4.4.2 Carrier solvent effect on pyrolysis

In this case we used 4G ink, which only substitutes a 80%_{V/V} of propionic acid for butanol. Again the zones are maintained, buckling is formed around 180°C and the film cracks at 260°C.

	Solution	Additives	Nominal thickness	Heating rate (°C/min)		
				160°C	240°C	500°C
9	4G 0.5M	—	700nm	25	1	5
10	4G 0.5M	—	700nm	25	5	5
11	4G 0.5M	—	700nm	25	10	5

Table 4.6: Pyrolysis experimental conditions table n°5

Like with 4C, if the heating ramp is larger than 2°C/min, the film buckles, but the difference is that this buckling is reversed if the heating ramp is less than 10°C/min, 5°C/min faster than 4C, implying a higher resistance to the compressive stress.

We did not observe an important change in the resistance to crack of the 4G respect the 4C ink. The liquid distribution during deposition is quite different, generating a "C" shaped accumulation. This indicates a large liquid movement that results on a larger thickness which tends to crack drastically. Interestingly, even if the thickest film parts are destroyed, we do not observe crack propagation.

In figure 4.10 we show the pyrolyzed films of the experiments 9 and 11 described in the experiment table 4.6.

4.4.4.3 Additive effect on pyrolysis - Diethanolamine

Chelating agents are reported to be effective in obtaining crack free films [46, 61]. Diethanolamine is a very promising additive to enhance the mechanical

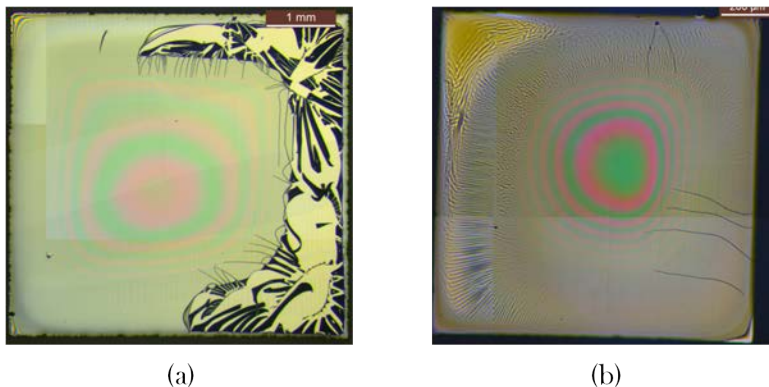


Figure 4.10: Optical micrographs of films deposited with 4G solution with a nominal thickness of 700nm after growth. In (a) the film rupture due to the "C" shaped inhomogeneity can be observed. In (b) the permanent buckling is observed at the left side of the film. The films were pyrolyzed using a 25/1/5 heating ramp for (a) and a 25/10/5 ramp for (b).

resistance to stress due to its decomposition temperature ($<500^{\circ}\text{C}$) and its chemical structure (figure 4.11):

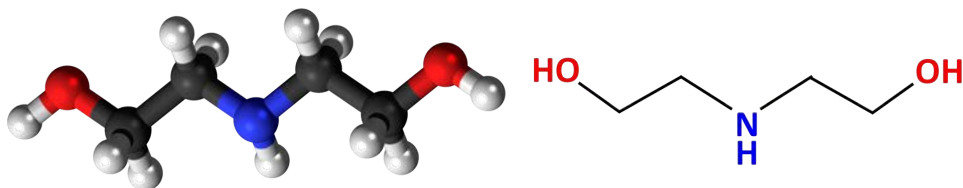


Figure 4.11: Diethanolamine molecule structural representation.

First we tested a film deposited with 4C 0.5M with 10% $_{V/V}$ of DEA, resulting in a very homogeneous deposition. In this case, with a heating rate of $20^{\circ}\text{C}/\text{min}$, we observe a slight buckling formation at 180°C , which in this case does not cover the full film and it is reversed fast.

At higher temperatures, besides the cracking, what we observe is the appearance of black circles that cover all the layer, destroying it. These circles

appear independently of the used heating rate, and they are formed at 270°C, coinciding with the DEA decomposition temperature. This phenomenon is illustrated in figure 4.12 (video: Pyrolysis 4C 0.5M + 10%DEA).

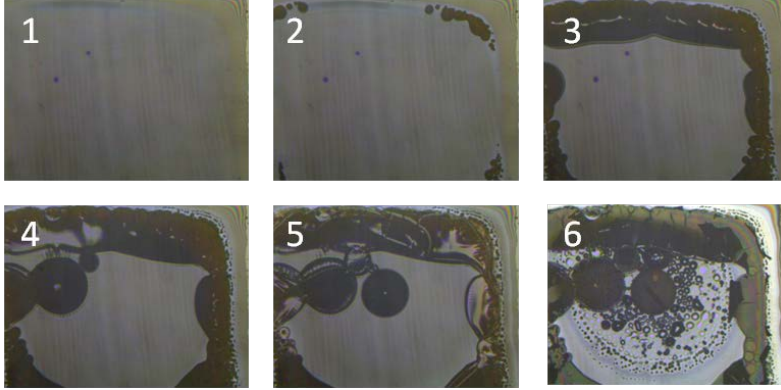


Figure 4.12: Pyrolyzer sequences from 260°C to 300°C of a sample deposited with 4C+10% V/V DEA. We present a sequence of images between 240°C and 300°C for a film pyrolyzed at 10°C/min.

The DEA amount was reduced, observing a similar effect until only a 1.5% V/V of DEA was added to the solution.

Using an addition to the 4C 0.5M solution of 0.5% V/V DEA, the deposition is not improved respect the solution without the additive but it neither presents the black circles inhomogeneities. Furthermore, the resistance to buckling is increased, presenting the stress phenomenon only at temperature ramps above 5°C/min. Buckling can be reversed if the heating rate is below 15°C/min.

Concerning the cracking zone, we can find the crack nucleation at the same temperature range than with the previous studies. But with the DEA addition, the amount of films without cracking is greatly increased. For films with a nominal thickness of 700nm after growth, by adding this 0.5% V/V of DEA we could increase the success rate of films without cracks from a 10% to a 50%, even if all the films present the same degree of liquid distribution inhomogeneity.

In equation 4.4 we calculate the DEA molar ratio respect YBCO for a DEA

addition of 0.5%_{V/V} in a 0.5M solution:

For 0.5%_{V/V}

DEA : MW = 105.14, density = 1.09g/mL.

$$1L\ 4C\ 0.5M * \frac{0.005L\ DEA}{1L\ 4C} * \frac{1000mL}{1L\ DEA} * \frac{1.09g}{1mL} * \frac{1mol}{105.14g} = 0.052mol\ DEA$$

$$For\ 1L\ solution, \frac{0.052mol\ DEA}{0.5mol\ salts} * 100 = \boxed{10.4\%_{mol\ DEA/mol\ salt}} \quad (4.4)$$

This 10.4%_{mol} of DEA addition has a great impact on the film resistance to stress, rising the success rate in achieving films without cracks, even if the homogeneity is not improved. Furthermore, the DEA addition enables heating ramps over 5°C/min without film buckling.

The same approach was used for the fluorine free solution also obtaining a great improvement on the film quality. Our results show the same increase of the buckling resistance to heating rate. A film deposited with fluorine free 0.5M + 0.5%_{V/V} DEA displayed buckling at 1°C/min. If the heating rate was kept below 5-6°C/min, buckling was reversed.

It has to be mentioned that the films with the DEA addition must be pyrolyzed up to 500°C to ensure complete organic decomposition. Using a 0.5%_{V/V} of DEA, we never observed any new crack formation after 280°C, even at heating rates as high as 15°C/min.

4.4.4.4 Additive effect on pyrolysis - Nanocomposite precursor salts

In order to increase the YBCO performance, we can synthesize nanocomposite films spontaneously segregating nanoparticles from organometallic precursors in the YBCO crystallization phase.

For the spontaneous segregation nanocomposite route, Ta(EtO)₅ and Zr acetylacetonate (Zr(acac)₄) were used for Ba₂YTaO₆ (BYTO) and BaZrO₃

(BZO) nanoparticles synthesis respectively. The precursor amount depends on the NPs %_{mol} (respect YBCO) that we want to use, but usually is around 6%_{mol}.

By adding these precursors, we found that the number of non cracked samples was greatly increased respect the "raw" solution. The buckling appears at a rate of 2°C/min and can be reversed below 5-6°C/min, the same values presented by the 4C ink without additives.

To prove if the cause for the improvement was the metal ligand, a 12% of Cu(acetylacetonate)₂ was substituted for the Cu(AcO)₂, thus contributing with the same amount of acetylacetonates provided by the BZO precursor. We did not observe any improvement respect the 4C without additives, so the could not confirm the assumption that acetylacetonate alone was enhancing the stress resistance, although the success of this approach has been recently demonstrated by KIT [148].

4.4.5 Summary of the morphology analysis

Summarizing, with the analysis carried out with the pyrolyzer, we were able to define and predict the thermal regions and the heating rates leading to different stress release mechanisms and thus defects formation. For the low fluorine system we can state the following:

- The buckling and cracking occur at two differentiated temperature regions. In addition we observed that the two phenomena are independent from each other.
- Buckling can be completely avoided using slow heating rates between 180°C and 220°C. Even if the buckling appears, it can be reversed if the heating rate is not too high depending on the ink formulation.
- Cooling after the complete pyrolysis does not affect the sample morphology. but if the sample is quenched below 270°C, the film will delaminate with a high probability, completely destroying the film (as we showed in figure 4.8).

- Thickness inhomogeneity must be completely avoided to obtain samples without cracks.

We observed the same buckling formation temperature range for the different tested compositions, but the heating rate values for the defect formation differ depending on the ink. We define as critical buckling heating rate 1 (R_{B1}) to the ramp where buckling is formed and critical buckling heating rate 2 (R_{B2}) to the heating ramp where the buckling is not reversed.

The buckling formation indicates that in this region we are dealing with a compression stress regime [78, 139, 140], thus the compositions that are less prone to buckle either have a higher resistance to the compressive stress or suffer less compression during this thermal zone.

The critical heating ramp depends on the ink formulation. The susceptibility to buckle depending on the used ink is indicated in table 4.7.

Solution composition	R_{B1} ($^{\circ}\text{C}/\text{min}$)	R_{B2} ($^{\circ}\text{C}/\text{min}$)
Fluorine free (FF)	<1	1
FF + 0.5% _{V/V} DEA	1	5
4C	2	5
4C + 0.5% _{V/V} DEA	5	10
4G	2	10

Table 4.7: Critical buckling rates comparative among the different tested ink compositions. R_{B1} is related to the critical heating rate for buckling formation. R_{B2} refers to the critical heating rate where buckling deformation is permanent

The crack formation is always located at higher temperatures than buckling, between 250 $^{\circ}\text{C}$ and 280 $^{\circ}\text{C}$ for all the tested compositions. The sample cracking strongly depends on the film homogeneity and its mechanical resistance, but still, surpassing a heating rate of 5 $^{\circ}\text{C}/\text{min}$ results in the sample cracking.

If the thermal treatment requires reaching higher temperatures than 320 $^{\circ}\text{C}$ (i.e. if DEA is added), the sample can be heated at any rate without cracking.

All the tested samples never presented crack formation at any cooling rate if they were already completely pyrolyzed. This is not the case for the samples

quenched or fast cooled below 270°C (before completing pyrolysis in a certain degree), which resulted in film delamination with a high probability.

We defined 160°C to 240°C as the zone transition temperatures where we can perform a heating rate change, if needed. From now on, the heating ramp nomenclature will be the next one: rate1/rate2/rate3, being the slash 160°C for the first and 240°C for the second.

The thermal treatment was optimized for low fluorine solutions according to the critical zones, leading to the heating ramp 25/1/5 (°C/min) for the 4C solution. According to the nomenclature this means: 25°C/min up to 160°C for the evaporation step, 1°C/min to 240°C to avoid the buckling and 5°C/min to the pyrolysis end.

For the step from 240°C to the end, there is no effect associated to slowing down the heating rate, but going at higher rates than 5°C/min leads to an increased probability to obtain cracked samples.

Once studied the film response during the pyrolysis treatment, a deeper study must be carried out to understand what is causing the different phenomena observed. Overall, this allowed us to optimize the heating ramp. But some questions remain unanswered:

- We have observed the buckling and cracking formation in very specific temperature ranges. What is the cause, from a physicochemical point of view, that triggers the apparition of these phenomena in that specific temperature ranges?
- The buckling formation is related with the release of compressive stress; cracking appears with the release of tensile stress. How is this stress generated?
- How is it possible that, once the film buckling is produced, the film can recover the initial flatness?

To fully understand the pyrolysis process and to optimize the thermal treatment and film composition, we focused our studies on what we consider that has the greater impact on the film deformation due to stress: The mass loss or

organic decomposition, the thickness reduction and the mechanical properties during the process.

For this purpose, thermal analysis was carried out to evaluate the mass evolution. Thickness was studied using a novel technique based on coupling the pyrolyzer and an interferometer to perform an in situ measurement of thickness evolution during pyrolysis. The film mechanical properties were studied by nanoindentation and by a novel in-situ thermomechanical analysis apparatus developed for this purpose.

4.5 Mass and heat flow evolution study during the pyrolysis

The main cause for the stress generation during pyrolysis lies on the film compaction due to the organic mass decomposition [149]. For this reason we need to study the mass evolution along the process.

We will divide this section in the different techniques used to determine the mass and heat evolution during the pyrolysis process: Thermogravimetric analysis (TGA) for the organic mass loss; Differential Scanning Calorimetry (DSC) to observe the heat flow during the pyrolysis to determine the decomposition peaks; Evolved Gas Analysis (EGA) and Infrared spectroscopy (IR) to study the decomposed mass nature.

In each section we will study the thermal properties for 4C, 4C+ 0.5%_{V/V}DEA and 4G ink formulations. The used conditions on the different thermal analyses are detailed in table 4.8.

4.5.1 In situ mass evolution analysis

By thermogravimetric analysis, we can study the sample weight change with temperature. This analysis was the first to be performed on low fluorine films to observe the mass loss stages.

Factors to consider:

Technique	Heating ramp	Temperature range	Atmosphere
TGA	20°C/min	50-800°C	Humid O ₂
DSC	5°C/min	50-500°C	Humid O ₂
EGA	5°C/min	25-700°C	Humid O ₂ , vacuum
IR	5°C/min	25-320°C	Humid O ₂

Table 4.8: Standard table used to define the experimental conditions of the analyses performed on mass and heat during the pyrolysis process.

- The films are deposited by drop coating, so the deposition homogeneity may differ from the inkjet printing deposited films.
- If the film is too thick and inhomogeneous, the final mass will not match with the expected value due to the delamination of the film (extra mass loss), also observed in the pyrolysis of films deposited by inkjet printing.
- The films after deposition may absorb water, which is not released until certain temperature that can vary depending on the solution composition and the ambient atmosphere. If the water mass is not properly considered, it can lead to errors on the weighted mass.

The first experiment was a TGA for the 4C solution with the conditions described in table 4.9:

Technique	Heating ramp	Temperature range	Atmosphere
TGA	20°C/min	50-800°C	Humid O ₂

Table 4.9: Thermal analysis experimental conditions table n°2

The theoretical final mass was calculated in order to discriminate the mass decomposed from the film precursors from other possible elements like solvent evaporation and absorbed water. For any solution with the low fluorine precursor salts (Y(TFA)₃, Ba(AcO)₂, Cu(AcO)₂) result was a final mass of 45.27%

respect the initial mass (43.52% if a 0.5%_{V/V} DEA was added). The calculations can be found in the annex.

If we have a look on the TGA spectra (figure 4.13) we observe a loss of mass from 150°C until 320°C. From 320°C no further mass is lost. We shall recall that the mass lost before 150°C corresponds only to the solvent and absorbed water evaporation.

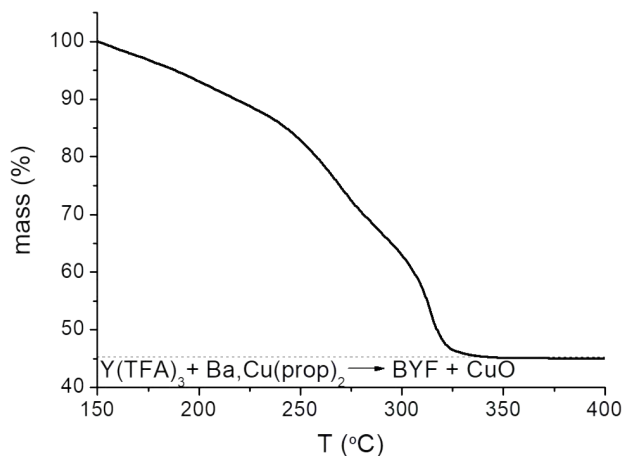


Figure 4.13: TGA curve of a 4C solution in humid O₂ atmosphere. Analysis performed at 20°C/min.

4.5.1.1 Ink composition effect on organic mass loss

To compare the ink composition effect on the decomposition, we repeated the TGA with the same conditions for 4C+ 0.5%_{V/V} DEA and 4G. The different TGA curves are displayed in figure 4.14.

By comparing the different formulations, what we can observe from the TGA curves, is a different degree of decomposition below 275°C depending on the tested ink, but above this temperature all the ink compositions have a sim-

ilar decomposition degree.

The 4C+DEA curve is almost identical to the 4C one, with the difference that when DEA is added, the mass is fully decomposed at 500°C. From the mass evolution measurement we cannot conclude the reason for the higher buckling and cracking resistance of this composition.

On the other hand, 4G (80% butanol, 20% propionic acid) presents a larger decomposition at lower temperatures than the 4C family of inks.

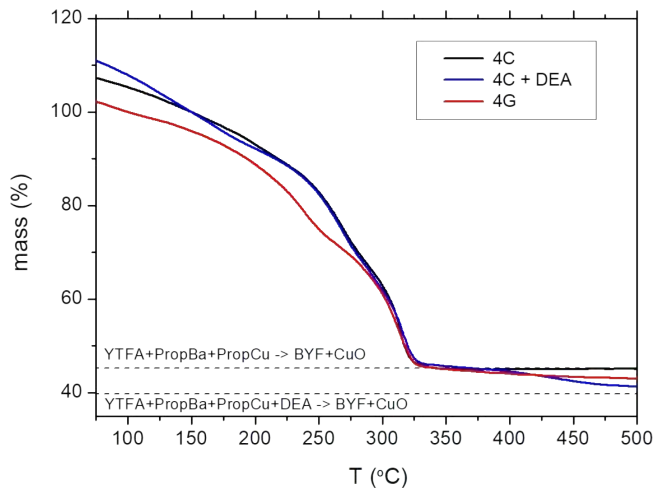


Figure 4.14: TGA performed to all the low fluorine solutions. The analyses were performed in humid O_2 at $20^\circ C/min$.

With the TGA we could determine how the mass is lost depending on the ink formulation. For the 4C compositions it seems that the mass loss rate is higher in the temperature range where cracks are produced. Still more analysis are required to comprehend the different stages observed during the pyrolysis process.

4.5.1.2 Film composition after the pyrolysis process

As we mentioned before, the pyrolysis products must be the BYF matrix and copper (I,II) oxide. To check if the pyrolysis of thick films deposited with 4C and 4G formulations was leading to the correct products, we performed an X-Ray diffraction analysis on the pyrolyzed samples (see figure 4.15).

The structure analysis was performed in a 2 dimensional GADDS (2D) X-ray diffraction (XRD), with a θ - 2θ analysis. We measured by X-ray two films deposited by 4C ink, one pyrolyzed at 320°C and the other at 500°C.

For both samples we detected the necessary precursors for YBCO growth, BYF ($\text{Ba}_{1-x}\text{Y}_x\text{F}_2$) + CuO according to equation 4.3.

From the X-ray spectra (4.15) we could observe sharper spectrum peaks for the sample pyrolyzed at 500°C, indicating a higher crystallinity, but both samples presented the required film composition at the end of the pyrolysis process.

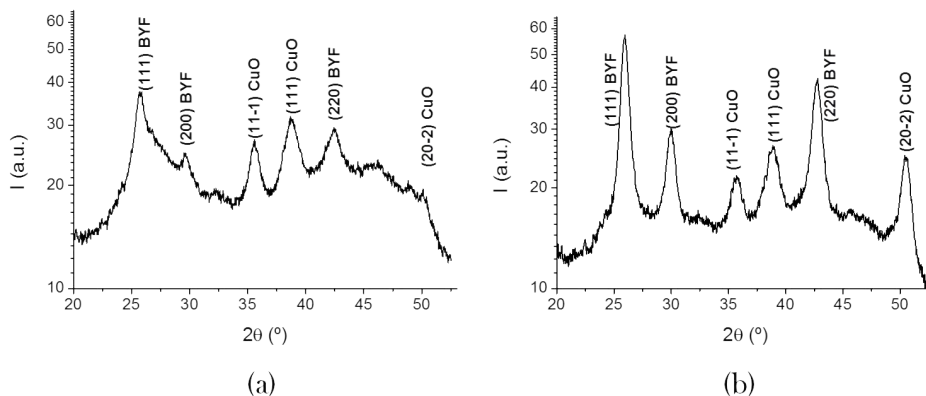


Figure 4.15: (2D) X-ray integrated diffraction pattern for a sample pyrolyzed at (a) 320°C and (b) 500°C. The higher crystallinity degree can be observed on the film pyrolyzed at 500°C from the sharper peaks. Both films presented the required precursors for the YBCO growth (CuO, BYF).

The X-ray analysis for 4C+DEA and 4G, showed identical results.

4.5.2 Heat flow analysis

With DSC we analyzed the heat flow during the process. In this analysis, the sample and a reference with a well known calorific capacity are heated at a constant heating rate. When the sample is suffering a transformation (e.g. a phase change), the heat will flow to or from the sample in order to keep sample temperature at the same rate than the reference. In our system, negative DSC signals are translated as heat transferred to the sample due to an endothermic process (positive signals for exothermic transformations).

Simultaneously to the DSC analysis, a TGA was performed. By the thermogravimetry derivative ($dTG = \frac{\partial mass}{\partial T}$) as function of $dTG(m, t)$, we can obtain information about the mass decomposition rate. Both analysis are displayed together for a better inspection of the decomposition peaks.

Simultaneous dTG - DSC (Figure 4.16) was performed as detailed in table 4.10:

Technique	Heating ramp	Temperature range	Atmosphere
DSC	5°C/min	50-500°C	Humid/Dry O ₂

Table 4.10: Thermal analysis experimental conditions table n°2

From the DSC curve performed on a 4C solution, we observe two decomposition stages, the first one starting at 210°C with a maximum intensity at 250°C and a second, sharper peak, at 275°C with a maximum at 300°C. The positive values indicate that the two processes are exothermic.

The exothermic peak indicates that the processes are indeed a decomposition (instead solvent evaporation, for example).

From the dTG curves we observe that the first stage is less intense than de second one, indicating a lower organic mass decomposition rate for the first peak.

This analysis shows the same results for all the ink formulations, with small variations on the peak temperature, complementing the data obtained by TGA.

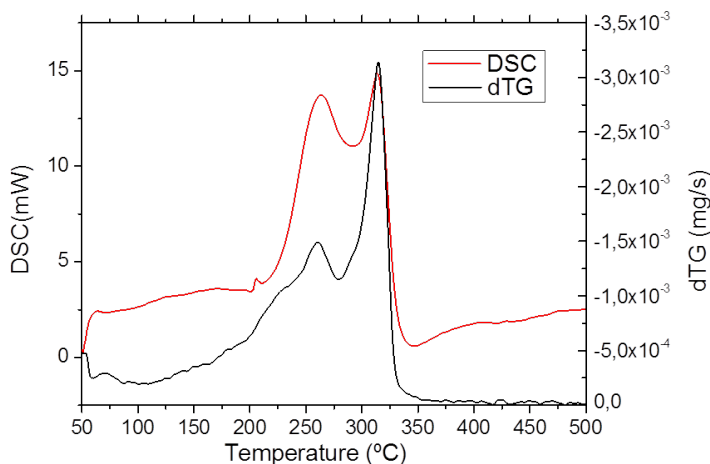


Figure 4.16: Simultaneous DSC (left Y axis) and dTG (right axis) for a 4C solution at 5°C/min using a humid O₂ atmosphere.

4.5.3 Released gas compositional study

With the already presented techniques we can study the global changes in mass and heat with temperature. However, for a specific interpretation of atomic/inorganic vapors and standard gases like H₂, H₂O, CO₂, etc. we will use Evolved Gas Analysis (EGA).

Using EGA, the released gases can be analysed by different analytical methods, such as gas chromatography, Fourier transform spectroscopy or, as it is the case for this specific work, mass spectrometry.

The objective of this analysis is to know the (thermal) region where a specific precursor or additive is decomposed.

The conditions used for all the performed EGA are detailed below:

The EGA analysis for the 4C solution without additives (figure 4.17) shows the next results:

1. Water evaporation is observed until 150°C, as we already mentioned from TGA curves. Water release is observed during the main decomposition peaks, indicating water absorption during the process.

Technique	Heating ramp	Temperature range	Atmosphere
EGA	5°C/min	25-700°C	Humid O ₂ , vacuum

Table 4.11: Thermal analysis experimental conditions table n°4

- From 200°C a first decomposition peak appears with a maximum at 230°C, matching with the first peak detected by simultaneous DSC-dTG (exothermic). The predominant detected masses with a molecular weight of 28 and 29, associated to a propionic acid fragment (CH₃CH₂⁺). The propionate fragment besides the low signal detected for mass 44 (CO₂) indicates that at this temperature range only propionate molecules are being decomposed.
- From 260°C, a second decomposition peak is detected, with a kind of overlapped double peak shape: a first broad one with a maximum at 285°C and a second sharp peak at 315°C; we consider this peak as a single decomposition step. For this peak, we detect the release of propionate fragments and a strong CO₂ presence. This indicates that in this decomposition stage, both propionates and TFA molecules are being decomposed.
- Only a small signal of mass 31 (CF) is detected at 320°C. This implies that F is not released from the film at this stage.

4.5.3.1 Ink composition effect on the released gases

We repeated the EGA experiments with the same conditions for the other ink compositions. The main observations from these analysis are detailed below.

In figure 4.18 the mass 28 (propionates and CO) signal acquired from EGA is plotted to compare 4C and 4C + 0.5%_{V/V} DEA. In this figure the changes on the main decomposition temperatures depending on the ink 4C additive can be observed.

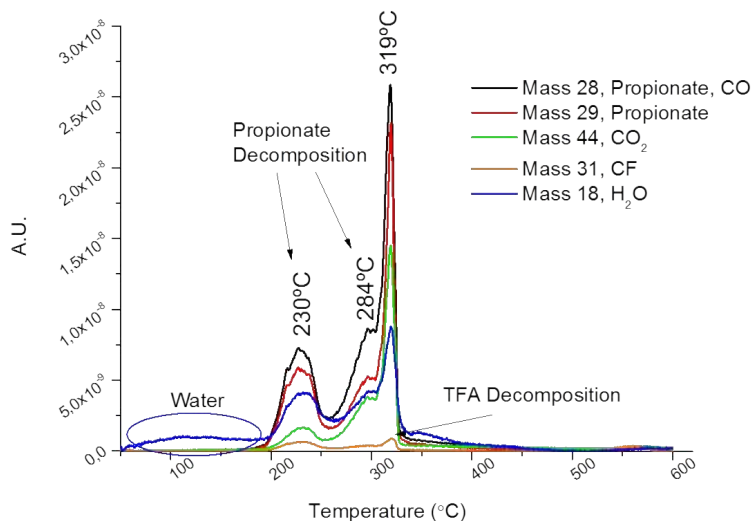


Figure 4.17: EGA with mass detector performed to a 4C solution in humid O₂ atmosphere at 5°C/min. The displayed masses correspond to CO₂ and propionates.

When DEA is added in a 0.5%_{V/V}, the EGA shows that the first decomposition peak is displaced to lower temperatures: the peak maximum when DEA is added is located at 200°C while the 4C without DEA presents a maximum at 220°C. But as can be observed from the figure 4.18, the decomposition peak ends at the same temperature than the 4C without additives. The most reasonable explanation is that the DEA can be binded to the metals displacing the propionates, which will decompose at lower temperatures. We did not observe any real relevance to this temperature shifting, since the higher buckling resistance of the films deposited with 4C + 0.5%_{V/V} DEA is attributed to a mechanical factor as we will see in section 4.6.

This decomposition shift to lower temperatures was not detected in TGA, since 4C and 4C + 0.5%_{V/V} DEA presented almost identical curves.

The second decomposition peak for 4C + DEA remains at the same position than the 4C ink without additives.

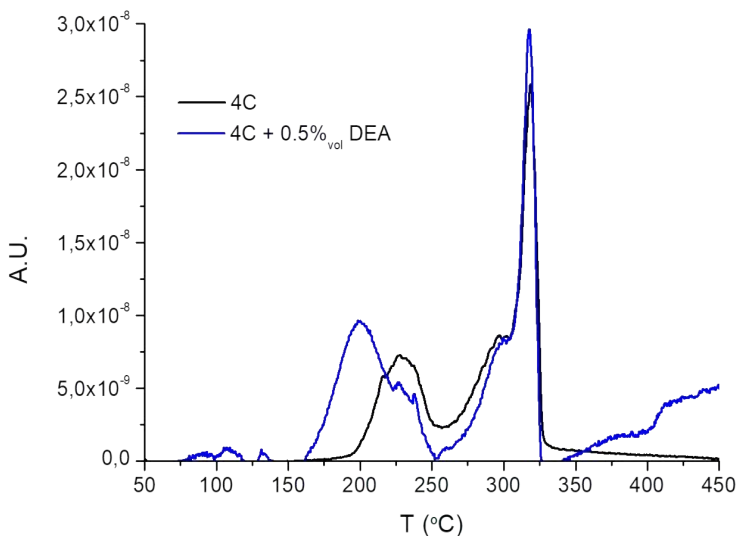


Figure 4.18: EGA analysis with mass detection performed to 4C and 4C + 0.5%_{V/V}DEA. The curve correspond to mass weight of 28, associated with propionate and CO. The analysis was performed at 5°C/min in humid O₂ atmosphere.

Despite the addition of 0.5%_{V/V} DEA (10%_{mol}), it seems that the results on the mass analysis do not present relevant differences respect the 4C formulation without additives.

The EGA performed on 4G (figure 4.19) shows an important difference respect 4C ink: beside the propionates observed for 4C analyses, we also detect the presence of acetates.

A possible reason might be an incomplete ligand exchange due to the lower amount of propionic acid used as solvent compared to 4C. The acetate presence in the EGA analysis justifies the faster decomposition observed in TGA since acetates decompose around 150°C according to the analysis.

Again, we do not find the CO₂ mass (44) until high temperatures (275°C-325°C range), indicating that before this temperature only whole molecules of propionate, and acetate in the case of 4G composition, are being decomposed.

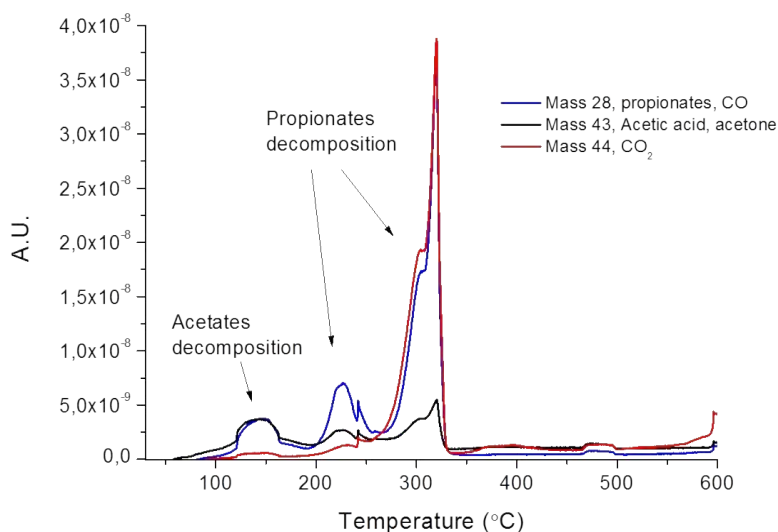


Figure 4.19: EGA with mass detector performed to a 4G solution in humid O₂ atmosphere at 5°C/min. The displayed masses correspond to CO₂ and propionates.

From the analyses on heat transfer and on the released gases, we were able to define the mass evolution during the pyrolysis stage in two zones around 200°C-250°C and 260°C-320°C. These zones match with the ones observed with the pyrolyzer study on morphology (considering that the EGA experiments were performed in vacuum, which can shift the decomposition temperatures).

From EGA analysis we could propose that during the first stage only propionates are decomposed while during the second decomposition stage both propionates and trifluoroacetates decompose.

As we will see latter on, this is of great importance to understand the pyrolysis process.

4.5.4 Infrared spectroscopy analysis of the pyrolysis process

Infrared spectroscopy was used for a more specific analysis of the precursor species.

Although EGA gives a sensitive response of the mass decomposed, the mass spectrometer only detects ionized fragments from the released gases (CH_3CH_2 , CO_2 , etc.).

For this reason it is hard to discriminate which specie is being decomposed since, propionate, acetate and trifluoroacetate can present the same fragments, or fragments with the same mass-to-charge ratio (m/z), like CH_3C and CO .

Using Fourier Transform Infrared Spectroscopy (FT-IR) we analysed the different precursor species evolution of the sample.

In figure 4.20 we show an IR spectra of a 4C film heated at 145°C for 20 minutes. We compare the 4C spectra with an IR of $\text{Y}(\text{TFA})_3$ and $\text{Na}(\text{propionate})$, which we used as reference.

The Beer-Lambert law establish a linear relationship between the absorbance and the concentration of an absorbing specie.

To determine the TFA amount we can measure the fluoromethyl (sp^3 C-F str.) absorbance, which for trifluoroacetate presents two intense absorbance bands between $1100\text{-}1200\text{cm}^{-1}$ [98].

For the propionates determination, we used the alkane peaks (sp^3 C-H str.), which presents a band between $2800\text{-}3050\text{cm}^{-1}$ [98].

In order to quantify an analyte by FT-IR, we require a calibration curve and a clear and isolated signal for each compound. Unfortunately the IR spectrum presents an overlapping on the alkane zone ($2800\text{-}3050\text{cm}^{-1}$) by the broad OH peak that can be observed with a maximum at 3400cm^{-1} . This overlapping complicates an accurate quantification. For this reason, we will study semi-quantitatively the evolution of the organic species during the pyrolysis process.

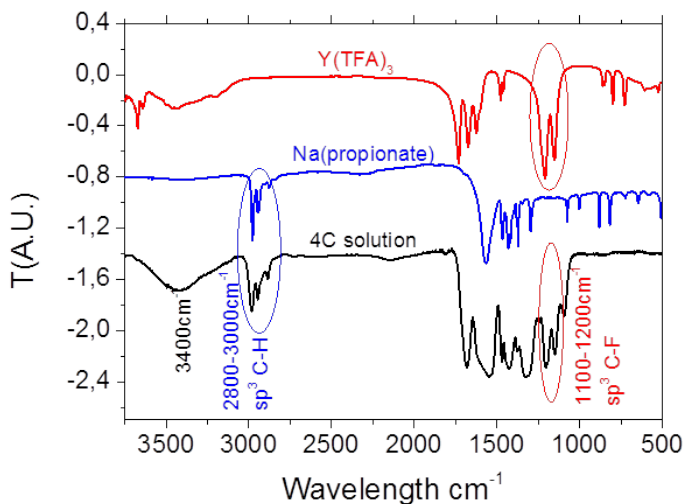


Figure 4.20: IR spectra for a sample after drying at 145°C for 45 minutes (black). In blue and red, the spectra of sodium propionate and yttrium trifluoroacetate respectively is shown. The absorbance band of the alkane group (C-H str.) used for the propionate determination is encircled in blue. Inside the red circle we find the bands corresponding to fluoromethyl (C-F str.) absorbance, assigned to trifluoroacetate molecule.

Before analysing the samples, we had to ensure if the LAO substrate could affect the IR signal. For this reason, several substrates were measured.

As it can be observed in figure 4.21, The analysis of the LAO substrates confirmed an identical absorption for wavelengths above 1100cm⁻¹. Below this wavelength, the substrate signal could interfere with the sample signal, since could differ among substrates.

The procedure for the IR analysis of the 4C and the 4C + 0.5%_{V/V} DEA inks, consisted on quenching the sample at the temperature that we want to analyse.

The used thermal treatment was the 25/1/5 optimized for the 4C solution, holding the temperature at 145°C for 45 minutes to ensure the complete solvent

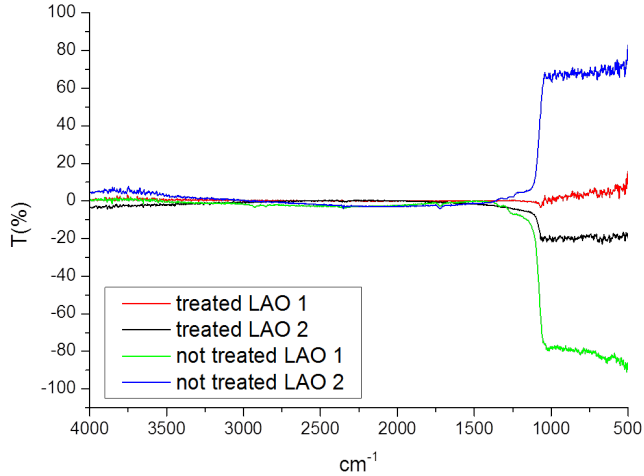


Figure 4.21: IR spectra for 4 LAO substrates. Two substrates (red and black) were thermally treated at 900°C . Two substrates ((blue, green) were not submitted to any treatment. A thermally treated LAO substrate was used as blank.

removal. The sample delamination when quenching the sample became an important problem, forcing to repeat most of the samples.

For the IR measure, the chamber was purged for 3 minutes with N_2 in order to guarantee homogeneous conditions during the measure.

The analysed samples were quenched at 145°C , 200°C , 240°C , 270°C , 300°C and 400°C for both 4C and $4\text{C} + 0.5\%_{V/V}$ DEA. The spectra resulting from the IR measurement are displayed in figure 4.22.

What we can observe from the figure 4.22 is that, from 150°C , the peak associated to the propionates (2900cm^{-1}) starts to decrease, with a large signal reduction from 200°C to 240°C . After that, the peaks decrease progressively until 300°C , where it is completely extinguished.

Focusing now on the peaks between $1100\text{-}1200\text{cm}^{-1}$, we observe that the peak area remains constant until 300°C , and then the absorption band is re-

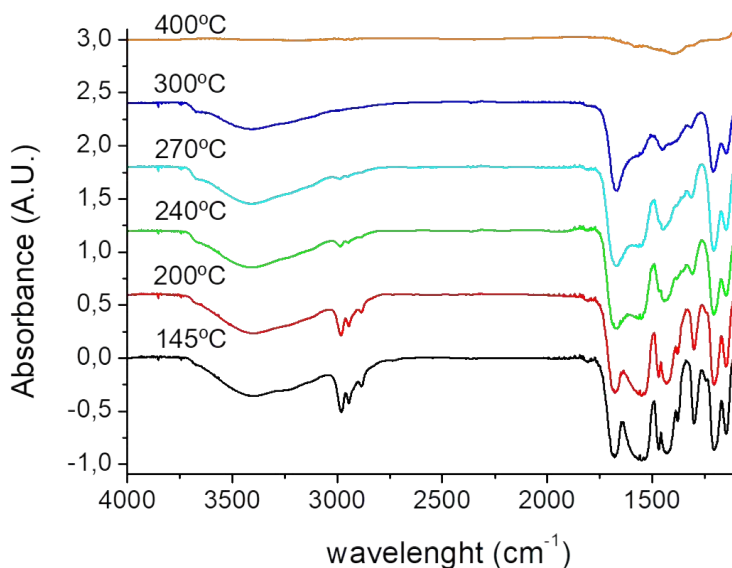


Figure 4.22: IR signal evolution with temperature for a 4C + 0.5%V/V composition, using a 25/1/5 heating ramp.

duced until it is extinguished.

To a more specific analysis on the decomposition during the pyrolysis process, we calculated the relative mass of the organic ligands remaining on the film at each temperature.

For the calculation, we integrated the IR spectrum between 1100-1200 cm^{-1} to measure the trifluoroacetate's absorption band area and between 2800-3050 cm^{-1} for the propionate's one. The values were normalized, considering that at 145°C we have the 100% of the organic ligands. In figure 4.23, the obtained values are shown as function of temperature.

To demonstrate the compatibility of the used techniques, in the figure 4.23 the values obtained from the IR bands integration are compared with the curve obtained from EGA measurement on mass 28 (propionates, CO). From this

comparison we can clearly observe that the sharp peak detected at 320°C correspond to the TFA decomposition.

From the calculation of the relative mass corresponding to each chemical specie (equation 4.5), it can also be observed that a 70% of the propionates are decomposed in the first decomposition peak (before 250°C). This fact has a great relevance, since the 68.2% of the total organic mass correspond to propionate molecules. This implies that a 50% of the total organic mass is decomposed in the first stage, between 180°C and 250°C, where buckling appears.

$$\begin{aligned}
 & \text{Yttrium organic mass : } CF_3COO^- * 3 \\
 & \text{total mass} = (12 * 2 + 19 * 3 + 16 * 2) = 339 \\
 \\
 & \text{Barium + copper organic mass : } CH_3CH_2COO^- * 5 \\
 & \text{total mass} = (12 * 3 + 5 + 16 * 2) * 5 = 730 \\
 & \hspace{20em} (4.5) \\
 \\
 & \text{Propionates percentage} = \frac{730}{730 + 339} * 100 = 68.2\% \\
 \\
 & \text{Trifluoroacetate percentage} = \frac{339}{730 + 339} * 100 = 31.8\%
 \end{aligned}$$

With the IR analysis, we complemented the data obtained from thermal analysis regarding the mass evolution during the pyrolysis process.

From the complete study we observe two main decomposition peaks, one around 220°C and the second at 300°C (values that can change depending on the ink composition). Even though, the loss of mass begins at 150°C with the propionates as the only specie being decomposed according to the IR analysis.

On the other hand, the TFA decomposition does not begin until 280°C, in the second decomposition peak. At 280°C, around a 50% of the total organic mass has been already decomposed (all of it due to propionate decomposition).

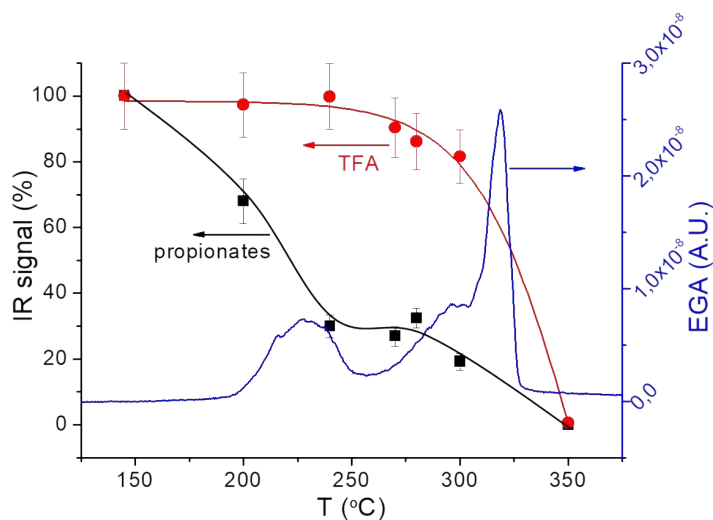


Figure 4.23: Comparison of the data obtained from IR spectroscopy and EGA during the pyrolysis of a film deposited with 4C 0.5M + 0.5%_{V/V} DEA. The blue curve corresponds to the EGA data, mass 28 (propionates, CO), while the dots, with their guidelines, are the values obtained from the integration of IR bands, black for the integration between 2800-3050 cm^{-1} (propionates) and red for the bands between 1100-1200 cm^{-1} (TFA).

The implications of these deductions will be fully discussed after the thickness evolution in-situ study since the thickness reaction to the mass decomposition is required to understand how and where the stress is generated.

4.5.5 Summary of mass and heat evolution study results

Along this section we have deeply analysed the organic decomposition during the pyrolysis process, knowing how the mass evolve and which specific compounds were decomposed at each temperature. Comparing the study on the mass with the morphology evolution, 2 stages were identified around the same temperature ranges.

The results obtained from the 4C mass and heat evolution during pyrolysis perfectly match with the 2 decomposition stages detected by different used

analytical techniques as we show in table 4.12.

Technique	200°C-240°C	280°C-320°C
DSC-dTG	broad exothermic peak	intense, sharp exothermic peak
EGA	broad propionate/CO decomposition	sharp propionate/CO/CO ₂ decomposition
FT-IR	propionate largest decomposition	TFA decomposition

Table 4.12: summary of the results obtained for the different analyses on the mass evolution for all the ink formulations. Two separated temperature ranges (200-240°C; 280-320°C) were perfectly defined from the mass study.

Around 200°C, the first decomposition peak matches with the buckling formation. Although at this point we cannot relate both phenomena since we defined buckling as compressive, later on we will show the relevance of this first decomposition stage on the buckling formation.

It is at the second decomposition stage (around 280°C), with the fast decomposition of both propionates and trifluoroacetates, where the film cracking occurs. As we will show in the next section (thickness evolution during pyrolysis), is in this temperature region where the film collapses, generating the stress responsible of the crack formation.

The same analyses for the 4C solution when a 0.5%_{V/V} si added to a 0.5M solution do not show important differences on the mass decomposition. This is interesting since the DEA was added in order to increase the mechanical resistance of the film to buckling and cracking, and thus we have to avoid the stress generation due to a large mass addition.

The reason for the little weight variation on the mass decomposition observed by TGA is the small molecular weight of the DEA molecule compared to the organometallic precursors:

- $MW_{DEA} = 105.1 \text{ g/mol}$
- $MW_{Y(TFA)_3} = 428.0 \text{ g/mol}$
- $MW_{Ba(prop)_2} = 283.5 \text{ g/mol}$
- $MW_{Cu(prop)_2} = 209.7 \text{ g/mol}$

Still the molar ratio of the DEA respect to the sum of precursor salts is a 10.4%, a high enough ratio to justify the mechanical resistance enhancement observed during the morphology study.

4.6 In situ study on the thickness evolution during pyrolysis

Even if the mass decomposition is the main cause of the film shrinkage, the volume reduction might not be linear with the mass loss. Actually, the thickness comparison with the mass reduction provide information about the stress produced in the film (i.e. compressive, tensile).

For functional oxides film synthesis by Chemical Solution Deposition, any reported method for the thickness detection during the thermal process can be found in the literature, even considering the importance of this parameter to control the firing process.

In this thesis, we present a novel technique for the CSD in-situ thickness measure during pyrolysis.

The analytical tool used for the thickness determination was interferometry. This family of techniques uses the interference of two superimposed waves in order to obtain the optical parameters and the thickness of the measured sample. With this technique we were able to characterize the thickness and homogeneity after pyrolysis in a fast, non-destructive testing, as we will show later on this chapter.

The condition to measure the film thickness by interferometry is that the light can be transmitted and reflected through the film. The reflected light will generate an interference pattern as the one we show in figure 4.24. In

order to fit this pattern, refractive index n , and extinction coefficient k must be defined. The information of how to obtain these parameters as well as the measure mechanism are detailed in chapter 2, section 2.5.5.

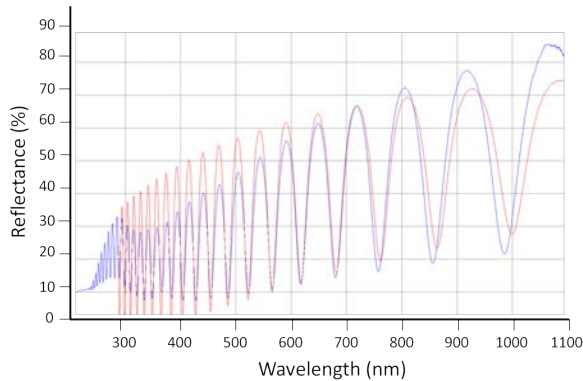


Figure 4.24: Example of an interference pattern (blue line) of a 4C film with 750nm of nominal thickness after growth measured after pyrolysis. The red line corresponds to the mathematical pattern fitting. The thickness value calculated from this interference pattern is 1565nm

The interferometer became a useful analytical tool to characterize the film thickness and thickness homogeneity. But it was by the coupling of the pyrolyzer with the interferometer that we were able to measure the thickness evolution during pyrolysis.

By measuring a sample with and without the pyrolyzer cover, we obtained the same thickness values, confirming that the pyrolyzer window does not interfere with the thickness measurement.

To check if the optical parameters used for the pyrolyzed film were valid for previous decomposition stages (after drying and at intermediate temperatures), we compared the thickness measurements obtained by the interferometer (without changing the n and k values) with the ones obtained by profilometry. There was little deviation among the values obtained from each technique, thus we concluded that the optical parameters n and k are very similar during the pyrolysis process.

In the next sections we will describe the results obtained from coupling

the interferometer with the pyrolyzer, for the in-situ analysis of the thickness evolution during pyrolysis. We will also present the thickness changes when the system is brought to an isotherm state and we will determine the density changes of the film during pyrolysis.

4.6.1 Thickness evolution during pyrolysis

The main objective of these analyses was to observe the thickness evolution of a film during pyrolysis step. The system setup is presented in figure 4.25. For the experiment we simply program the desired thermal ramp and we measure the thickness.

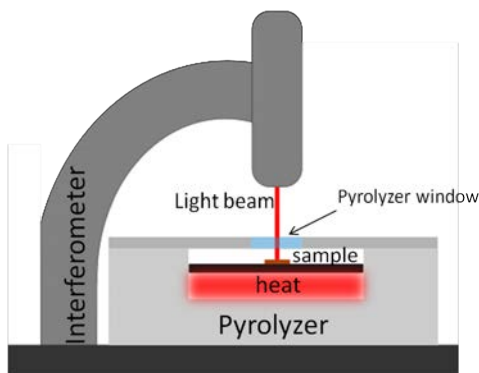


Figure 4.25: Schematic representation of the interferometer and pyrolyzer coupling.

There are two important factors to consider for taking measurements using this technique:

1. The signal acquisition zone (spot with a diameter of 0.7-1mm) must be homogeneous in thickness.
2. The thickness of a film becomes impossible to measure when buckling appears, so the limitation of this study relies on the formation of this phenomenon.

To observe the effect on thickness of the DEA addition, the thickness evolution was tested using a heating ramp of 25°C/min to 160°C, 1°C/min to 240°C,

5°C/min to 400°C (25/1/5) in order to avoid buckling formation.

	Solution	Additives	Nominal thickness	Heating rate (°C/min)		
				160°C	240°C	400°C
12	4C	—	700nm	25	1	5
13	4C	0.5% _{V/V} DEA	700nm	25	1	5

Table 4.13: Pyrolysis experimental conditions table n°6

Using the pyrolysis parameters described in table 4.13, we observed that the addition of DEA does not change the thickness evolution respect the 4C solution without the additive.

As we said, the thickness of a film becomes impossible to measure when it buckles, so the limitation of this study relies on the formation of this phenomenon. The heating ramp that can support a 4C solution without additives is 2°C/min (table 4.7). For this reason, 4C + 0.5% DEA which can stand 5°C/min without buckling formation has been used to compare the evolution of thickness and mass.

To compare the thickness evolution with the studies on the mass change during the thermal process, we performed an interferometry+pyrolyzer analysis following the next thermal profile: 25°C/min up to 145°C with 45 min of isotherm to evaporate all the solvent; the rest of the process at 5°C/min. The used experimental conditions are described in table 4.14:

	Solution	Additives	Nominal thickness	Heating rate (°C/min)		
				160°C	240°C	400°C
14	4C	0.5% _{V/V} DEA	600nm	25	5	5

Table 4.14: Pyrolysis experimental conditions table n°7

From the resulting curve (figure 4.26), we can observe two main phases: From 145°C (after drying) to 200°C the thickness does not decrease. From 200°C the thickness starts to decay linearly until 320°C, were all the organic mass has been decomposed.

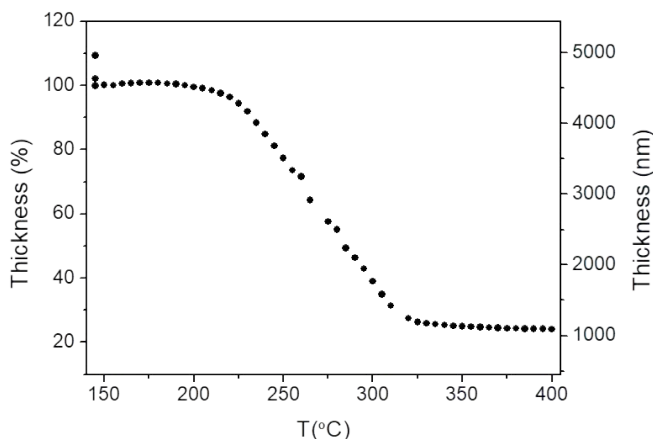


Figure 4.26: Curve of thickness evolution with temperature for a $4C+0.5\%_{V/V}$ DEA with a nominal thickness of 600nm after growth. The used thermal profile was 25/5/5. The left Y axis corresponds to the relative thickness; the right Y axis to the real measured thickness value.

From the study we want to remark the huge thickness reduction observed during the analysis. Almost an 80% of the thickness after drying is reduced. From this value it can be observed the great challenge that is trying to obtain thick films by CSD.

From the thickness curve we can see again the presence of two zones during the pyrolysis as we described. But the result highly contrasts with the mass evolution observed for the different low fluorine ink formulations, where the mass decomposition starts at 150°C while thickness remains constant until 220°C.

To determine the relation between all the studied parameters, we will compare the thickness and mass evolution during the pyrolysis process.

4.6.2 Film density evolution during pyrolysis

In the previous section we showed how the propionates were decomposing from 150°C, with a mass loss of 50% of the total when 240°C were reached. On the other hand, thickness remains almost constant in this temperature range. This will generate density changes on the film that provides interesting results for the pyrolysis study.

The mass from TGA was divided by the film volume measured from interferometry (thickness * 5x5mm³) obtaining the film density variation with temperature. The curve can be observed in figure 4.27.

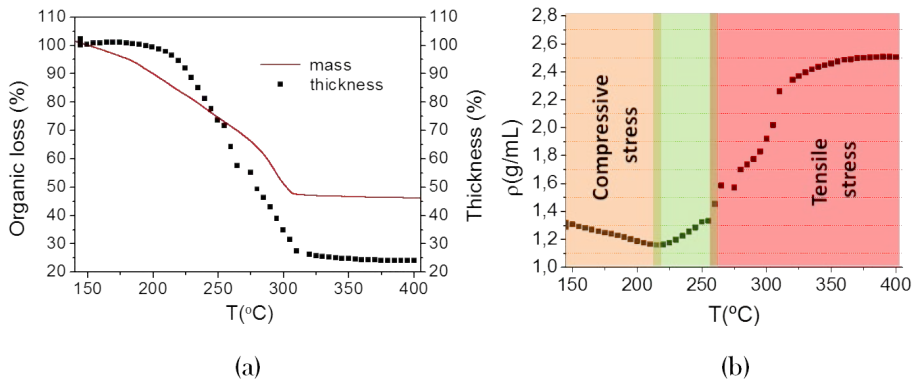


Figure 4.27: (a) Comparison among mass and thickness evolution during pyrolysis measured by TGA and interferometry respectively; (b) density changes with temperature. Density was calculated by dividing the mass obtained from the TGA measurements with the film volume measured by interferometry. In orange we highlighted the compressive stressed region where buckling is formed; in green the buckling release zone; in red the tensile stressed region where film cracks.

From the density curve we can define again 2 zones. Until 220°C, we can observe a slight drop on the film density, product of the mass decomposition for a film that is not losing practically any thickness. After this temperature, the thickness decreases faster than the mass, resulting in a density increase.

From the results observed until now, we will try to define the stress modes

that the film is experiencing.

Looking at the thermal region from 150°C to 225°C, we observe the next:

1. The film buckles at the beginning of this range and "de-buckles" at the end.
2. The mass is reduced a 25% from the total. All of it due to propionate decomposition.
3. The film thickness is constant.

As we defined before, the film buckles when a compressive stress is applied to the film. This phenomenon is typically reported on films deposited on compliant substrates [139].

In our case, the film compression is generated due to the loss of mass without any volume reduction. This implies that the film structure is preventing the film shrinkage. The film tending to shrink is in this case the compressive acting force.

On the second region, from 240°C to 320°C, we observe the next:

1. The film cracks.
2. The remaining propionates and all the TFA is decomposed.
3. The film is compacted an 80% respect the film thickness after drying.

For this region the huge film thickness reduction (75% of the initial thickness) originates the tensile stress responsible of the film cracking. This stress is generated by a limited transverse diffusion (due to the substrate influence) while in the cross section there is a shrinkage of several microns.

In figure 4.28 we display a scheme to represent the substrate in-plane stress acting on the film.

Around 220 film switches from a densification decrease to an increase on density. It is at this temperature that we observe the buckling recovering, since the compression causing the stress release phenomenon changes to the a tensile stress, which has an opposite force direction.

With this new information we can understand the critical stages on the

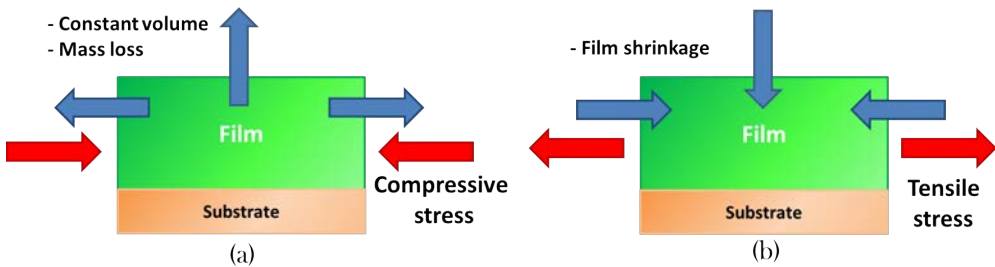


Figure 4.28: Representation of the stress acting on the film in the direction parallel to the substrate. (a) Represents the case where the film volume is constant while the mass decreases; the blue arrows represent the force that the film structure makes to prevent the film volume loss due to the mass lost; the red arrows are the compressive stress produced from the density loss that results on the film buckling. (b) Represents the tensile stress (red arrows) produced from the film shrinkage (blue arrows), which is hindered in the substrate in-plane direction, causing the film cracking.

pyrolysis process.

The buckling and cracking formation is submitted to stress generation produced by the volume reduction, which, in turn, is caused by the organic mass decomposition. For this reason, it is normal to observe the same critical thermal regions on the studies of morphology, mass and thickness evolution during pyrolysis.

We observed that the thickness decreases only in the second decomposition peak, where TFA decomposes. From this fact, we can deduce that these two phenomena are closely associated.

From a chemical point of view, the fluorine atom from TFA can easily be bonded on the metal coordination sphere, forming a network that acts as a "skeleton" that keeps the film from shrinking. When the TFA decompose, the structure collapses, which is observed in the thickness huge reduction, generating the tensile stress that causes the film cracking.

This information is specially relevant for the ink design. Adding flexible compounds able to keep the film structure, can smooth the film collapsing if they decompose in differentiated thermal regions.

One example of an additive able to smooth the film collapsing will be presented in chapter 5.

To conclude the study on the thickness evolution, in the next section we will show the thickness changes when the system is brought to an isotherm.

4.6.3 Thickness evolution in isotherm regime

From the last experiments we observed that thickness below 240°C remains almost constant even if at this temperature, half of the organic mass has been already decomposed. In order to study in detail the different zones of the thermal profile, we measured the thickness while holding a constant temperature at the thermal regions of interest.

The objectives of this analysis were to determine the shrinkage at each temperature, and to test if the film could be compacted at lower temperatures in order to avoid crack formation.

For this experiment, we performed several isotherm annealings for 1 hour at 190°C, 210°C, 240°C and 260°C. We choose these temperatures following this criteria:

- 190°C - Temperature where the thickness remains constant and buckling is formed.
- 210°C - Zone where thickness starts to decrease, matching with the buckling reversal.
- 240°C - From this temperature, thickness decreases linearly. At this temperature did not observe buckling or cracking formation, and if the R_{B2} is not surpassed, at 240°C the buckling is totally reversed.
- 260°C - Crack formation temperature.

We used 4C+0.5% v/v DEA ink formulation, performing the study under oxygen atmosphere.

The experiment led to quite interesting results, all of them represented in figure 4.29. The isotherm performed at 190°C presents a slight thickness loss

(around a 10% after 1 hour), indicating that the film volume is stable, even if propionates are being decomposed.

The isotherm performed at 210°C also shows a small thickness reduction, a 20% after 1 hour. In this case we , so the shrinkage rate becomes slower over time.

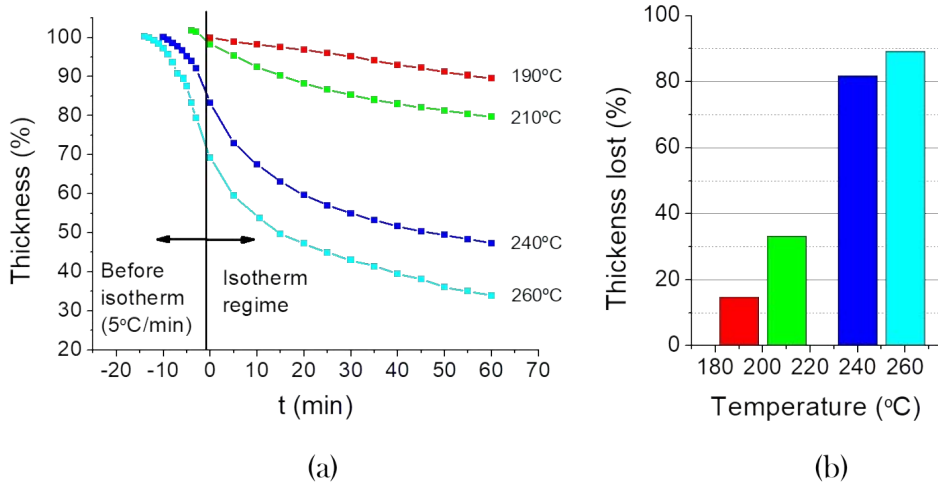


Figure 4.29: (a) Thickness evolution over time during an isotherm at 190°C, 210°C, 240°C and 260°C. In the negative time values we represented the thickness decreased before reaching the isotherm, where the samples were heated at 5°C/min. (b) Relative thickness reduced during each isotherm from the total film shrinkage observed at the pyrolysis end, a 75-80% of the film thickness after drying.

In contrast with the small thickness reduction at lower temperatures, during the isotherm at 240°C the film shrinkage becomes really important, around a 55% of thickness is shrunk in an hour. The thickness decrease follows an exponential decay; the greater part of thickness is lost in the first 15 minutes of the isotherm.

We performed a longer isotherm at 240°C (2 hours). From the result we observed that during the first hour, a 55% of the film thickness was lost while

in the second hour only a 7% of the film is compacted. This indicates that the film cannot be fully compacted before the temperature where we observe the second decomposition peak in the mass analyses.

At 260°C the film shrinks even faster, losing a 66% of thickness in 1 hour.

From these results, we can deduce that there is a thermodynamic activation that triggers the thickness collapsing located around 240°C. We observe this from the slight film compaction observed below this temperature.

Actually, to achieve the full film shrinkage, the film must reach the second temperature peak; at 240°C the film will not be fully compacted.

The thermodynamic factor can be explained using what we learned from the mass study.

From the IR analysis we observed that while propionates decompose at low temperatures, the trifluoroacetates decompose at the final stages of the process, in the second decomposition peak observed by EGA, TGA and DSC.

Below the TFA decomposition temperature, film structure is held by this ligand, keeping the film from collapse. The thickness study on the isotherm regime confirms this hypothesis already proposed on the thickness and mass comparison study; the TFA ligands act as the film skeleton, and when it decomposes, the film collapses.

The addition of compounds supporting the film structure, as it is the diethanolamine, smooth the film sudden collapsing due to the TFA decomposition.

Schmidt *et al.* and lately Kozuka *et al.* [45, 46] demonstrated that chelating ligands such as acetylacetonate ($\text{CH}_3\text{COCH}_2\text{COCH}_3$), ligand of the BZO precursor salt presented in section 4.4.4.4, increased the critical thickness to obtain crack free films. A reason for this improvement can be found on the explanation that we provided in this section.

An additive to improve the film resistance to crack requires the next characteristics:

1. It has to contain functional groups that allow the to generate bounds with

the metals, creating a network to support the film structure.

2. In order to keep the structure, the additive must decompose at a temperature above the film collapse, in order to smooth the compaction.
3. Preferentially, the additives must have a low molecular weight to avoid a mass contribution too high that will result in an extra stress generation.

To complete the physicochemical analysis of the pyrolysis process, during the next section we will present the study of the film mechanical properties during pyrolysis.

4.7 Film mechanical properties

Along this chapter we have demonstrated the consequence of the decomposition process on the film thickness and mass. But still the higher resistance to crack of some composition respect the others is not justified. In this section the mechanical properties of the system will be analysed and discussed by means of two techniques: Nanoindentation and a novel in situ measure using thermomechanical analysis.

4.7.1 Film mechanical testing by nanoindentation

To test the mechanical properties of small samples, nanoindentation is perhaps the most commonly used technique [150]. It allows a fast and accurate measure of the hardness and elasticity of a sample. Furthermore, the small indented depth (10% of the total thickness) guarantees that the substrate will not interfere with the measure.

We found that some ink composition could produce films more resistant to stress generated defects. To determine the mechanic characteristics of films deposited with different inks, we performed nanoindentation studies.

For the sample preparation we used the same method than for the IR study, consisting of quenching the sample at the desired temperature. The films were pyrolyzed in the heating stage (pyrolyzer), using the thermal profile optimized

for the 4C solution, 25/1/5. Again we had the same difficulty in obtaining films without delamination that we faced for the IR studies.

The tested ink composition were 4C and 4C+0.5% V/V DEA ink formulations, all of them with a 0.5M concentration.

In 4.30 we show the typical load-displacement curve obtained from nanoindentation. The figure comes from Oliver and Pharr work presented in 1992 [151].

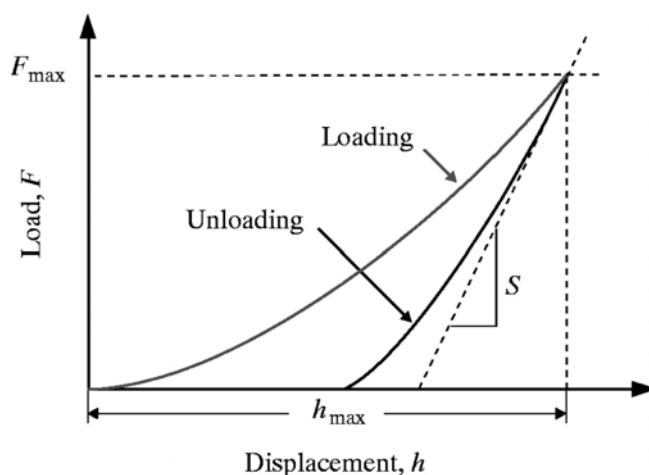


Figure 4.30: A schematic representation of load versus indenter displacement data for an indentation experiment. The quantities shown are F_{max} : indentation load; h_{max} : the indenter displacement at peak load; h_f : the final depth of the contact impression after unloading; and S : the initial unloading stiffness.

To obtain a nanoindentation curve, the nanoindenter tip is pressed on the sample. The load placed on the indenter tip is increased as the tip penetrates further into the specimen until it reaches a user-defined value, usually a 10% of the total film thickness.

When the load is retired, the sample will recover part of the displacement depending on the material elasticity. The more elastic is the sample, the larger the displacement recovered during the unloading.

The curve slope upon unloading gives the measure of the sample stiffness (S), which can be used to calculate the reduced Young's Modulus (E_r), related

with the sample elasticity.

Hardness (Hr) is calculated from the relation of the maximum load (F_{max}) with the projected area of the indentation calculated in function of the nanoindenter tip.

Firstly we nanoindented the films deposited with 4C ink. The films were quenched at 145°C, 220°C, 270°C and 320°C.

The curves obtained from these experiments are displayed in figure 4.31.

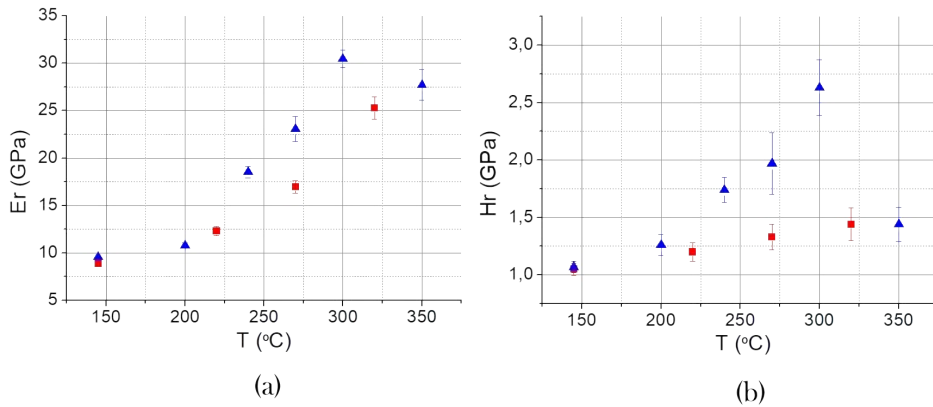


Figure 4.31: (a) Reduced Young's modulus and (b) Hardness value for a 4C solution (red) and 0.5%V/V DEA (blue) additives.

From the measures we observed a clear tendency. The sample measured at 145°C presented a values of Hr= 1.05GPa and a Er=8.87GPa. For films quenched at higher temperatures, both Hr and Er were increased progressively, with the maximum values for the films at 320°C (H=1.44GPa, Er=25.28GPa).

The 4C + 0.5%V/V DEA ink presented major differences respect the 4C ink without additives. For this composition the films were quenched at 145°C, 200°C, 240°C, 270°C and 350°C.

The film at 145°C had the same values on hardness and Young's modulus than the previous inks, and the same can be said for the film mechanical

properties after pyrolysis (350°C).

But the films measured at intermediate temperature present larger values on H and Er, specially at the higher pyrolysis temperatures, indicating that the film deposited with this compositions are stiffer and harder during pyrolysis.

From the nanoindentation measurements we could demonstrate the DEA effect on the film mechanical properties. This additive causes an increase of the film hardness and stiffness during the pyrolysis process, justifying the higher resistance to crack of the films deposited with 4C+DEA.

Still, the mechanical properties were measured out of the real pyrolysis conditions. A proof of this is the sample delamination during the quench at intermediate pyrolysis temperatures, indicating that the film properties before and after the quench are quite different.

For this reason, in the next section we will present the film mechanical properties in-situ measured during the pyrolysis process.

4.7.2 In situ mechanical properties study during pyrolysis

In order to observe the mechanical properties without the need to quench the sample, our collaborators from the Universitat de Girona (UdG) developed a novel technique based on nanoindentation.

The thermomechanical analysis (TMA) is a technique used in thermal analysis to measure properties like mass, volume and density as they change with temperature.

The instrument is based on a cannula that can apply a controlled load, and it is sensitive to displacement. Thus the measurements follow the same procedure than in nanoindentation, but measuring the sample during the pyrolysis process. The technical aspects of the measurement are described in section 2.5.6.2.

We used this technique to measure the mechanical properties of our films during the pyrolysis process.

In figure 4.32 the curve load used as example on the experimental methodologies, is recalled. In this figure, the displacement for a dried sample is dis-

played. It can be seen how the cannula is displaced when a load is applied and how part of the displacement is recovered when the load is 0, indicating an elastic recovery also observed in the nanoindenter.

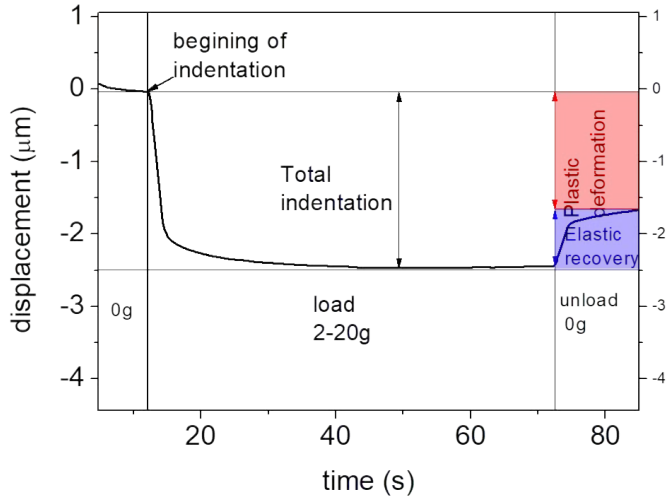


Figure 4.32: Example of a displacement curve obtained from a TMA test.

For the initial test, the 4C ink was used. Since the TMA apparatus is not at the same facility than the inkjet printer, the films were deposited by drop coating, aiming for a nominal thickness of $1\mu\text{m}$ in a $10\times 10\text{mm}^2$ substrate.

The film was measured at 100°C , 140°C , 170°C , 200°C , 230°C , 260°C and 310°C .

We did not apply the same loads for all the temperatures. We observed that the samples at 100°C and 320°C were more difficult to indent, for these temperatures we used a load of 20g. For the rest of measured temperatures we applied 2g of load.

We used a heating ramp of $10^\circ\text{C}/\text{min}$ for all the tests. The sample indentation lasts 1 minute; this implies that between the beginning of the analysis and the end, there is a temperature displacement of 10°C .

In figure 4.33 we show the measurements obtained from this experiment.

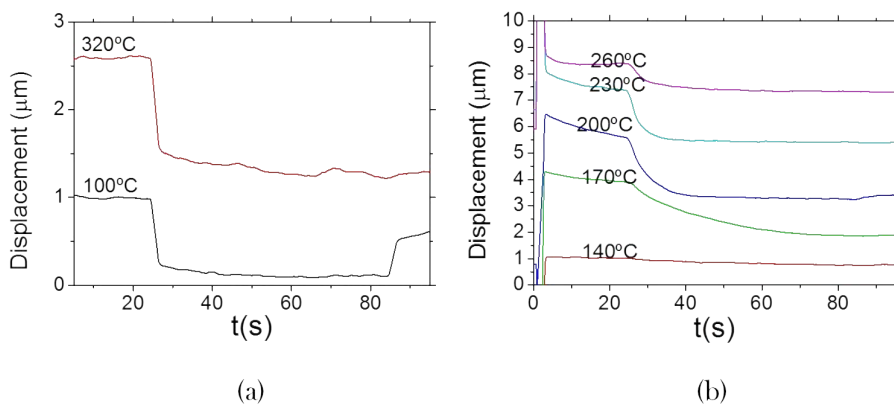


Figure 4.33: Displacement curves obtained for the TMA measure of films deposited by drop casting of 4C 0.5M solution with a nominal thickness of $1\mu\text{m}$ after growth. The applied loads were (a) 20g for 100°C and 320°C and (b) 2g for 140°C, 170°C, 200°C, 230°C and 260°C.

First we will describe the samples measured at 100°C and 320°C (figure 4.33(a)).

The sample measured at 100°C presents an important elastic recovery when the cannula is unloaded.

The film measured at 320°C broke because the load applied in the large cannula indentation area, so it does not present any displacement recovery.

Other samples measured at this temperature did not break. Instead, they recovered all the displacement during the unload, indicating that they were not deformed by the test.

The interesting results came with the measurements at intermediate pyrolysis temperatures, during the thermal decomposition.

Once the load is constant, no further displacement should be observed. Instead we observe displacement until it reaches the substrate.

This is the expected behaviour for a liquid regime, with a viscosity propor-

tional to the relaxation time at constant load [101]. We defined this type of deformation as viscous deformation.

We repeated the measurements on the films deposited using 4C +0.5%_{V/V} DEA and 4G ink formulations, this time deposited by inkjet printing.

The measured temperatures were: 100°C, 140°C, 170°C, 200°C, 230°C, 260°C, 290°C and 310°C.

For the measure at 140°C, the applied load was increased from 2g to 20g. The reason was the small displacement observed during the previous experiments (figure 4.33(b)).

4.7.2.1 In-situ mechanical study for 4C 0.5M + 0.5%_{V/V} DEA

The mechanical analysis of the 4C+DEA ink formulation shows (figure 4.34) the same dynamics already presented in the previous test (figure 4.33).

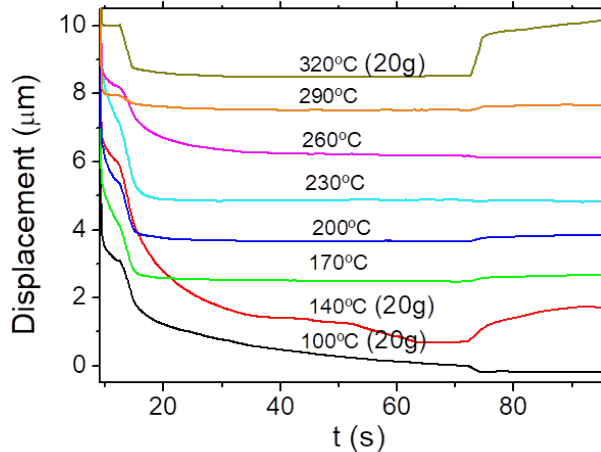


Figure 4.34: Displacement curves over time obtained from the TMA of 4C 0.5M + 0.5%_{V/V} DEA. The applied load was 2g except for the measures at 100°C, 140°C and 320°C.

Still, some differences were found:

1. The measure at 100°C presented viscous deformation while the film deposited by drop casting presented an elastic solid behaviour.
2. The measure at 320°C did not break the sample. What we observe is a complete recovery of the displacement during the unload. This indicates that the measure did not deform the sample.
3. The measurements show a smaller viscosity at intermediate temperatures (fastest relaxation time).

We attribute the differences to the film homogeneity difference obtained from drop coating and inkjet printing deposition, being the second technique the most reliable.

From these measurements we can observe that the film at 320°C is indeed stiffer (resistance to be deformed) than the sample at 100°C as we observed by nanoindentation.

To observe the relevance of the viscosity values, we repeated the analysis for the 4G 0.5 ink formulation.

4.7.2.2 In-situ mechanical study for 4G 0.5M

The TMA for the 4G solution (figure 4.35) showed an important difference on the measurement of the film at 100°C. We could observe both viscous deformation and a great elastic recovery (viscoelastic regime).

The rest of the measurements show a similar behaviour than the results for the 4C+DEA formulation.

4.7.2.3 Film viscosity analysis

For a quantitative viscosity measurement we used the method described in the annex A.2. It consist of the fitting of a curve obtained from the equation 4.6:

$$\nu = \frac{F}{6\pi\eta R^2} \frac{(2H - h_0)^2 h_0}{4(H - h_0)^2} \quad (4.6)$$

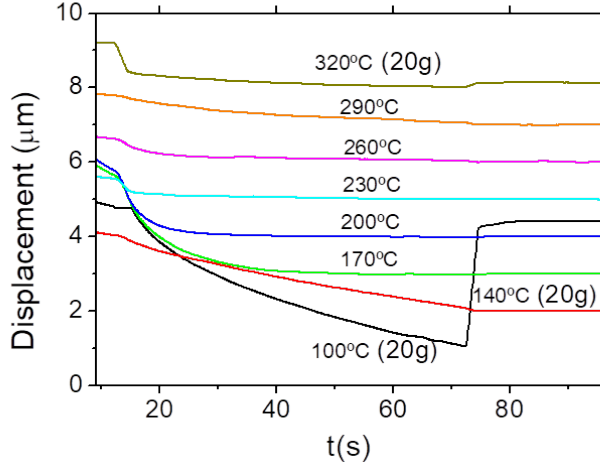


Figure 4.35: Displacement curves over time obtained from the TMA of 4G 0.5M. The applied load was 2g except for the measures at 100°C, 140°C and 320°C.

where F is the applied load; η , viscosity; H , the film thickness; h_0 , the probe-substrate distance and R the radius of the hemispherical probe.

From this equation, a parameter α is obtained, which is a measure of the relaxation time of the probe. α is related with viscosity as follows:

$$\alpha = \left(\frac{6\pi\eta R^2}{F} \right) \quad (4.7)$$

When the curve obtained from the TMA measurement is properly fitted with the theoretical curve obtained from the integration of eq. 4.6 (since the probe velocity is dh/dt , h displacement, t time), α can be obtained, and from there, the viscosity. In figure 4.36 we show an example for the viscosity determination. For a proper fitting, the cannula must remain stable (constant displacement) before the end of the loading stage.

Only the curves with a finite relaxation time could be measured. This implies that only the curves from the measurements at 140°C, 170°C, 200°C, 230°C and 260°C could be measured.

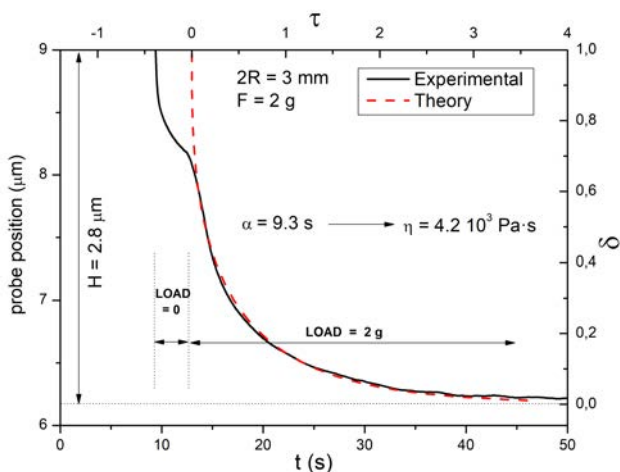


Figure 4.36: Fitting of a curve obtained from the analysis at 260°C of a film deposited with 4C+0.5%V/V DEA.

We observed that from 140°C, the film viscosity decreases one order of magnitude and then is maintained until 230°C. After this temperature, the viscosity increases again one order of magnitude at 260°C. At 290°C, viscosity is too large to measure it and at 320°C the curve shows a solid response.

The viscosity measurement for 4G solution shows also a decrease from 140°C (where viscosity was too large to be measured) reaching a minimum at 230°C. From this point viscosity increases again.

In figure 4.37 the viscosity values for the films deposited with 4C+DEA and 4G can be observed and compared.

The viscosity analysis of the measured curves show an interesting result. As it happened along this chapter, there is a drastic change on the thermal region from 150°C to 240-250°C and the segment from 250°C to the end of pyrolysis.

From the first segment we can observe a viscosity drop for the tested compositions, while after 240°C, viscosity rises until it becomes unmeasurable (huge

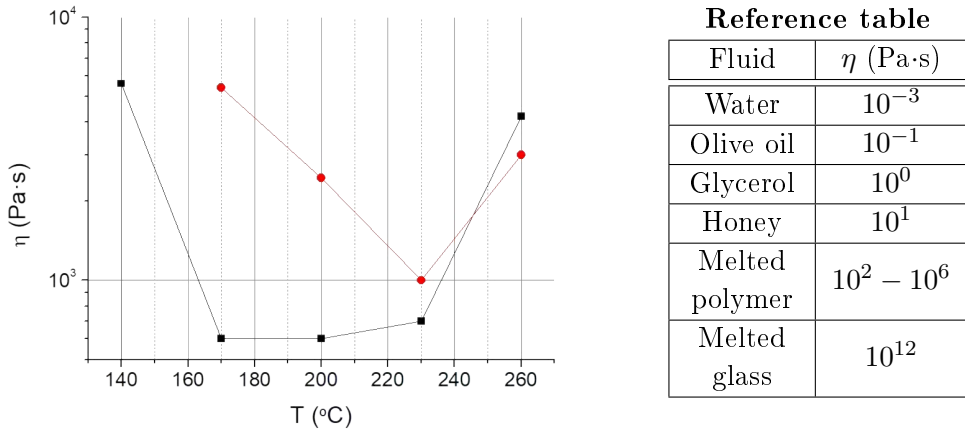


Figure 4.37: Plot with the viscosity values obtained from the TMA measurements of 4C + 05%_{V/V} DEA (black) and 4G 0.5M (red). To the right, we display some viscosity values as reference.

relaxation time), becoming a solid at the pyrolysis end.

The viscosity decrease in the first zone follows what will be expected for a liquid that is heated up. This is what we observe from 100°C to 240°C.

With this new information, two important factors regarding the buckling phenomena could be understood.

In a liquid-like state, the mass will be redistributed more easily than in a solid-gel state. For this reason, it is reasonable that the small compressive tension generated due to density loss can lead to the film buckling (usually film buckling occurs in soft substrates that compress faster than the film).

This mass redistribution "easiness" also justifies that the buckling can be reversed when the compressive stress is released.

If the films were hard and stiff films, as nanoindentation results showed for the quenched samples, the film would hardly recover from buckling.

We interpret that the viscosity recovering from 240°C is consequence of a solid fraction gain on the film. Thus the viscosity gain corresponds to a liquid

solidification towards the ceramic product. It is not clear how this solid fraction is generated but the most plausible possibility is the release of particles within an amorphous matrix.

We should remind the results reported in section 4.4, particularly in table 4.7, where we could conclude that there exist differences in the critical buckling values for different compositions.

Comparing those values with the viscosities obtained now from TMA, we can conclude that the trend is that the higher is viscosity for a composition, the higher is the film resistance to buckle.

Since the viscosity is defined as the resistance to deformation by a shear or tensile stress, it makes sense to relate both phenomena.

4.8 Results on the non cracked thick films synthesis

Due to the knowledge achieved during the physico-chemical analysis pyrolysis process we were able to optimize the ink formulation and the thermal process to obtain non cracked thick films.

Using the 25/1/5 ramp we could completely avoid buckling formation for all the used ink formulations.

To deal with cracking formation, diethanol amine (DEA) was added to the ink formulation in a 0.5%_{V/V} (10%_{mol}), greatly increasing the mechanical resistance to crack.

After this optimization we could synthesize non cracked films with a thickness of 700-800nm with a 50% of reproducibility.

After pyrolysis, the films presented the precursor species (BYF, CuO, CuO₂) necessary to grow a superconducting YBCO film. In addition we studied the pyrolyzed film cross section by scanning electron microscopy (SEM).

In order to study the film cross section we used the Focused Ion Beam (FIB) to ablate the film while imaging with SEM.

The cross section analysis (figure 4.38) shows a homogeneous distribution

of small pores for all the tested ink compositions (4C, 4C+0.5% V/V DEA, 4G) In this figure we show the large thickness achieved after pyrolysis.

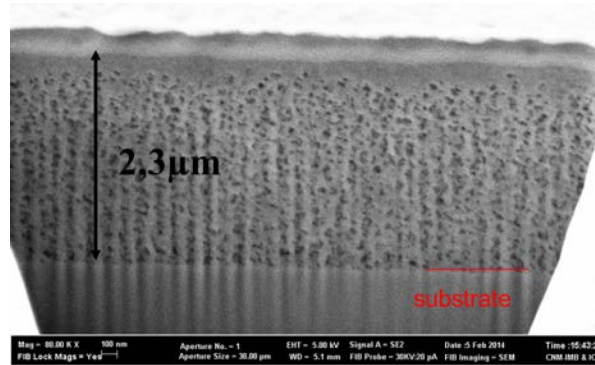


Figure 4.38: Film cross section SEM micrograph of a film deposited with 4C + 0.5% V/V DEA with a nominal thickness of $1\mu\text{m}$ after growth.

The homogeneity in the microstructure indicates a smooth pyrolysis process, without any phenomena that may leave big pores or inhomogeneities during the process. This is specially important for the DEA addition, since we observed its detrimental combustion when a value above 1.5% V/V was added as we reported previously.

Still, the synthesis reproducibility is to be greatly improved if long length films are to be produced. But the problem in obtaining non cracked films does not lie in the pyrolysis parameters but in the deposition homogeneity.

In the next section we will present the effect of the thickness homogeneity on the film cracking.

4.8.1 Thickness homogeneity effect on the film cracking

As was explained before, interferometry resulted of great use for the film thickness and film homogeneity characterization after pyrolysis.

In order to measure the sample homogeneity, a matrix of points are acquired. This matrix oscillates between 3x3 and 7x7 pints depending on the resolution

that we want to obtain, and afterwards we generate a contour graph. In figure 4.39 we show a schematic representation of how we obtain the thickness maps.

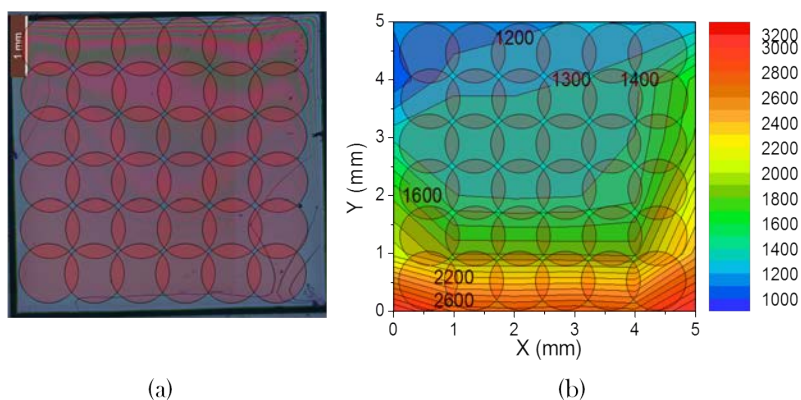


Figure 4.39: Example of the map generated from the thickness measure of a film using a matrix of 6x7 (42 measurements). In (a), the measured film, where the red translucent circles represent the point where a measurement was acquired. In (b) we show the contour map generated from the interferometer thickness measurements.

From the many measured samples, it was evidenced that the more inhomogeneous is a film, the more cracked it results after pyrolysis. For samples with a nominal thickness between 700 and 850nm after growth, only the films presenting differences below a 20% of the mean thickness value could be pyrolyzed without cracks.

The reason is that an inhomogeneous film will present zones surpassing the critical thickness for the crack formation. In these zones the crack will nucleate and propagate along the sample.

In figure 4.40, the optical image and the thickness map are compared for two films with a different degree of homogeneity. In this example it can be observed that the inhomogeneous film cracked while the homogeneous film did not present any defect.

Both films were deposited using $4C + 0.5\%_{V/V}DEA$ solution, with a nominal thickness of 800nm after growth and the 25/1/5 thermal process was used.

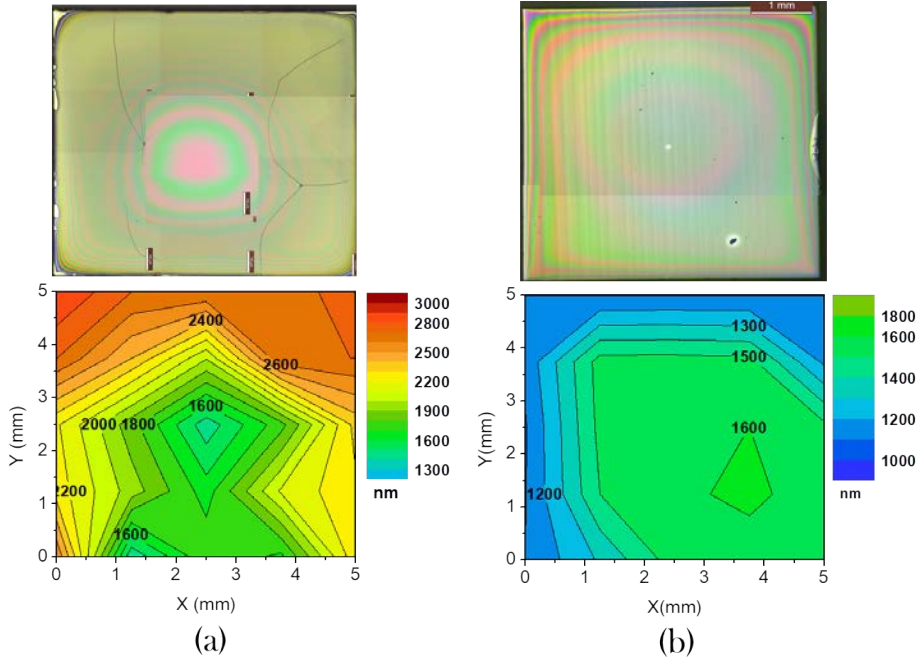


Figure 4.40: Comparison of the thickness homogeneity and its effect on the film quality. In (a), a coffee ring inhomogeneity led to crack formation. In (b) an homogeneous film with no cracks is observed.

4.9 Chapter summary and conclusions

A wide variety of studies have been performed on the films to analyse the pyrolysis stage, most of them based on an in situ approach while the films were pyrolyzed; the morphology, thickness, mass loss, heat flow, composition and mechanical properties were analysed in parallel, thus providing us an unique global picture of the whole organic firing process.

In the next points we proceed to summarize the information generated during this pyrolysis study:

- We successfully implemented a novel technique for the CSD films named pyrolyzer, consisting of a heating stage coupled to an optical microscope. It allowed us the optical observation of the surface of the films during the pyrolysis stage under controlled atmosphere and heating ramps. This allowed us to easily identify the critical zones during the pyrolysis process.

Before the pyrolyzer analysis, it was a general believe that stress could either crack or buckle the film but once the stress was released no further evolution of the defects should occur. Our study has demonstrated that this idea was not sustained. We have observed, instead, an unexpected phenomenon: film buckling can be reversed if the heating rate does not surpass a certain limit, depending on the characteristics of the ink composition.

Thanks to the information generated by the pyrolyzer, we have been able to optimize the thermal process for each solution in order to avoid buckling and reduce significantly the film cracking.

- We also performed studies on the mass thermodynamic and composition changes. This encompasses the use of TGA, DSC, EGA and IR spectroscopy. From these studies we identified the different phases of the organic mass decomposition. It starts at 150°C, and there exist two large decomposition stages around 220°C and 280°C, with small variations depending on the ink composition.

In order to analyse the specific species decomposed during the process, we quenched the films at several temperatures and analysed them by Infrared spectroscopy. This study, in combination with EGA, allowed us to conclude that all the mass lost below 280°C corresponds to propionates decomposition. It is above 280°C that the trifluoroacetates decompose.

- On the same way that we could couple the pyrolyzer to the optical microscope, we coupled the pyrolyzer with an interferometer. With this system we could in situ control the film thickness during pyrolysis. Until now, the in situ thickness evolution during a thermal process has not been reported for CSD samples.

Studying the thickness evolution with temperature, we observed that the film shrinkage does not start when the decomposition begins. Until 200°C, the thickness remains constant. Above 200°C, the thickness begins to decrease linearly with temperature.

By means of thickness studies in isothermal regimes, we could conclude that this was not a kinetic effect, and we also could conclude that it is from 220°C that the film start to shrink.

Comparing the thickness studies with the mass loss determination, we could conclude that the decomposition generates at low temperatures a density decrease, leading to a compressive regime that it is interpreted as the driving force for the buckling formation.

After 200-220°C, the stress regime changes from compressive to tensile, since the film shrinks faster than mass loss. This crossover coincides with the buckling recovery of the film. It is above this temperature that the film cracking occurs.

- To complete our physicochemical characterization of the pyrolysis landscape, we developed a novel methodology for the in situ film mechanical testing. We used a Thermomechanical Analysis (TMA) apparatus working under the same principles that the nanoindenter. With this equipment we obtained the in situ film displacement response to an applied load during the pyrolysis process.

Using TMA as an in-situ mechanical analyser system, we were able to successfully perform a mechanical characterization along the thermal process in less than 1 hour.

These measurements showed unexpected results that we could not have anticipated by means of nanoindentation analysis of quenched samples.

During the pyrolysis process, the mechanical behaviour of the film does not match with the one of a gel or a ceramic. Instead, we obtained a liquid like response.

Measuring the film viscosity, we observed that it decreased with temperature (as expected for a liquid) until 240°C. When this temperature is

surpassed, the viscosity of the system increases again until the mechanical properties are those characteristics of a solid at 320°C. We attribute the viscosity increase to the formation of a solid fraction on the film; the observed change of viscosity matches with the temperature where the film thickness was found to collapse.

- In addition the observation of an intermediate liquid formation justifies how it is possible that the film flatness is recovered after the huge deformation produced during film buckling: only a liquid system could redistribute the mass of the film to become flat again. This is the first time that such a phenomenon is reported.

We also observed that the film is more reluctant to the buckling formation when larger viscosity values are achieved by modifying the ink composition.

All the performed studies share a common result: the process is clearly divided in two stages, with a turning point around 240°C.

In table 4.15 we gathered the most significant information obtained from our physico-chemical studies when comparing the stage extending from 150°C to 240°C with the stage defined between 240°C to 320°C.

Film parameter	150-240°C	240-320°C
Stress type	Compressive	Tensile
Stress effect	Buckling	Cracking
Organic mass decomposed	0-50%	50-100%
Thickness lost*	0-25%**	25-100%
Precursor decomposed	Propionates	Prop. and TFA
Viscosity	Descending	Rising

Table 4.15: Summary of the film properties for the significant temperature segments.

*Calculated from the total thickness loss.

**Until 220°C the thickness only decays a 5%.

Gathering all the information obtained from the physico-chemical study of the pyrolysis we were able to optimize the thermal treatment and the solution

composition in order to obtain thick non cracked films.

But in addition we have obtained the tools to optimize, not only the different pyrolysis parameters to obtain YBCO thick films, but also for the pyrolysis of any functional material synthesized through the Chemical Solution Deposition - Metallorganic Decomposition (CSD-MOD) methodology.

With the morphology analysis performed with the pyrolyzer we could easily detect the critical zones during the pyrolysis process. Buckling can be controlled by slowing the heating rate in the thermal region where it is formed. But also we learnt that we could not overcome the crack formation by only slowing the heating rate.

We also concluded that below the buckling formation temperature the heating rate can be increased to 25°C/min, avoiding an unnecessary time expense by going at slow heating rates.

With the studies on thickness and mass evolution we detected that the film collapses when the trifluoroacetates decompose.

We understood that, to increase the film thickness without crack formation, an additive with functional groups capable to form networks is required. This additive will smooth the film collapsing by holding the films structure, and thus, avoiding an abrupt tensile stress generation.

It is preferable that the additive has a small weight to avoid the stress formation due to the mass contribution. Also the additive must decompose at a different temperature from the TFA decomposition one to avoid the simultaneous decomposition of the both molecules acting as a film skeleton.

Our additive of choice has been diethanolamine (DEA) in a 10%_{*mol*} ratio respect the sum of salts. This compound has a small molecular weight respect the organometallic precursors and it is a chelating agent capable of forming chemical bounds with the metals. In addition, as it was demonstrated from TGA, it decomposes at latter stages than TFA.

Finally from the mechanical in situ measurements we could identify the film mechanical behaviour during the pyrolysis. We concluded that the ink composition that led to higher viscosities during pyrolysis had an enhanced

resistance to be permanently buckled.

The effect of having a solid or a viscoelastic regime during the pyrolysis is still to be explored.

As a result of this physico-chemical analysis we were able to obtain non cracked thick films with an acceptable statistics (around 50% form films with 700-800nm after growth). Considering that most of the works on YBCO synthesis through CSD methodology are not able to achieve films thicker than 200-300nm this is a very encouraging result.

In the next chapter we will demonstrate that, by improving the ink composition, we can obtain a higher deposition homogeneity and a higher film resistance to crack we will demonstrate during the next chapter that the $1\mu\text{m}$ thickness can be surpassed for YBCO films synthesized by the CSD route.

Besides the pyrolysis process optimization, along the study we have designed several techniques for the in-situ characterization of the different pyrolysis parameters during the thermal process.

In addition, we have obtained a deep knowledge on the pyrolysis process, which was fully unknown until now. This knowledge has been crucial to obtain a YBCO film thickness above $1\mu\text{m}$ presented in the following chapter.

Reproducible inkjet printing of homogeneous YBCO thick films

5.1 Homogeneity problem

At this point we have studied the different parameters affecting the deposition and pyrolysis process for thick YBCO films deposited by inkjet printing following the CSD route. We could optimize the parameters for both processes obtaining thick superconducting films, however, we concluded that the $1\mu\text{m}$ homogeneity should be improved in order to achieve a higher reproducibility in the superconducting properties of the film since we could obtain only a 50% success rate (non cracked films). If several kilometre length films are to be produced, this success ratio is not acceptable.

In figure 5.1 we show a representative example of the film homogeneity effect on the film quality.

We found that, in order to obtain a non cracked film, the maximum thickness difference must be lower than a 20%. This is critical for films between 800 and 1000nm (nominal thickness after growth), otherwise the accumulation will overpass the critical thickness and cracks will be formed.

Furthermore, even if the film is not cracked, an inhomogeneous film will decrease the growth quality since every thickness requires a specific thermal treatment: the growth conditions of a 700nm film are different from the ones required for a $1\mu\text{m}$ film. It also has to be noticed that the thinnest film section will limit the current passing through the film.

For all these reasons, it is important to guarantee an homogeneous film deposition at a high rate, with a robust solution composition and deposition parameters.

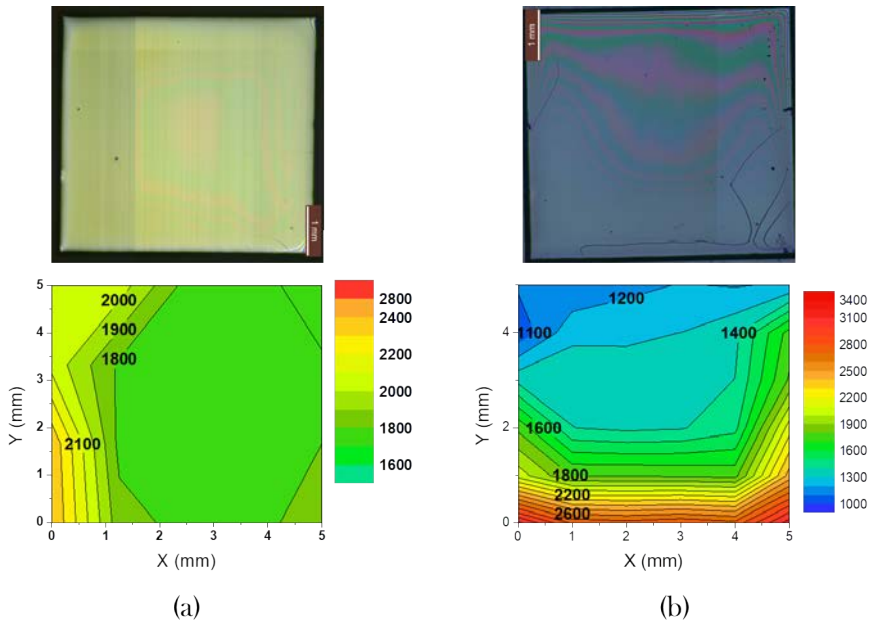


Figure 5.1: Homogeneity effect on film cracking. (a) map of a highly homogeneous (down) film with the optical microscope image (up) showing no cracks. (b) Film with liquid accumulation and cracks nucleation.

We will devote this chapter on how we solved the homogeneity problem, increasing the film reproducibility and achieving large film thickness, and thus, optimizing the final product performance.

5.2 Possible approaches to improve thickness homogeneity

The deposition of homogeneous films is a largely studied topic for all the existing deposition techniques. Multitude of approaches have been tried with greater or lesser degree of success. The tensioactives to compensate the coffee ring effect by Marangoni flow [128, 152], low boiling point co-solvent use to control solvent evaporation [153] and changes on the surface energies to increase the liquid-substrate affinity [92] are some examples of the work done on the

homogeneity enhancement.

But the most suitable approaches for our facilities and deposition technique are the following ones:

1. Change the viscosity of a solution. The hypothesis consists of counteracting the driving forces of the liquid movement (i.e. capillarity) by viscous dissipation [127, 154].
2. Keep the film wet to avoid the liquid movement caused by inhomogeneous evaporation and performing an photo-curing to initiate a polymerization reaction that will swiftly fix the film [44, 155].

5.3 Viscosity increase for the homogeneity improvement

We already tried to increase the film homogeneity by adding diethanol amine in a 10%_{V/V} to the 4C solution. The deposition results in highly homogeneous films, but when the film is pyrolyzed, this additive combusts, resulting in the film destruction.

Among all the suitable candidates that can be found to increase the film viscosity (PVP, diglyme, ethylenediamine, TMDA, etc.) we selected polyethylene glycol (PEG) as the most suitable one due to its low decomposition temperature (200°C) and the previous knowledge reported within SUMAN group[146].

Two PEG chain lengths were tested to increase the solution viscosity: PEG₈₀₀₀ and PEG₂₀₀₀₀ with a mass percentage of 5, 10 and 15%_{wt} in propionic acid. All the mixtures were soluble in the solvent after 1 hour stirring under 50°C.

The viscosity was tested at 20°C. The most promising results were PEG₈₀₀₀ with a 15%_{wt} and PEG₂₀₀₀₀ with 10 and 15%_{wt}, the values at 20°C were 16.5mPa·s, 22.7mPa·s and 52.8mPa·s, respectively.

Viscosity was measured at 35°C, 50°C and 75°C; the results can be shown in table 5.1

Since the practical viscosity limit to deposit with the single nozzle inkjet printer is 20mPa·s, the solution with the PEG₂₀₀₀₀ additive has to be heated

Viscosity (mPa·s)	PEG ₈₀₀₀			PEG ₂₀₀₀₀		
	5%	10%	15%	5%	10%	15%
Temperature						
20°C	4.8	9.9	16.5	8.7	22.7	52.8
35°C	/	/	11.2	/	15.7	34.0
50°C	/	/	10.3	/	13.0	26.1
75°C	/	/	6.8	/	8.4	16.6

Table 5.1: Measured viscosity for several concentrations (%_{wt}) of PEG₈₀₀₀ and PEG₂₀₀₀₀ in propionic acid.

to reduce its viscosity below this value. To avoid solvent evaporation on the reservoir, only the nozzle was heated, which can be heated up to 70°C.

In figure 5.2 we show optical images after drying of films deposited with the PEG additions.

When a 4C 0.5M solution was deposited with a 5%_{wt}, the resulting film presented huge liquid movements. Increasing the PEG percentage to 15%_{wt} led to an even more inhomogeneous liquid distribution and to film cracking during drying.

From the results obtained, we considered that tuning the viscosity is not a good approach since it does not show any improvement on the film homogeneity.

5.4 Photo polymerizable varnishes for the homogeneity improvement

After discarding the viscosity approach as a route to avoid inhomogeneity, we proceeded to the homogeneity enhancement through light curing.

By performing different deposition tests of our inks we observed a homogeneous liquid distribution until the solvent is evaporated. Thus, our proposal is to fix the film by triggering a polymerization reaction before solvent evaporation.

A photo curable varnish consists of a mixture of monomeric and oligomeric

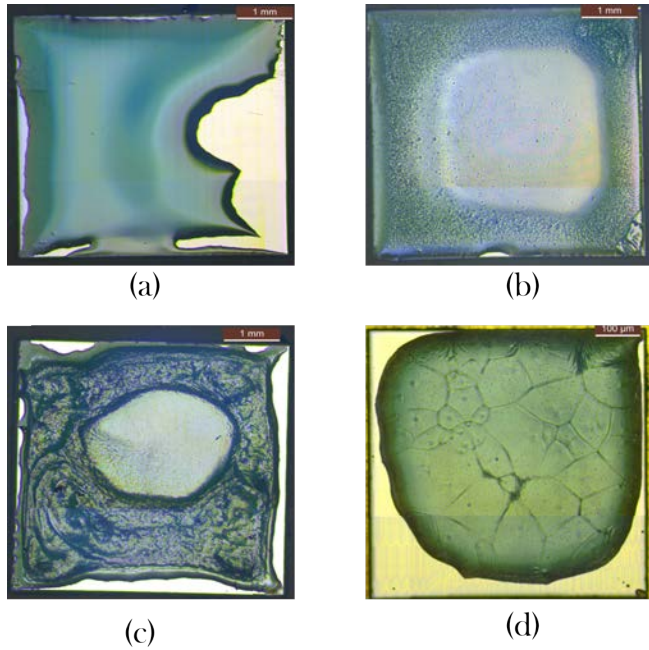


Figure 5.2: Optical microscope images of a film deposited with a nominal thickness of $1\mu\text{m}$ after growth, using a 4C solution with (a) $5\%_{V/V}$ PEG₂₀₀₀₀ dried at RT; (b) $5\%_{V/V}$ PEG₂₀₀₀₀ dried at 50°C ; (c) $15\%_{V/V}$ PEG₂₀₀₀₀ dried at 100°C ; (d) $15\%_{V/V}$ PEG₂₀₀₀₀ dried at RT. All the films presented a highly inhomogeneous liquid distribution.

molecules, and a photo-initiator. Influenced by light, usually on the UV range, the photo-initiator forms free radicals that splits the double bonds of the monomers and oligomers. The broken bonds reassemble forming a polymer in a free-radical reaction, generating a 3D network [156].

Depending on the varnish purpose and features, other additives can be added (e.g. stabilizers, pigments, inhibitors...). In figure 5.3 a scheme of the polymerization reaction is displayed.

Through an industrial partnership with Chimigraf company (KAO), two polymerizable varnishes were designed for inkjet printing deposition.

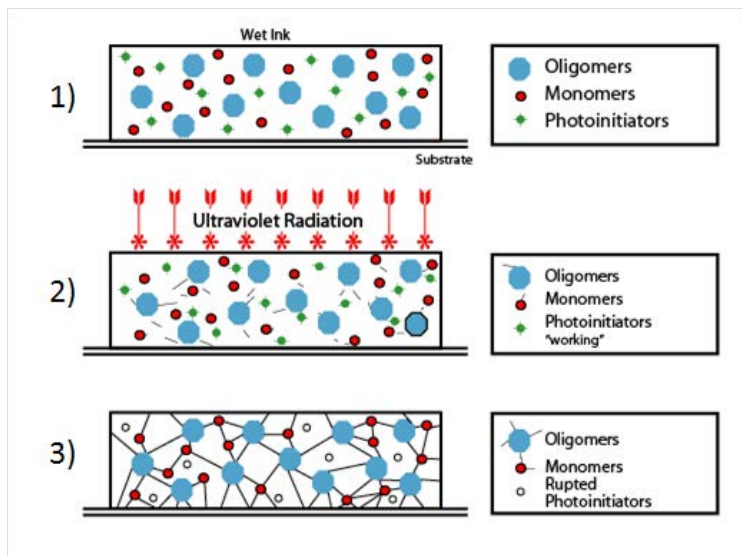


Figure 5.3: Schematic representation of the polymerization triggered by UV light of the molecules present in a UV curable ink. 1) The monomers and oligomers that will create the polymeric network together with the photoinitiators are added to the ink in the form of a varnish. 2) The photoinitiators interact with the UV releasing free radicals to the system. 3) The free radicals attack the monomers, usually containing a carbon-carbon double bond, triggering the polymerization reaction.

5.4.1 Preliminary tests on the curable varnish

The varnish was designed to act as ink, not as an additive. The mixture of the varnish with our inks must fulfil the proper rheology and stability conditions. We also checked if the varnish decomposition was complete in the pyrolysis temperature range, as well as the printing performance of the varnish when mixed with our designed solutions (4C and 4G). In order to test the feasibility of the varnish addition to the low fluorine inks, as well as the inkjet performance of the mixture, we carried out the verifications detailed in the next sections.

5.4.1.1 Varnish organic matter decomposition

The mass evolution of the solution when the varnishes were added was studied by TGA. The following conditions were used for the TGA experiment:

Technique	Heating ramp	Temperature range	Atmosphere
TGA	25°C/min	50-800°C	O ₂

Table 5.2: Thermal analysis experimental conditions for samples containing varnish table n°1

The resulting curves from the TGA are displayed in figure 5.4.

Varnish 1 (V1) What it can be observed from the TGA curve o the varnish 1 (figure 5.4 (a)) is that the varnish decomposition is completed at 600°C. In our thermal process we perform a 30 minutes dwell at the final temperature of 500°C to ensure the complete decomposition. We checked by IR that all the organic mass is decomposed at the end of the pyrolysis.

From the TGA we can observe that the main mass decomposition (a 60% of the total mass) occurs at 200°C.

After crossing this temperature, the mass is progressively lost until 450°C, where a 95% of the organic mass has been decomposed.

As it can be observed from our results, the greatest decomposition peak occurs before the cracking temperature, where the tensile stress becomes critical. The remaining mass is decomposed between 200°C and the pyrolysis end. This guarantees a smooth varnish decomposition and so it prevents an abrupt stress generation during the TFA decomposition around 280°C.

Varnish 2 (V2) On the other hand, the TGA performed on varnish 2 (figure 5.4) shows two main decomposition steps. A first one located at 190°C, and a second, very abrupt, at 290°C.

The second decomposition stage is located at the same temperature where the trifluoroacetates decompose, so it is very critically located at the cracking

zone of the thermal profile.

This may result in large stress accumulation at the most critical pyrolysis stage, strongly increasing the film cracking probability.

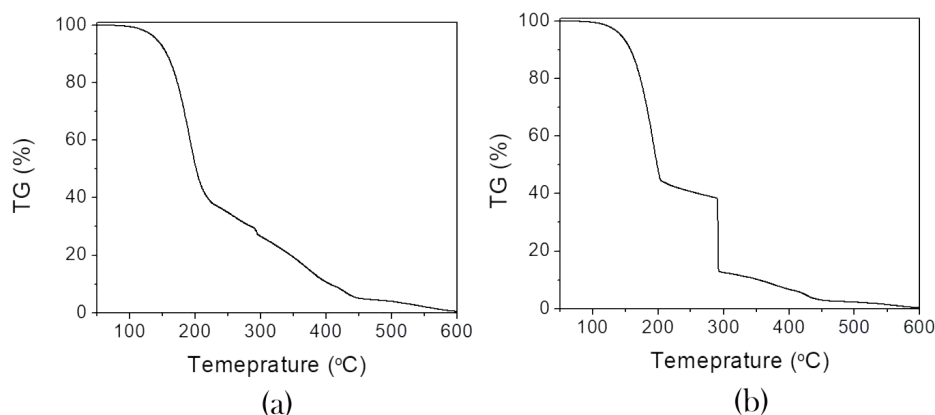


Figure 5.4: Thermogravimetric analysis (TGA) performed under O₂ on a deposited film of (a) Varnish 1 and (b) Varnish 2.

5.4.1.2 Varnish rheology and stability in the low fluorine solution

We tested the varnish stability by measuring the viscosity over time and checking the sample turbidity. We performed this inspection for both varnishes and for the mixture of the varnish, adding a 10%_{V/V} of varnish to a 4G solution with a concentration of 0.5M.

In table 5.3 the viscosity values and the solution aspect are noted during a period of 10 days.

From the obtained results we could observe that Varnish 1 is completely stable for 10 days. On the other hand, Varnish 2 loses transparency after 4 days and some precipitates appear after 1 week from its synthesis.

When Varnish 1 is added to the 4G solution, we observe that after 10 days the ink becomes turbid and the viscosity increases. The viscosity increase is also observed for the 4G + Varnish 2 at the 10th day, although the ink presents

a clear aspect.

	Varnish 1		Varnish 2	
	Viscosity (mPa·s)	Aspect	Viscosity (mPa·s)	Aspect
Day 0	20.0	Clear	17.7	Clear
Day 2	19.9	Clear	17.5	Turbid
Day 4	20.3	Clear	16.7	Turbid
Day7	20.2	Clear	16.8	Precipitated
Day 10	19.6	Clear	20.3	Precipitated
	4G+10% _{V/V} V1		4G+10% _{V/V} V2	
	Viscosity (mPa·s)	Aspect	Viscosity (mPa·s)	Aspect
Day 0	8.2	Clear	8.2	Clear
Day 2	7.8	Clear	8.0	Clear
Day 4	8.0	Clear	7.9	Clear
Day7	7.9	Clear	7.9	Clear
Day 10	9.0	Turbid	8.7	Clear

Table 5.3: Monitoring of the varnishes and solution with varnish stability and viscosity for 10 days.

For the ink preparation we add the varnish to the previously prepared 4C or 4G solution. We stir it for 15 minutes in dark conditions and then the ink is ready for deposition.

Since the addition of varnish to the solution is done minutes before the deposition, the stability of varnish 1 (7 days) is good enough for its use in our process. But for an industrial design, a longer stability could be probably required.

Varnish 2 is not stable itself, showing a turbid aspect after 4 days. For this reason, together with the mass decomposition profile shown in the TGA, Varnish 2 was discarded.

5.4.1.3 Deposition and printing test

We carried out a deposition using a solution with the varnish mixed with 4C and 4G solutions in order to see the mixture suitability.

Both mixtures were prepared using 0.5M concentration and adding a 10%_{V/V} of Varnish 1.

We were able to easily obtain a stable drop using the next waveform parameters:

- 4C 0.5M + 10% V1: wave length = 56 μ s; wave width = 26V/-15V; drop volume = 59pL
- 4G 0.5M + 10% V1: wave length = 62 μ s; wave width = 35V/-20V; drop volume = 75pL

We deposited both solutions with a square drop pitch, aiming for 600nm to 1000nm of nominal thickness after growth. From the several results, we could observe an homogeneous film when printing with 4G+V1 solution. On the other hand, the printing with 4C+V1 presented liquid retraction, indicating a poor affinity for the substrate. In figure 5.5 we show an example of a film deposited with each solution.

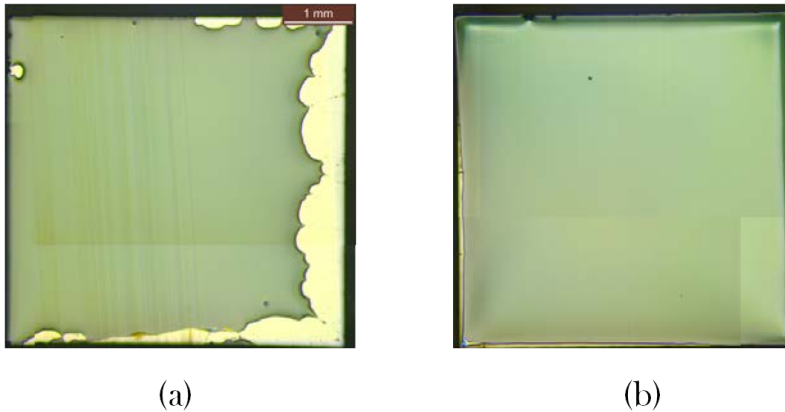


Figure 5.5: Comparison of the printing performance for (a) a 4C 0.5M solution with 10%_{V/V} of Varnish 1 and (b) 4G 0.5M solution with 10%_{V/V} of Varnish 1. Films deposited with a 25x25 drop pitch, aiming for 800nm after growth.

After the preliminary tests to check the varnish suitability with our solution and purpose, we decided that the 4G solution (80% butanol 20% propionic acid) mixed with varnish 1 was the most suited one for the thick film deposition.

5.4.2 UV Curing

The usual set up for the curing of photosensitive varnishes consist of a UV-LED lamp located at 395nm (in the threshold of visible-UV light) next to the printhead so it radiates the sample immediately after printing, fixing the film. In our case, the film must be cured after the deposition is completed. Because of the slow printing rate of the single nozzle system, to irradiate the film during deposition would imply to place the lamp next to the nozzle. This would cause the polymerization of the varnish inside the tray, changing the ink properties and blocking the nozzle.

This implies a time lapse between starting the deposition and the curing process of 5 to 20 minutes, depending on the used drop pitch .

To test the effect of the UV-LED light on our solutions, we performed a UV-visible spectroscopy analysis to determine the solution absorbance. We also performed several tests on the required light power to ensure that the varnish initiates the polymerization.

5.4.2.1 Ink UV absorbance

In order to verify the UV absorbance of the varnish, we performed a UV-visible spectroscopy. We analysed 3 samples: varnish 1, the mixture of a 4G 0.5M with a 10% of varnish and a 4G 0.5M solution without additives. All the samples were diluted 1 to 100 in butanol.

The varnish alone presents an absorbance peak with a maximum at 382nm. This is the wavelength that the photoinitiator absorbs to initiate the polymerization reaction. This absorbance is very close to the light emitted from our LED lamp (395nm).

At shorter wavelengths (<300nm) we can detect a saturated absorbance peak, where the polymerization will be stronger. There is a clear advantage of using a LED close to the visible range, since some works report the decomposition

of the YBCO organometallic precursors using UV radiation. With the 395nm LED we can fix the film after deposition without an early decomposition out of our control.

The 4G+varnish solution, also absorbs at this wavelength, but it additionally presents an absorbance broad peak at 689nm.

Interestingly, the low fluorine solution without the addition of varnish also presents absorbance at 382nm. This is a factor to consider when curing the film since the solution will heat up due to the interaction with UV light.

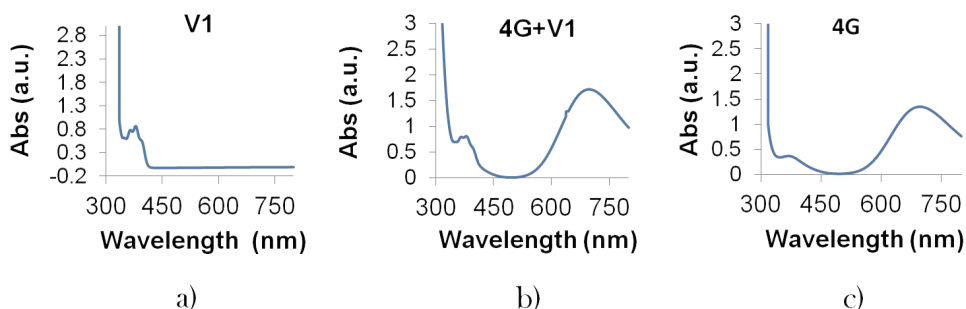


Figure 5.6: UV-visible spectroscopy curves for (a) Varnish 1; (b) 4G 1M + 10% V/V Varnish 1; (c) 4G solution 1M. The three samples were diluted 1 to 100 in butanol. All of them present absorbance at 382nm, very close to our 395nm peak of our LED (wavelength for the polymerization initiation). The samples with 4G solution also present a broad absorbance peak with a maximum at 689nm due to Cu^{2+} .

5.4.2.2 Curing testing

Since the varnish is diluted in the low fluorine precursor solution, we needed to confirm that the polymeric reaction could fix the sample.

We tested the UV effect on a 4G 0.5M ink and a 4G 0.5M with the addition of 10% V/V of varnish 1. The films were deposited by drop casting, using a drop of 2 μ L (volume for a nominal thickness of 1 μ m after growth).

The test consisted of curing a film with different UV power inputs (0.35W, 0.7W and 1.05W) during 5 minutes.

After curing, the film was softly wiped to check the effect of the curing on the film. In figure 5.7 we show an example of the wipe test effect on a film after deposition. The samples that were not affected by the wipe test were scratched with tweezers to test the texture.

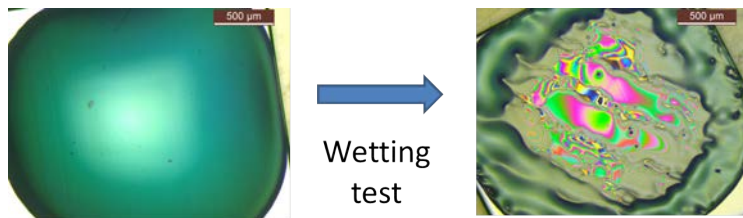


Figure 5.7: Optical micrograph for a film deposited by drop casting using $2\mu\text{L}$ of 4G 1M before and after wiping the film with a clean room wipe.

The films cured with the different LED intensities, before and after the tests, are presented in figure 5.8.

Once cured, the films presented a very different aspect depending on the used ink composition. The films deposited without varnish were more inhomogeneous, specially those cured at 0.35W and 1.05W.

On the other hand, the films deposited with varnish and cured at 1.05W seems to indicate an aggressive process. After the curing the film presents buckling and cracking, in addition to a yellow colour, which contrasts with the greenish hue of the rest of experiments.

When the films were cured with an input power of 0.35W, both 4G and 4G + Varnish were wet, so the wipe dragged the film as can be observed on 5.8(a) and 5.8(b).

The films cured at 0.7 and 1.05W remained fixed when the wipe test was applied for either solution composition.

In this case the films reacted differently to the tweezer scratching, depending on the ink: 4G cured films presented a gel texture while the 4G + V1 films

became a hard solid after curing.

From these tests we established 0.7W as the optimal UV lamp power.

When the film is cured at 0.35W (figure 5.8(b)) the polymerization process does not start. The 1.05W curing, on the other hand, is too aggressive for the film, resulting in a simultaneous buckling and cracking.

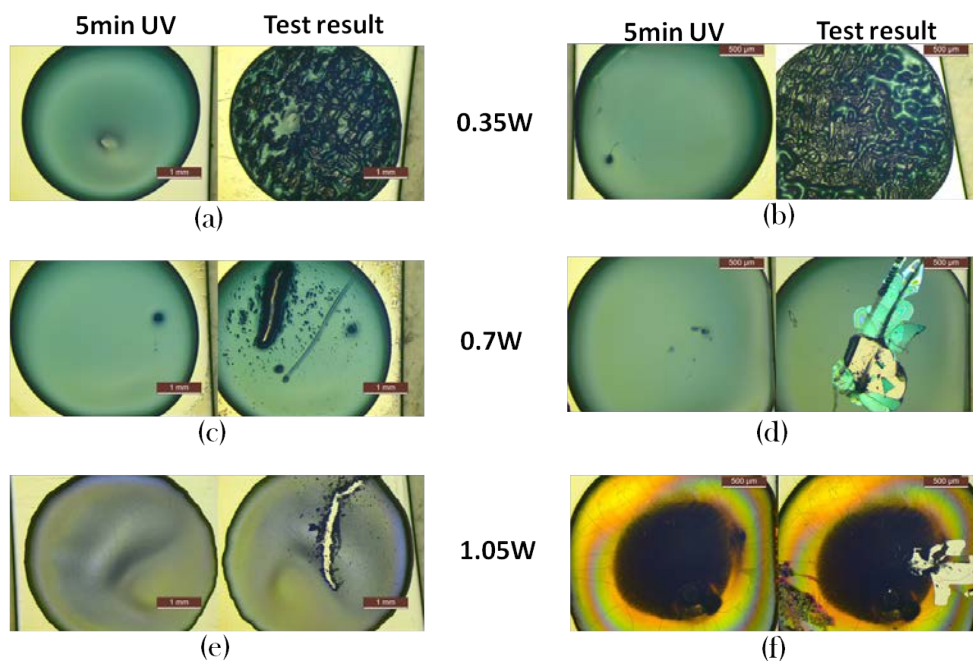


Figure 5.8: Testing of the LED curing on films deposited by drop casting using $2\mu\text{L}$ of 4G 1M (a, c, e) and 4G 1M + V1 10% $_{V/V}$ (b, d, f). The used input power for the curing was 0.35W (a, b) 0.7W (c,d) and 1.05W (e, f). Optical micrographs were acquired before and after the wetting test. (a) and (b) dewetted with the wipe while the rest of cured films were unaffected. (c), (d), (e) and (f) where scratched with metallic tweezers. (c) and (e) presented a gel aspect when scratched while (d) and (f) became a brittle solid after curing. 0.7W was decided as the optimum LED lamp input.

5.4.3 Ink design

After all the validations, we considered varnish 1 (V1) as a fitting additive for our system.

To study the morphology during the pyrolysis of the films deposited with varnish we used the in situ observation using the pyrolyzer.

For the first test, we deposited a film with an ink composed by 4G 0.5M + 10%_{V/V} V1, depositing a film with 700nm after growth. The pyrolysis was performed heating at 2°C/min. In figure 5.9 we show some images acquired during the pyrolysis. The full video can be watched in the following link [Pyrolysis of 4G 0.5M + 10%_{V/V} V1 ink](#)

	Used solution	Additives	Nominal thickness	Heating rate (°C/min)		
				160°C	240°C	400°C
1	4G 0.5M	10% _{V/V} V1	700nm	25	2	2

Table 5.4: Table of the used pyrolysis experimental conditions for samples containing varnish n°1

Using this ink composition, we obtained a perfect deposition, but the film heavily cracked during the pyrolysis process. The cracking is caused by the excessive thickness: For a nominal thickness of 700nm, we established a film thickness after drying of 7000nm without adding varnish; with the addition of a 10% of varnish, the starting thickness was around 17000nm (measured by interferometry).

As we can observe from the images obtained during the morphological analysis (fig. 5.9), buckling was formed at the same temperature range than all the low fluorine inks, and it could be reversed at heating rates of 2°C/min. We also observed that the film cracking was shifted to higher temperatures, starting at 290°C. As we mentioned, the cracking is too drastic to be avoided by simply tuning the pyrolysis parameters (heating rate, gas flow).

We tried to minimize the initial thickness increase by maintaining the homogeneous deposition caused by the varnish.

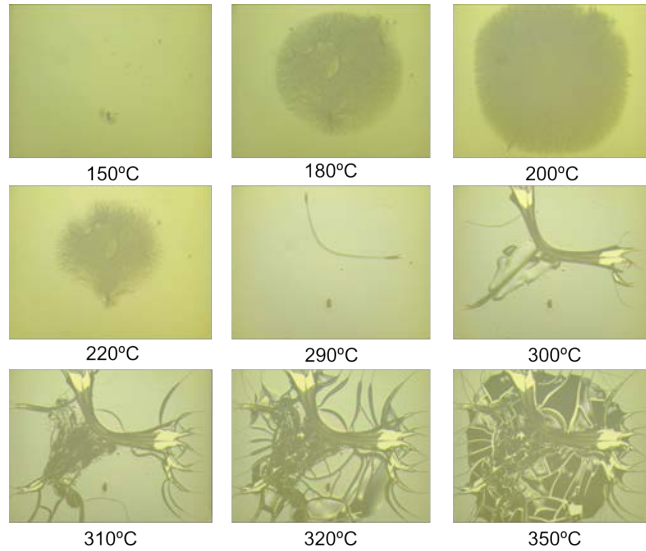


Figure 5.9: Optical micrographs obtained during a pyrolysis at 2°C/min of a film deposited with 4G 1M+ 10%_{V/V} V1 with a nominal thickness of 700nm after growth. Reversible buckling can be observed in the same temperature range than for films without varnish. At 290°C the film was hugely cracked.

To achieve this, we increased the solution concentration and tuned the varnish amount. By this approach we intended to decrease the varnish/salt molar ratio, that affects the thickness after solvent evaporation, keeping a high varnish/solvent volume ratio that improves homogeneity.

The next combinations were tried. All of them were deposited aiming for a nominal thickness of 700nm, obtaining the following results, also illustrated in figure 5.10:

1. 4G 0.5M + 10% V1 - Thickness after drying = 17 μ m. Perfect deposition, highly cracked film after pyrolysis
2. 4G 1.5M + 10% V1 - Thickness after drying = 10 μ m. Really inhomogeneous deposition, any improvement respect 4G 1.5M without the additive. With this composition we tried to reduce as much, as inkjet deposition

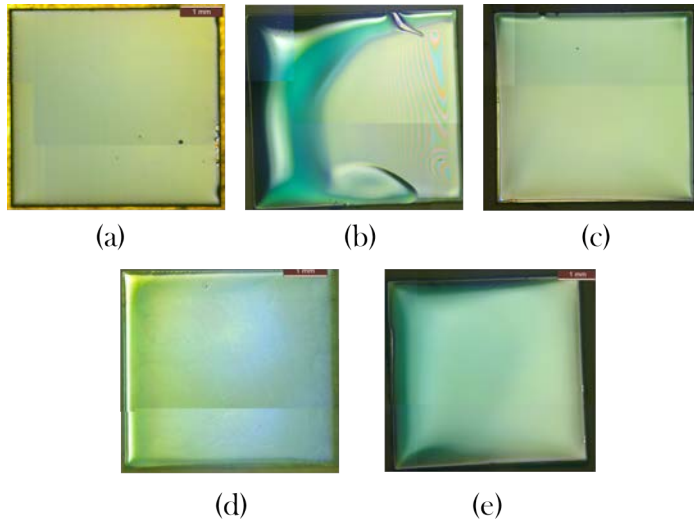


Figure 5.10: Optical micrographs showing films deposited with different concentrations and varnish proportions of 4G+V1 inks, with a nominal thickness of 700nm after growth. (a) 4G 0.5M + 10% V1; (b) 4G 1.5M + 10% V1; (c) 4G 1M + 6.6% V1; (d) 4G 1M + 5% V1; (e) 4G 1M + 3% V1. The composition used in (c) present the best homogeneity/varnish quantity relationship among all the screened compositions.

permits, the solution concentration, maintaining the varnish percentage of the first experiment.

3. 4G 1M + 6.6% V1 - Thickness after drying = $10\mu\text{m}$. Good deposition and pyrolysis. Composition designed to maintain the initial thickness of the former experiment.
4. 4G 1M + 3% V1 - Thickness after drying = $8.5\mu\text{m}$. Inhomogeneous deposition. Still better performance than 4G without varnish. This composition was designed trying to obtain the minimum varnish value for an homogeneous deposition, permitting thicker films without cracking.
5. 4G 1M + 5% V1 - Thickness after drying = $9.3\mu\text{m}$. The deposition almost as homogeneous as that in the case of 6.6%V1. The drawback of this composition is that strongly depends on the printing conditions (humidity, solution preparation), which can lead to inhomogeneous depositions

afterwards.

From all these experiments we defined the 4G 1M + 6.6%_{V/V} V1 as the most robust solution composition to obtain homogeneous thick films with high reproducibility.

5.5 Deposition of solutions with varnish

In this part we will repeat the deposition study for the 4G 1M + 6.6%_{V/V} V1. We studied the drop generation and deposition parameters reproducing the experiments presented in chapter 3.

5.5.1 Drop generation

In table 5.5 the ink parameters for the new composition are indicated:

Solution	Density $\rho(g/mL)$	Viscosity $\eta(mPa \cdot s)$	Surface tension $\sigma(mN/m)$	Contact angle θ ($^\circ$)	Z
4G 1M + 6.6% V1	1.067	8.00	25.62	19.7 - 7.5	5.06

Table 5.5: Ink parameters of the 4G 1M + 6.6%_{V/V} Varnish 1 ink.

The values indicate that the ink is suited for a stable inkjet deposition. The following waveform parameters were used to generate a drop: 60 μ s, 36V,-20V.

The larger pulse width and length required to obtain a stable drop, leads to drop volumes around 65pL., a factor 2 higher compared with the drop volume of 4C 0.5M solutions. As we explained before, the larger volume plays a beneficial effect in order to increase homogeneity.

In table 5.6 we compare the average drop conditions and parameters of the solutions with and without varnish.

From what we described above, we can conclude that the 4G 1M + 6.6% V1 is perfectly suited for deposition by inkjet printing.

Solution name	Composition (% volume)	Conc.	Viscosity	Waveform parameters	Drop volume*
4C+DEA	(99.5)prop. acid (0.5) DEA	0.5M	1.7mPa·s	50 μ s 23V/-13V	32pL
4G+V1	(73) butanol (20)prop. acid (6.6) V1	1M	8.0mPa·s	60 μ s 36V/-20V	69pL

Table 5.6: Comparison among the required waveform parameters and drop volume depending on the ink composition.

5.5.2 Liquid distribution homogeneity

Already during the first tests with the varnish addition, we could observe a great homogeneity improvement, even if the film was not cured with UV radiation. In figure 5.11 we compare two films deposited with 4G 1M with and without the varnish addition. The contrast was enhanced for a better homogeneity visualization.

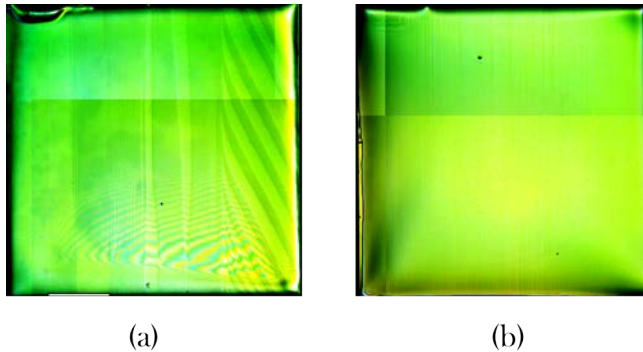


Figure 5.11: Optical micrographs allowing to compare the film homogeneities (a) 4G 1M and (b) 4G 1M + 6.6% $_{V/V}$ V1. Films deposited with a nominal thickness of 800nm after growth. From the images it can be observed the higher homogeneity of the sample deposited with the 4G+V1 ink composition.

5.5.2.1 Line merging study on single crystal substrate

To observe how the liquid is distributed during the deposition, we repeated the drop merging study. This study consists of printing lines of a constant drop distance on the X axis, varying the distance between lines (Y axis).

Recalling from the merging for 4C and 4G solutions we observed that:

- 4C solution lines became completely spread when deposited, being able to cover the whole $5 \times 5 \text{mm}^2$ substrate only with 10 lines.
- The lines printed using 4G solution were well defined, avoiding the film spreading when they were isolated. But when the lines were brought close to each other, they flowed towards the first deposited line (the driest one), generating uneven liquid distributions in what we call a "C" shaped inhomogeneity.

From this we concluded that the capillary attraction between neighbour lines was far stronger than the liquid-substrate interaction, thus promoting liquid movements.

The line drop merging study was done for 4G + 6.6% V1 with a constant drop spacing on X direction of $50 \mu\text{m}$.

In figure 5.12 we show the comparison of the experiment performed for a 4G solution 1M with and without the varnish.

There is a clear difference when the 4G + V1 ink is printed compared to the solution without varnish.

When the varnish is added to the solution, the liquid is not dragged to merge on the adjacent lines. Instead, the lines remain fixed printhead position. We concluded that the slower drying of the lines when the varnish is present prevents the line movement activation due to the capillary forces produced by the adjacent line drying.

Even when the lines are overlapped, the liquid movement is minimized, resulting in a homogeneous distribution for a $50 \times 50 \mu\text{m}^2$.

Still the liquid movement tendency is to move towards the beginning of the deposition.

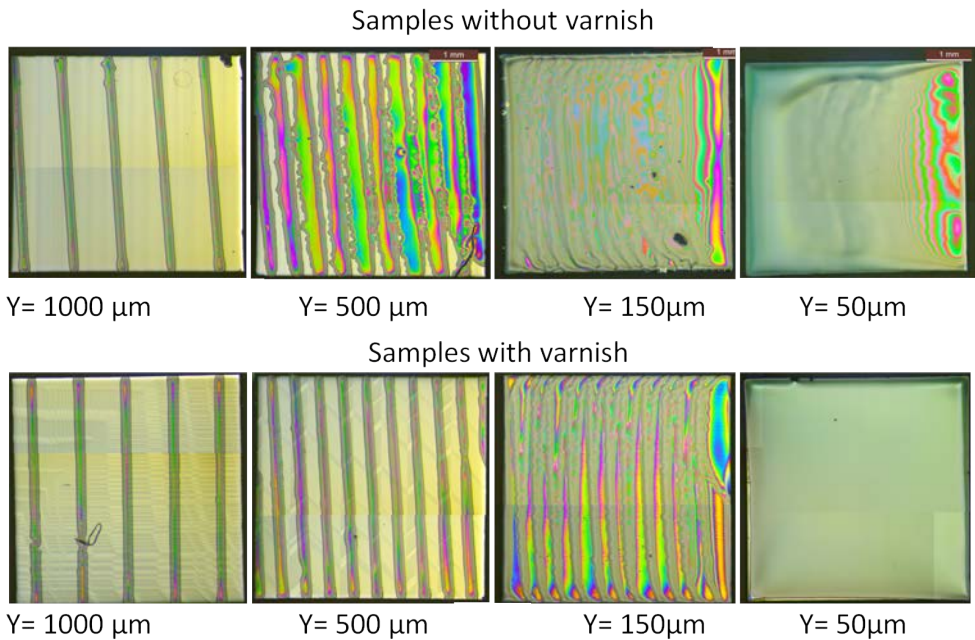


Figure 5.12: Line merging study comparison among 4G 1M and 4G 1M + 6.6% v/v V1. Both inks were deposited with a constant drop distance on X of $50\mu\text{m}$, modifying the distance on Y to observe the lines interaction from $1000\mu\text{m}$ to $50\mu\text{m}$. It can be observed that the lines deposited without varnish (up) experience a liquid movement towards the deposition beginning while the lines deposited with varnish (down) remain attached to the substrate.

5.5.2.2 Homogeneity enhancement through drop pitch

At this point it is clear that the varnish addition greatly enhances the film homogeneity. Still the deposition presented some tendency to form the "C" shaped inhomogeneity depending on the printing conditions.

Until now we have used a square drop pitch, for example $50\mu\text{m}$ of drop distance in X and $50\mu\text{m}$ of drop distance in Y (50×50). For a drop with an impact diameter of $170\mu\text{m}$, a drop spacing of $50\mu\text{m}$ implies a drop overlapping of 67% of the drop diameter as we have represented in figure 5.13.

If most of the liquid is being deposited on top of a drop, the liquid will tend

to redistribute flowing towards the already deposited film, causing a liquid inhomogeneous distribution.

To completely avoid the liquid movement the selected drop pitch was changed. The used drop spacing on X direction of $25\mu\text{m}$ while the drop distance on Y was changed between 60 and $100\mu\text{m}$ depending on the desired thickness and on the drop volume, so decreasing the drop overlapping only up to a 35% of the drop diameter.

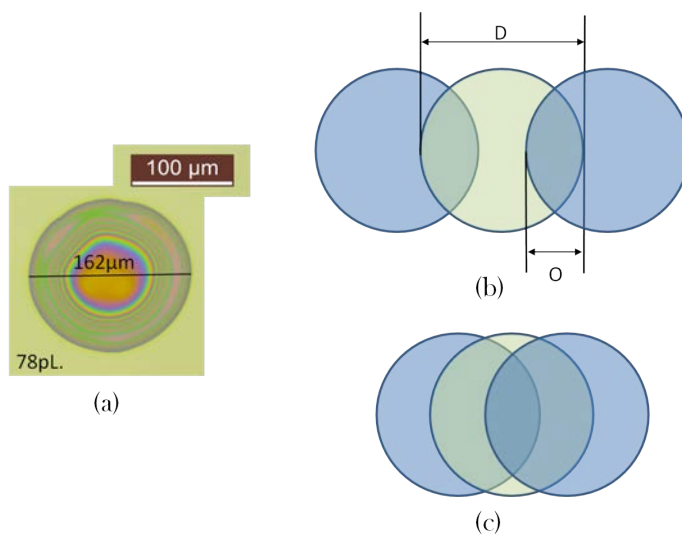


Figure 5.13: Schematic representation of the drop overlapping. (a) impact diameter of a drop of 78pL ; this drop impact diameter ($162\mu\text{m}$) was used as a model to the scale drawing. (b) Droplet diagram when the drop distance is of (b) $100\mu\text{m}$, presenting a drop overlapping of a 35% of the drop diameter, and (b) 100μ , with a drop overlapping of 67% of the drop diameter.

The drop overlapping is calculated with the next expression: $\frac{O}{D} \times 100$, being D the drop impact diameter and O the overlapped length between two neighbour drops.

5.5.3 Liquid distribution on metallic tapes

We repeated the line merging study on top of a Bruker SS/YSZ/CZO substrate with the 4G 1M + 6.6%_{V/V} V1. The deposition on tape showed similar results than the line merging experiment on LAO as it can be observed in figure 5.14. The lines are strongly fixed to the substrate, blocking the liquid movement. The printed lines on tape are more spread out, indicating a higher wetting on tape than on LAO.

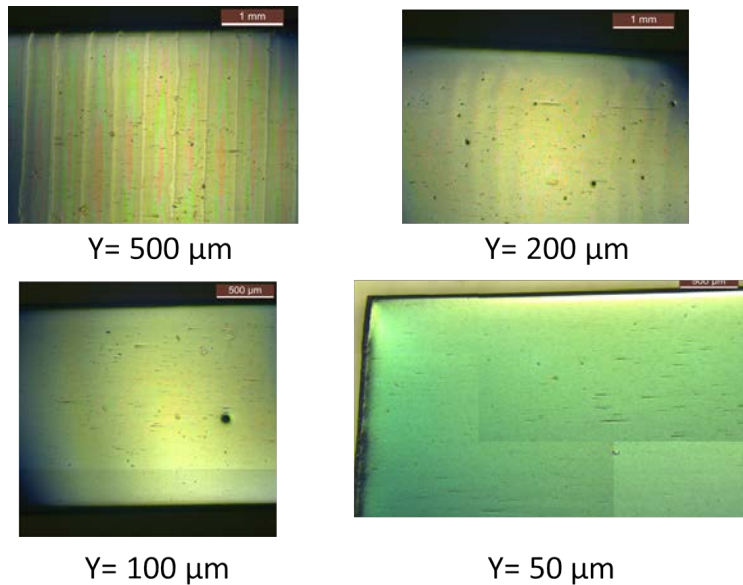


Figure 5.14: Line merging study of a solution 4G 1M + 6.6%_{V/V} V1 on a buffered metallic tape from Bruker. The drop distance in X was kept at $50\mu\text{m}$ and the distance in Y was changed from $1000\mu\text{m}$ to $50\mu\text{m}$. The lines remained attached to the substrate resulting in an homogeneous deposition.

From the experiment we observe a general higher homogeneity on tape. A probable cause is the substrate roughness, that aids to the liquid pinning to the surface. Even so, when depositing on top of Bruker buffered metallic substrate, we still observe a liquid accumulation on the substrate edge due to the perturbation of the edge itself.

Regarding a long tape production, this issue will not be relevant since the accumulation only affects up to 1mm from the edge. Beyond this millimetre, the film homogenizes, becoming flat for the rest of the film, as it can be observed in figure 5.15, where we display an optical image and its corresponding film thickness mapping of a pyrolyzed film deposited on a Bruker tape.

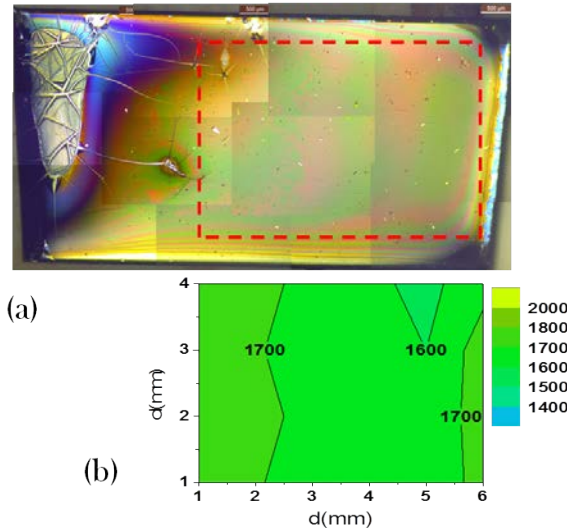


Figure 5.15: Liquid distribution of the 4G 1M + 6.6% V_V V1 on a 10mm buffered metallic tape from Bruker deposited with a nominal thickness of 950nm after growth. (a) Optical microscope image of the film where it can be observed the liquid accumulation at the edge of the tape. (b) Mapping of the film out of the accumulation region where it can be observed that a high homogeneity has been achieved.

To avoid printing from the substrate edge is, at present, the best option in order to obtain a flat and homogeneous film.

In figure 5.16 we show a tape where the first mm was not printed. The homogeneity improvement is clear when compared with the tapes printed from the edge (as the one presented in figure 5.15).

At this point we have demonstrated the advantages of using the varnish to achieve homogeneous thick depositions.

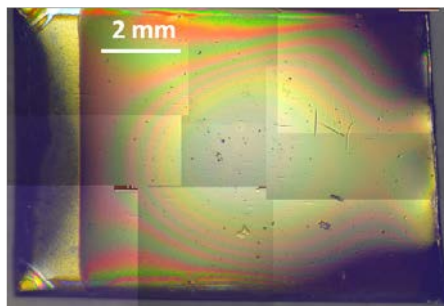


Figure 5.16: Optical micrograph of a pyrolyzed film deposited with 4G 1M + 6.6%_{V/V} V1 on a 10mm buffered metallic tape from Bruker with a nominal thickness of 850nm after growth. The first 1.5mm was not printed, avoiding the liquid accumulation at the tape edge.

We also tried to maintain the additive amount down to a minimum level in order to facilitate the decomposition process. For this reason there is still room for improvement since a larger varnish quantity would further enhance the homogeneity. Since the limiting factor is the film cracking due to the shrinkage, there are two paths to further improve our work:

- 1) To minimize the varnish organic matter contribution by changing its composition trying to maintain the properties that improve the homogeneity.
- 2) To understand and improve the pyrolysis process to avoid film cracking at this high thickness, as it will be described in the next section.

5.6 Pyrolysis physico-chemical analysis of films deposited with varnish

The pyrolysis physico-chemical analysis of the films deposited with the solution 4G 1M + 6.6%_{V/V} of varnish 1 was carried out following the same steps already presented in the Chapter 4.

The films morphology, mass evolution, thickness and mechanical properties were analysed by the presented in-situ analytical techniques.

5.6.1 Pyrolysis performance

We proceeded to pyrolyse the films deposited with the new composition. First, we used the heating stage to visualize the process. A film with 700nm of nominal thickness was pyrolyzed with a heating ramp of 10°C/min. The experiment objective was to determine if the pyrolysis critical zones were maintained with the new composition.

	Used solution	Additives	Nominal thickness	Heating rate (°C/min)		
				160°C	240°C	500°C
1	4G 1M	6.6% _{V/V} V1	800nm	10	10	10

Table 5.7: Pyrolysis experimental conditions table n°2

For the new composition we still observe the buckling formation at the same range than the rest of used inks. This indicates that the compressive stress is still present when varnish is added to the solution. At 10°C/min the buckling was totally reversed at a temperature of 220°C.

The cracking temperature of this film was at 300°C, 30°C higher than the typical cracking temperature detected for all the other analysed inks.

To establish the critical irreversible buckling rate (R_{B2}), we performed a pyrolysis at 20°C/min. We placed 2 samples of different nominal thickness in order to analyse them simultaneously, as we display in table 5.7. The video of this experiment can be watched in the following link: [Pyrolysis 20°C/min 4G 1M + 6.6%_{V/V} V1](#)

	Used solution	Additives	Nominal thickness	Heating rate (°C/min)		
				160°C	240°C	500°C
1	4G 1M	6.6% _{V/V} V1	810nm	20	20	20
2	4G 1M	6.6% _{V/V} V1	600nm	20	20	20

Table 5.8: Pyrolysis experimental conditions table n°3

For both samples, the buckling was formed at 180°C, being reversed at 225°C, even at this high heating rate. From the pyrolyzer inspection we could

observe that buckling was formed and reversed at the same velocity and temperatures for both films.

Furthermore, the sample with a nominal thickness of 600nm did not present crack formation. From these results we can conclude that the films with 4G 1M + 6.6% are the most resistant films produced along this work.

We decreased the heating rate looking for the critical rate for buckling formation R_{B1} . At 2°C/min we still observed buckling formation (even if at higher temperature was always reversed). It seems that, even if the R_{B2} is higher than the rest of ink compositions (4C, 4G, 4C+0.5% $_{V/V}$ DEA), the R_{B1} value is 5°C/min, in the same range than the 4C+DEA ink

In table 5.9 we gathered the different critical buckling rates and cracking temperatures observed for all the studied inks.

Solution composition	R_{B1} (°C/min)	R_{B2} (°C/min)	Cracking temperature
FF	<1	1	230°C
FF + 0.5% $_{V/V}$ DEA	1	5	230°C
4C	2	5	260°C
4C + 0.5% $_{V/V}$ DEA	5	10	260°C
4G	1-5	15	260°C
4G+V1	2-5	>20	300°C

Table 5.9: Buckling formation critical rate (R_{B1}), permanent buckling critical rate (R_{B2}) and cracking temperature depending on the ink composition.

5.6.2 Thickness and mass evolution

The thickness evolution of the films deposited with 4G+6.6% V1 was analysed by coupling the interferometer with the pyrolyzer heating stage.

The experiment was performed in the pyrolyzer with an O₂ atmosphere. The deposited film had a nominal thickness of 800nm after growth, with the thermal profile indicated in table 5.8.

In parallel, the mass evolution of the 4G+6.6% $_{V/V}$ V1 ink was analysed by

	Solution	Additives	Nominal thickness	Heating rate (°C/min)		
				160°C	240°C	400°C
3	4G 1M	6.6% _{V/V} V1	800nm	25	5	5

Table 5.10: Pyrolysis experimental conditions for samples containing varnish table n°4

TGA, with the conditions described in table 5.11:

Technique	Heating ramp	Temperature range	Atmosphere
TGA	20°C/min	50-800°C	Humid O ₂

Table 5.11: Thermal analysis experimental conditions table n°2

In the figure 5.17 we show the comparison of the mass and thickness evolution of films deposited with 4C 0.5M + 0.5%_{V/V}DEA and 4G 1M + 6.6%_{V/V}V1.

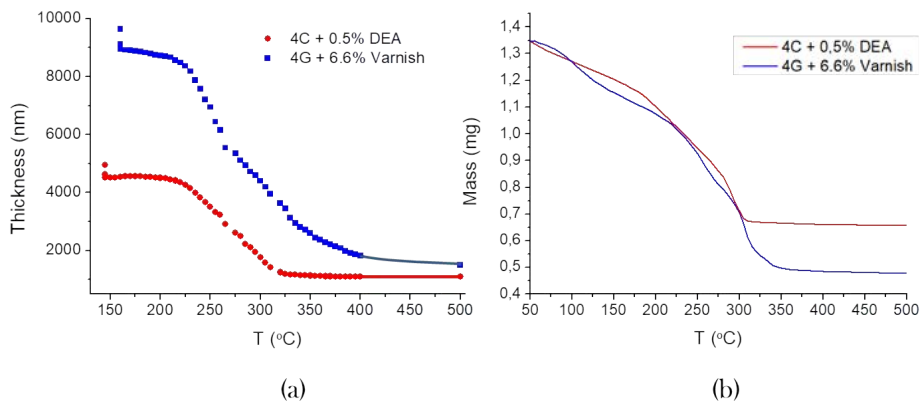


Figure 5.17: Comparison of the mass and thickness evolution in-situ study of films deposited with 4C 0.5M + 0.5%_{V/V}DEA (red) and 4G 1M + 6.6%_{V/V}V1 (blue). (a) Thickness evolution studied with the coupling of the pyrolyzer with the interferometer. (b) Mass evolution study by TGA

Comparing the thickness evolution of the films deposited with varnish with the film without the additive (figure 5.17(a)) we can observe a similar progres-

sion: Below 240°C the thickness remains almost constant. Above 240°C the film starts to collapse, however at 400°C the film did not achieve yet a constant thickness in this case.

However some important differences can be detected from the analysis on thickness. The most important is the huge thickness increasing due to the varnish addition. The initial film thickness is increased in a factor 2 respect the films deposited without varnish.

Another difference is that, right after the constant thickness zone, the thickness loss is much more abrupt than for the case of the 4C+DEA. This can be easily understood from the TGA performed to the Varnish 1 previously presented (5.4(a)), where a 60% of the mass is decomposed around 200°C.

On the other hand, the film thickness loss for the films deposited with varnish is smoothed after 250°C, and from 320°C (where the 4C+DEA film is fully compacted) there is still a great thickness reduction.

This fact justifies that the film cracking is displaced to higher temperatures, since the remaining varnish can hold the film structure, smoothing the film collapsing. This agrees with the requirements established for the additives in order to prevent a large stress contribution.

The comparison of the mass decomposition of the 4C+DEA and the 4G+V1 (figure 5.17 (b)) shows the difference of the mass lost due to the varnish addition, which justifies the initial thickness increase. However, the mass loss curve is really similar for both tested inks.

Comparing the mass with thickness we observe that at low pyrolysis temperatures the mass is rapidly decomposed while thickness remains constant. This implies that compressive stress affecting the film, which could be deduced from the buckling formation.

From this study we can conclude that:

- The different pyrolysis zones described during chapter 4 are maintained when the varnish is added.
- The varnish addition leads to an initial film thickness increase of a factor

2. This will lead to a high stress contribution, thus, to decrease this thickness addition by tuning the varnish composition could lead to the film thickness enhancement.
- A part of the varnish decomposes after the TFA decomposition, smoothing the film collapsing. This agrees with the additives requirements described before.

5.6.3 In-situ mechanical properties study for films deposited with varnish

In the previous chapter, the higher resistance to buckling was justified by a larger viscosity value of the liquid regime measured during pyrolysis. To observe if the films deposited with 4G+V1 also presented this viscous deformation behaviour we measured the mechanical properties by TMA, using the following experimental conditions:

Technique	Heating ramp	Temperature range	Atmosphere
TMA	10°C/min	100-320°C	N ₂

Table 5.12: Thermal analysis experimental conditions table n°3

The 4G 1M + 6.6%_{V/V} V1 was tested on LAO 10x10mm² deposited by inkjet printing with a nominal thickness after growth of 1µm.

From the TMA curves (figure 5.18) we could observe the same liquid regime behaviour already observed on the other inks. The liquid response to the indentation was located between 140 and 290°C, as it was detected for other ink formulations.

The viscosity values obtained from the films with varnish as compared with the previous measured compositions, present higher values at all temperatures. In table 5.13, we display the measured viscosity values for 4C+0.5% DEA, 4G and 4G+6.6% V1 inks, also plotted in figure 5.19.

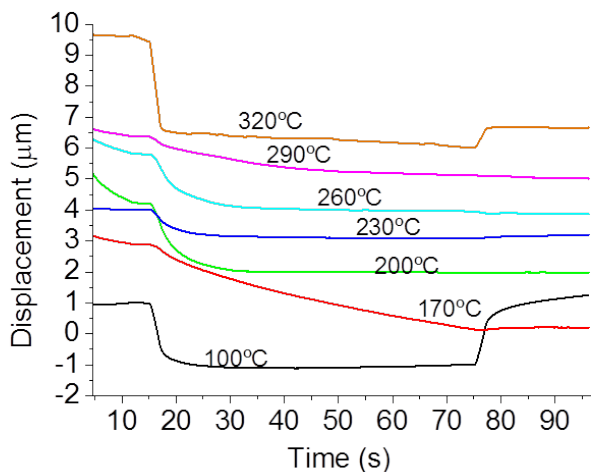


Figure 5.18: Displacement curves obtained from the TMA measures of a film deposited with 4G 1M + 6.6% V/V V1 with a nominal thickness of $1\mu\text{m}$ after growth. All the measurements but the ones performed at 100°C and 320°C presented a liquid behaviour response to load.

What we can also observe from figure 5.18 is that, even if the films deposited with 4G+V1 present higher viscosity values from 140°C to 240°C , at 260°C the viscosity values are really similar for all the solutions. The reason is that at this temperature, the liquid regime is changing to the solid regime, losing the viscous deformation response to load.

If the viscosity values are related with the critical heating rate for each composition, we can conclude that the samples with higher viscosity values present a higher resistance to the film defects formation. This supports the hypothesis that an increase in viscosity complicates the film deformation due to stress.

5.7 Synthesis of thick pyrolyzed films

After analysing the physico-chemical results for the 4G+V1 solution affecting the pyrolysis, we observed important changes respect to the previous used

	Viscosity from TMA measurements (MPa·s)		
	4C+DEA N ₂	4G N ₂	4G+V1 N ₂
140°C	5.6	—	—
170°C	0.6	5.4	—
200°C	0.6	2.5	3.2
230°C	0.7	1.0	2.7
260°C	4.2	4.6	4.6

Table 5.13: Viscosity values measured from the films deposited with the indicated ink composition. The temperatures without a viscosity value presented a too large viscosity to be measured.

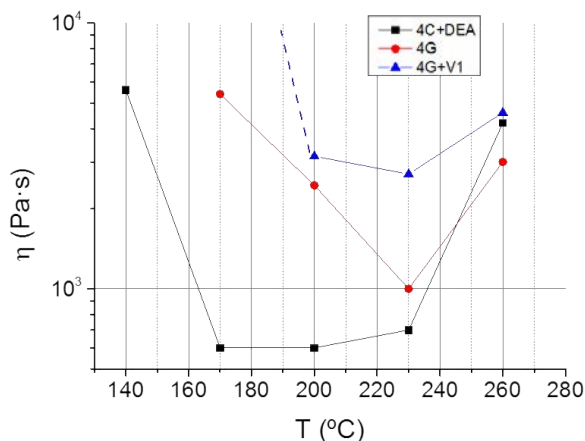


Figure 5.19: Viscosity values obtained for films with 1 μm of nominal thickness after growth deposited with: 4C 0.5M + 0.5%_{V/V} DEA (black); 4G 0.5M (red); 4G 1M + 6.6%_{V/V} V1 (blue).

solutions. Even though, the main stages of the pyrolysis were maintained:

1. We still observe a first stage below 240°C where buckling is formed. Compressive stress is generated due to the mass loss without a film compaction response. The viscosity of the liquid measured by TMA decreases.
2. On the second stage, the film tends to crack due to tensile stress around 300°C. The film is compacted on this temperature zone faster than the

mass is lost, generating a tensile stress. When measured by TMA, we observe the viscosity increase until it becomes a solid after 300°C.

Considering this, we used the heating ramp already optimized for 4C+0.5% DEA to perform a pyrolysis on the tubular furnace. We deposited films with 3 different thickness for the first test, as we indicate in the following table:

	Used solution	Additives	Nominal thickness	Heating rate (°C/min)		
				160°C	240°C	500°C
4	4G 1M	6.6% _{V/V} V1	850nm	25	1	5
5	4G 1M	6.6% _{V/V} V1	950nm	25	1	5
6	4G 1M	6.6% _{V/V} V1	1050nm	25	1	5

Table 5.14: Pyrolysis experimental conditions table n°5

In figure 5.20 we show the optical micrographs of the three samples, with their respective thickness mapping. As it can be observed, the films were really homogeneous, with thickness differences below 10%. The film deposited with a nominal thickness of 850nm after growth, does not present any defect.

The film of 950nm was only cracked around a deposition impurity and did not propagated along the samples.

The thicker film (more than 1 μ m after growth) did crack. The cracks present a superficial aspect, and they are located in the film centre, implying an homogeneous stress distribution.

After these promising results we synthesized multiple samples. Over 50 samples were pyrolyzed with a nominal thickness around 800-1000nm after growth, obtaining a success rate of 80% of films without displaying cracks. Within this statistics analysis, the cracked samples were the ones that presented some liquid inhomogeneities or impurities, such as precipitates or dirt which could not be detected before pyrolyzing the film.

The liquid inhomogeneities sources were the following ones:

- High environmental humidity conditions (>30% of relative humidity).
- Film deposition after a prolonged printing time. For longer printings than

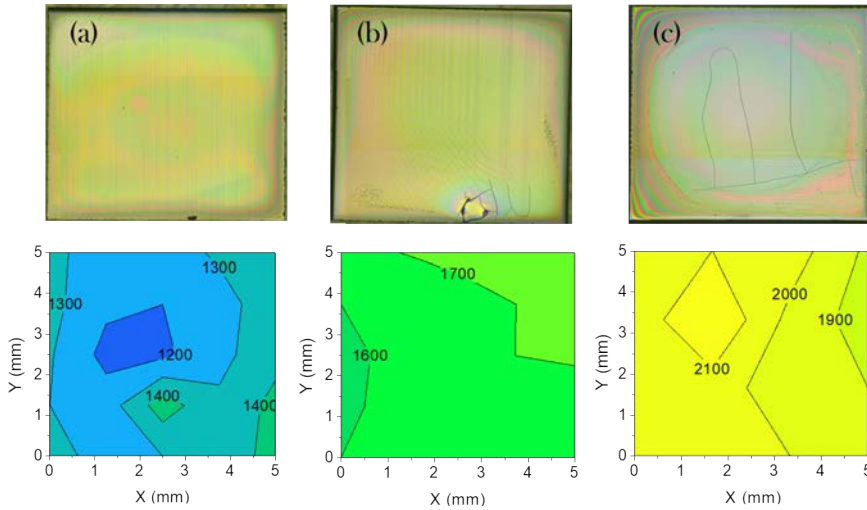


Figure 5.20: Optical microscope images of pyrolyzed films and the respective thickness maps of films deposited with 4G 1M + 6.6%_{V/V} V1 with a nominal thickness after growth of (a) 850nm, (b) 950nm and (c) 1050nm. As can be observed all were really homogeneous and only (c) presented extended cracks.

2 hours, the solution presents signs of deterioration, which produces liquid inhomogeneities or impurities during the curing.

- Unpredicted movements during deposition or on sample positioning below the UV lamp
- Bad solution preparation: light contact during the varnish addition, precursors partial dissolution, high water content of the ink.

5.7.1 Surpassing 1 μ m in one single deposition

To reach the over-micrometer thickness milestone, we repeated the single deposition and pyrolysis for several films using 4G 1M + 6.6%_{V/V} V1 with a nominal thickness above 1 μ m.

Using the same pyrolysis conditions we were able to obtain 2 non-cracked samples out of 10 attempts. In figure 5.21 one of the successful over-micrometer films is displayed.

	Solution	Additives	Nominal thickness	Heating rate ($^{\circ}\text{C}/\text{min}$)		
				160 $^{\circ}\text{C}$	240 $^{\circ}\text{C}$	500 $^{\circ}\text{C}$
7	4G 1M	6.6% $_{V/V}$ V1	1100nm	25	1	5

Table 5.15: Pyrolysis experimental conditions table n°6

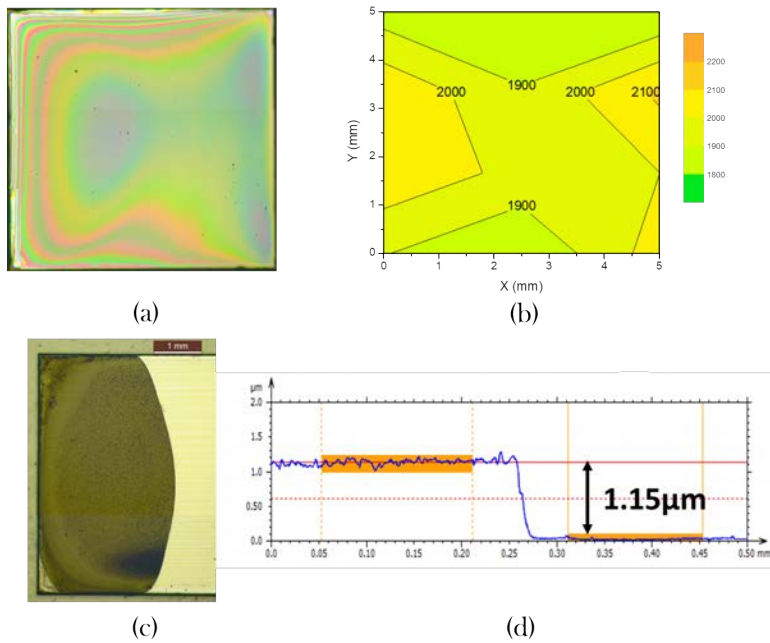


Figure 5.21: Film deposited with 4G 1M + 6.6% $_{V/V}$ V1 with 1140nm after growth in one single deposition. In (a) the optical micrograph of the film is displayed. (b) Thickness mapping of the sample. (c) Optical micrograph of the grown film after performing an etching; the left, brown part is the film, the white right part is the substrate. (d) Profilometry measurement of the grown film.

Even with the low reproducibility, obtaining a fully grown YBCO film with this thickness in one single deposition without cracks has never been reported for the Chemical Solution Deposition route.

Actually there is still further room for improvement on the ink in order to increase the achievable thickness:

1. The varnish-solution proportion and the solution concentration can still be tuned to decrease the extra mass amount at the beginning of the pyrolysis but maintaining the high homogeneity provided by a high varnish proportion.
2. The varnish formulation can be improved to provide more mechanical resistance to the system or to reduce the organic mass contribution to the film.
3. The pyrolysis should then be also optimized.

5.7.2 Thickness increase through multideposition

Due to the high reproducibility, we were able to investigate how to obtain higher thickness by multideposition. Two films were deposited in a 10x10mm² with a nominal thickness of 800nm after growth for each of them. The second deposition is performed on top of the first film after the pyrolysis treatment.

	Solution	Additives	Nominal thickness	Heating rate (°C/min)		
				160°C	240°C	500°C
8	4G 1M	6.6% _{V/V} V1	800nm	25	1	5
9	4G 1M	6.6% _{V/V} V1	800nm (+800nm)	25	1	5

Table 5.16: Pyrolysis experimental conditions table n°7

Neither the first nor the second deposition presented cracking. The optical image of the film was measured by profilometry after growth, obtaining a result of 1600nm. The film and the corresponding measured profile are shown in figure 5.22.

This result demonstrates that very thick films can be obtained through a process requiring only two pyrolysis steps instead of the >10 repetitions which were used up to now for YBCO films with similar thickness [82, 157].

Thus, we can conclude that there is no limit on the thickness achievable regarding the IJP deposition and pyrolysis. With only 3 deposition we can

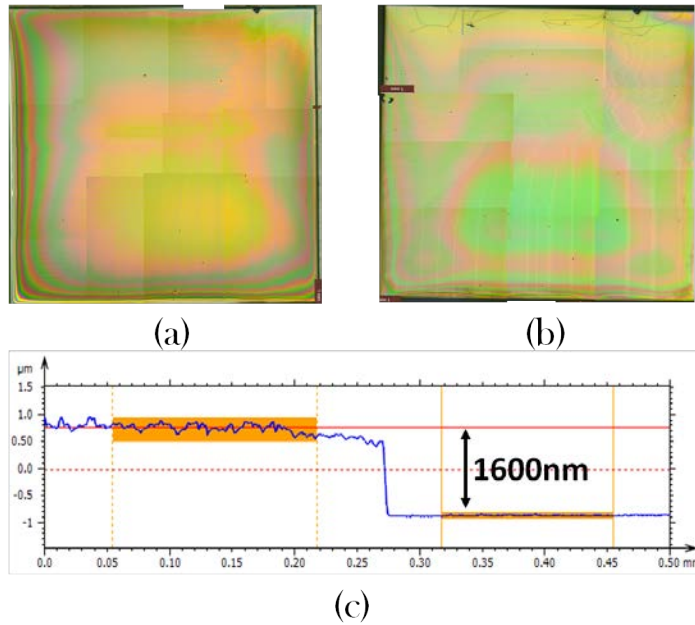


Figure 5.22: Film resulting from the deposition of 2 films deposited with 4G 1M + 6.6% V/V V1 of 800nm after growth. (a) Optical micrograph of the first pyrolyzed film. (b) Optical micrograph of the second pyrolyzed film. (c) Profilometry measure of the film after growth.

achieve a film with a thickness after growth of $3\mu\text{m}$ where many authors would need around 20 steps to achieve the same thickness.

5.7.3 Pyrolyzed film cross section and film compactness

To further characterize the thick film microstructure, we studied the film cross section by Scanning Electron Microscopy (SEM), using Focused Ion Beam (FIB) to ablate the film and analyse a cross section.

The cross section of films deposited with 4G 1M + 6.6% V/V V1 presented a compact structure with any visible pore. This compactness deeply contrasts with the high porosity observed on films deposited by low fluorine without varnish addition as can be observed in figure 5.23.

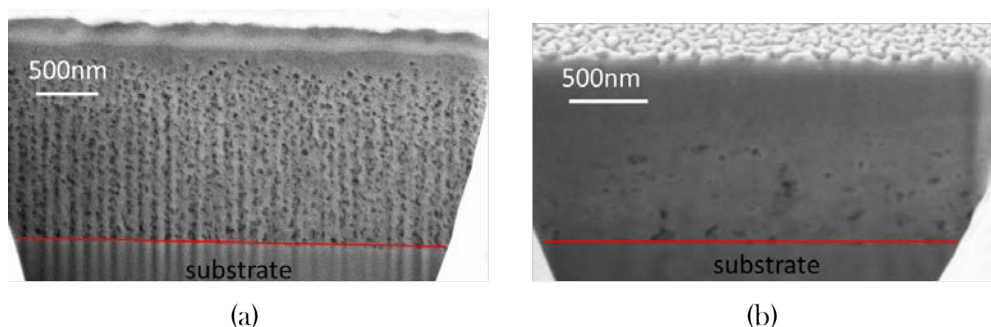


Figure 5.23: SEM image from the cross section of films with a thickness after growth around $1\mu\text{m}$ deposited with (a) 4C 0.5M + 0.5% $_{V/V}$ DEA, with a thickness= $2.3\mu\text{m}$ and (b) 4G 1M + 6.6% $_{V/V}$ V1, thickness= $1.6\mu\text{m}$. The difference in porosity can be clearly observed.

The high film compactness after pyrolysis is an issue of high interest for a proper film growth, not only in YBCO but on other materials, specially piezoelectric material or photovoltaic solar cells, where reducing the film porosity is of fundamental interest to achieve enhanced performances.

From the films deposited with compositions without varnish we observe a film compaction of a factor 2.3 from the pyrolyzed film to the grown YBCO crystal: a film with 2300nm after pyrolysis results in a 1000nm thick film after the growth process. This corresponds to an estimated porosity of $\sim 57\%$.

On the other hand, a film deposited with 4G + Varnish 1 with a thickness of 2000nm after pyrolysis, becomes a grown film of 1140nm (reduction factor 1.75). The corresponding porosity is reduced in this case to a $\sim 40\%$.

This demonstrates the higher compactness achieved by the 4G+V1 solution in comparison with the solution without varnish, indicating the role of the varnish in the film decomposition.

This is a parameter that will be properly considered in the effort being carried out to optimize the growth conditions of these films at SUNAM.

5.7.4 BZO Nanocomposite and Ag addition for an enhanced YBCO performance

Along this work we have presented the addition of some compounds to improve the deposition and pyrolysis performances. But there are also a whole set of additives that are being used to increase the film quality during the high temperature annealing performed to grow epitaxial YBCO films or to enhance the superconducting properties.

Preformed nanoparticles for the nanocomposite film synthesis the additives of silver salts (Ag(TFA)) to tune the growth parameters were used in combination with the 4G+V1 solution. The addition of these compounds did not require any modification of the deposition and pyrolysis processes, demonstrating the ink robustness.

The reasons for the addition of preformed nanoparticles and the silver addition are briefly described in the following sections.

5.7.4.1 Spontaneous segregation route for nanocomposite film synthesis

In the previous chapter we mentioned the interest of adding Ba_2YTaO_6 (BYTO) or BaZrO_3 (BZO) precursors to generate nanoparticles during the growth step.

This processing approach to nanocomposite films is called "spontaneous segregation" nanocomposite because the nanoparticles are segregated and formed from the NPs precursor salts during the growth process of YBCO [32, 66, 158]. One of the limitations of this process is that it is difficult to achieve control on the final nanoparticles composition and size [159].

To go beyond these limitations, the SUMAN group, in collaboration with the Universitat Autònoma de Barcelona, developed a novel methodology called "preformed nanoparticles" nanocomposite. The process consist on the synthesis of preformed nanoparticles, such as BaZrO_3 , BaHfO_3 , ZrO_2 , CeO_2 [160] and its stabilization as a colloidal solution in the organometallic precursor solution

of YBCO.

The nanoparticles are synthesized by the solvothermal method from organometallic precursors and stabilized in methanol or butanol with concentrations rounding the 90mM. The nanoparticles colloidal solution is stable for weeks.

The resulting nanoparticles could be prepared with an average size in the range of 5-10nm, suspended in butanol, making them perfectly suited for implementation in our inks. With these colloidal solutions, we were able to grow nanocomposite films following the preformed nanoparticles route. The advantages of this route are discussed elsewhere [32, 160, 161].

The BZO nanoparticles addition to the solution is performed after the precursors are dissolved and before filling the solution to volume. The colloidal solutions display fairly good stability: the nanoparticles suspended within the ink, for concentrations up to a 50%_{mol}, are stable for several weeks.

5.7.4.2 Silver addition for the modification of growth conditions

Silver is added to the solution as Ag(TFA) (silver trifluoroacetate) in a concentration of 5%_{mol} respect the YBCO.

The purpose of this additive is to decrease the c-axis nucleation temperature of YBCO, increasing the window for the epitaxial nucleation in the thick films [39, 66, 162].

In addition, when YBCO is grown on top of a CeO₂ buffer layer, a competitive reaction of the Ce₂ with the BaF₂ occurs at a similar temperature than the YBCO growth. This reaction leads to the formation of BaCeO₃ layers, strongly degrading the YBCO film texture.

By decreasing the YBCO growth temperature with the silver addition, the formation of BaCeO₃ can be avoided until the YBCO is completely nucleated in c-axis orientation, ensuring that the BaCeO₃ does not affect the YBCO texture [161, 162].

During film annealing, the silver sublimates leaving any trace in the grown material.

The Ag(TFA) salt is added to the solution before the varnish addition, 10

minutes before carrying out the deposition. The solution must be heated up to 50°C to dissolve the Ag(TFA). The stability lifetime of the Ag(TFA) in the ink is about 2-3 hours before observing the first signs of precipitation due to the silver oxidation.

Regarding the scaling up of the process, the precipitation of silver can be easily avoidable by protecting the ink from UV radiation.

5.8 Growth of YBCO films

The promising films obtained from the deposition and pyrolysis of the 4G+V1 ink were grown to form superconducting YBCO films.

Using an optimized growth treatment through silver addition to lower the nucleation temperature [162], we were able to grow YBCO in both LAO and buffered metallic tapes as substrates. In addition, using the colloidal solutions of preformed BZO and BHO nanoparticles, we could synthesize nanocomposites by the colloidal solution route, obtaining superior superconducting performances [161].

Only a weak (103) Bragg peak is observed which corresponds to randomly oriented YBCO grains, while (001) peaks are associated to the epitaxial volume.

5.8.1 Pristine growth of YBCO films on LAO substrates

The growth of pristine YBCO films, using 4G + V1 + Ag(TFA), presented a high quality epitaxy, as can be observed the X-Ray diffraction pattern presented in figure 5.24, which corresponds to a 2D $\theta - 2\theta$ X-Ray diffraction of a 1000nm thick film.

The superconducting properties were measured by SQUID for 600nm and 1000nm pristine films. For the 600nm film we obtained 2.7MA/cm² of critical current density (J_C) at self field (SF) and 77K and a critical temperature (T_C) of 90.7K.

The 1000nm film presented a $J_C=1.9\text{MA}/\text{cm}^2$, which corresponds to an I_C of 190A/cm·w.

All the results are displayed in figure 5.27.

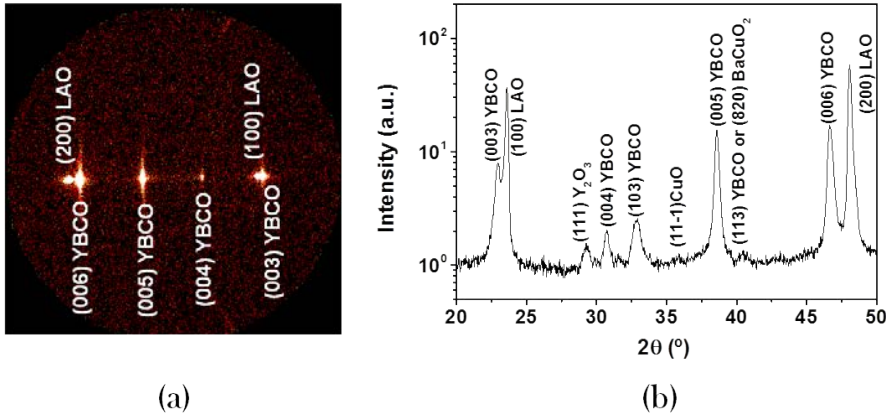


Figure 5.24: X-ray diffraction results from a pristine 1000nm thick film deposited with 4G 1M + 6.6%_{V/V} V1. (a) 2D X-ray diffraction pattern where the discrete spots confirm the film epitaxy. (b) Integrated diffraction pattern showing only the (00l) YBCO reflections (besides the LAO substrate reflections), and a weak (103) peak corresponding to randomly oriented YBCO grains.

These results surpass in both J_C and I_C the values obtained in the previous chapter ($J_C = 1.73\text{MA}/\text{cm}^2$ for a 950nm film deposited with 4C + 0.5%_{V/V} DEA). But most importantly, unlike the films deposited without varnish, these films can be obtained with a high reproducibility.

5.8.2 YBCO-BZO nanocomposite YBCO on LAO substrates

However, in order to increase the superconducting performance at high magnetic fields, we grew nanocomposite films, with the incorporation of preformed BZO nanoparticles to the YBCO matrix.

Nanocomposite YBCO films were grown using the most successful thick film approach, using the ink designed for this work:

- 4G 1M + 6.6%_{V/V} V1 + 12-20%_{mol} BZO + 5%_{mol} Ag(TFA).

From the pyrolyzed films deposited with this ink composition, we grew epitaxial films with a randomly oriented homogeneous distribution of BZO

nanoparticles. In figure 5.25 the X-ray diffraction pattern obtained for a 850nm thick film deposited with the mentioned ink shows the achieved YBCO epitaxy, though some minor phases of $Y_2Cu_2O_5$ are still observed.

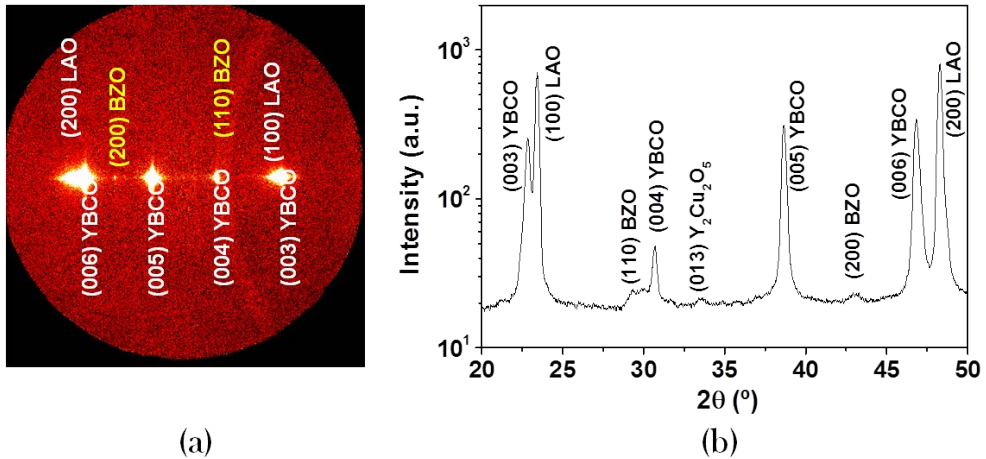


Figure 5.25: X-ray diffraction results from a nanocomposite 850nm thick film deposited with the 4G 1M + 6.6% $_{V/V}$ V1 12% $_{mol}$ BZO + 5% $_{mol}$ Ag(TFA) ink. (a) 2D X-ray diffraction pattern where the discrete spots confirm the film epitaxy. The ring at the BZO reflection indicates the presence of randomly oriented nanoparticles. (b) Integrated diffraction pattern showing only the (00l) YBCO and the (110) and (200) BZO reflections. Some minor phases of Y_2O_3 and CuO are also seen.

In figure 5.26 we show a micrograph obtained from the Transmission Electronic Microscopy (TEM) analysis of the cross section of a YBCO + 12% $_{mol}$ BZO NPs film. In this image it can be observed the homogeneous nanoparticles distribution in the YBCO matrix of a thick film.

The superconducting properties of the YBCO film were determine by SQUID magnetometry. For films deposited with a 12% $_{mol}$ BZO we obtained J_C values at 77K and self-field in the range of 3MA/cm 2 for films with a measured thickness between 700 and 1000nm. In figure 5.27(a) we show that a 850nm film displays a I_C value of ~ 240 A/cm \cdot w ($J_C = 2.8$ MA/cm 2) at 77K SF.

With this ink composition we obtained the highest current values achieved

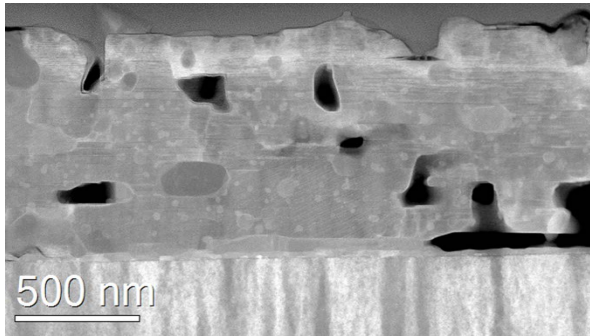


Figure 5.26: TEM image of the cross section of a YBCO film with 12% $_{mol}$ BZO NPs. The NPs present an homogeneous size and distribution within the YBCO matrix.

so far by IJP in films prepared with a reproducible and robust methodology.

In addition, the BZO nanoparticles enhance the critical current at high magnetic fields, as it can be observed in figure 5.27(b), where we compare the critical current dependence with magnetic field.

This dependence was determined by transport measurements for a nanocomposite 700nm film with 20% $_{mol}$ BZO and a 850nm film with 12% $_{mol}$ BZO, both of them using an initial precursor solution with the ink 4G 1M + 6.6% $_{V/V}$ V1 and 5% $_{mol}$ of Ag(TFA).

In figure 5.27(b) we compare the I_C - magnetic field dependence of the described nanocomposite thick films with a 250nm pristine YBCO sample deposited with a 4C 1.5M ink by spin coating, and a pristine YBCO 600nm film deposited using the ink 4G 1M + 6.6% $_{V/V}$ V1 + 5% $_{mol}$ by inkjet printing.

From the results, we can observe that the nanocomposite films present a much slower I_C decay when the magnetic field increases respect the pristine samples. In addition, it can be observed the high I_C enhancement when the film thickness increases.

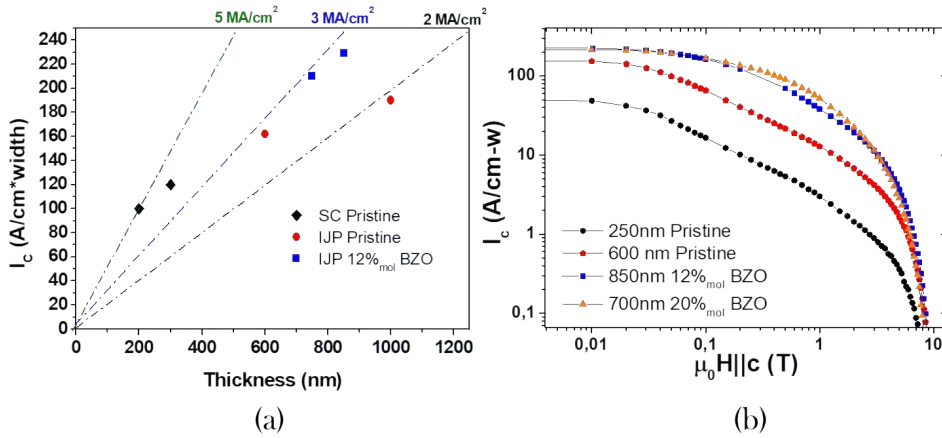
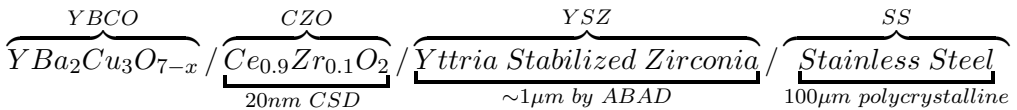


Figure 5.27: Critical current (I_C) values comparison for YBCO films deposited by inkjet printing (IJP) and spin coating (SC). We compare films deposited by spin coating (black), and by inkjet printing using pristine precursor inks (red), 12%_{mol} BZO nanocomposite (blue) and 20%_{mol} BZO precursor inks. In (a) we compare the I_C for different thickness and composition at 77K SF. In (b) we show the I_C dependence with magnetic field (parallel to c) of different films at 77K.

5.8.3 Growth of IJP YBCO thick films on metallic buffered tapes

As we have demonstrated we are able to obtain pyrolyzed films with thickness up to $1.7\mu\text{m}$ on top of buffered metallic tapes which gives around 1000nm thick films after growth. These films could be grown on metallic substrates to form a coated conductor architecture. From top to bottom, the investigated architecture is the following:



We successfully grew a $1\mu\text{m}$ YBCO film on top of the buffered Bruker tape obtaining essentially an epitaxial structure, with only a small intensity of (103) Bragg peak, corresponding to a random orientation, as can be observed in figure

5.28.

These films presented I_C values in the range of 100A/cm·w at 77K, self field, when we use the ink 4G 0.1M + 6.6%_{V/V} V1 + 12%_{mol} BZO + 5%_{mol} Ag(TFA). These results demonstrate the suitability of this ink composition to obtain high performance superconducting coated conductors.

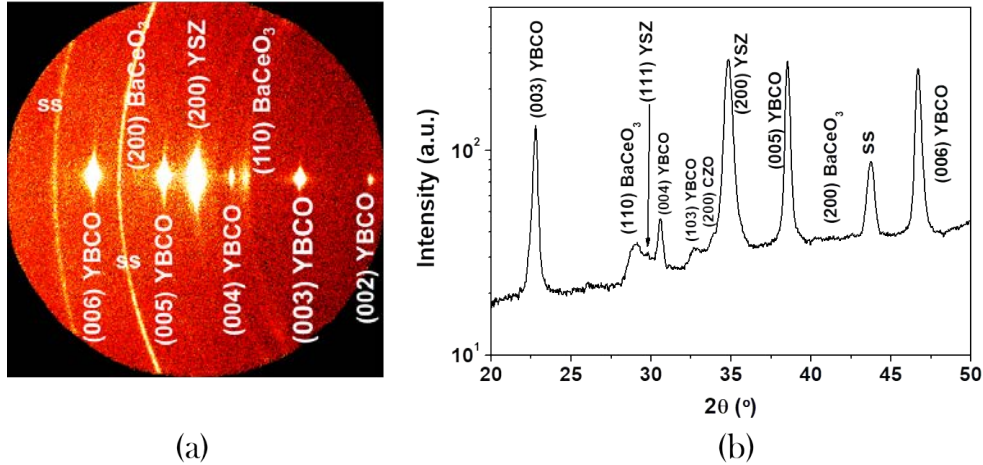


Figure 5.28: X-ray diffraction pattern of a coated conductor deposited with 4G 0.1M + 6.6%_{V/V} V1 + 12%_{mol} BZO + 5%_{mol} Ag(TFA). (a) 2D X-ray diffraction pattern where the YBCO epitaxy can be appreciated. (b) Integrated X-ray diffraction pattern where only a small intensity of the (103) peak associated to randomly oriented YBCO grains is detected. It can be noticed that Ba reacted with CeO₂ giving rise to BaCeO₃.

5.9 Chapter summary and conclusions

In this chapter we used the knowledge generated in the two previous chapters, to obtain the highest single deposited YBCO thick film reported until now in a highly reproducible process. In this section we will describe the conclusions reached from the analyses performed within this chapter.

- We discarded the viscosity enhancement by the addition of polymers as a valid approximation to obtain an homogeneous liquid distribution. The viscosity was increased through the PEG_{8000/20000} addition.

- From a collaboration with the company Chimigraf (KAO corporation) we obtained an UV curable varnish (V1) that we adopted for inkjet printing deposition. The purpose of the varnish addition was to avoid the liquid movement due to solvent evaporation and further induce the film polymerization by UV-LED curing.

Already during the deposition, the varnish addition to 4G 0.5M ink composition with a 10%_{V/V} content displayed an excellent film homogeneity. The homogeneity enhancement is produced by two factors:

- A stronger liquid-substrate interaction. This was observed from the drop merging study, where, unlike the 4G ink without varnish, the printed lines were not dragged towards the neighbour lines.
 - The low varnish volatility, slowed the film drying, avoiding the problems produced from the solvent evaporation.
- Despite the high homogeneity displayed by the 4G 0.5M with a 10% of varnish, the large added amount resulted in film heavy cracking due to the high increase of organic matter to be decomposed. The ink was modified by increasing the salt concentration to 1M and reducing the varnish addition to 6.6%_{V/V}, maintaining on this way a good liquid distribution homogeneity while avoiding film cracks.
 - To avoid the liquid movement in the Y direction, the drop pitch was changed, using larger drop distances in the Y axis to reduce the drop overlapping in this direction. This resulted in an enhanced liquid distribution homogeneity.
 - The varnish could be successfully polymerized with light with a wavelength of 295nm. A smooth curing was required to avoid the liquid movement since the 4G ink absorbs the UV light in the same wavelength emitted by the LED used to fix the sample, and thus, a too intense UV light can heat up the film leading to liquid inhomogeneities.
 - The morphology analysis with the pyrolyzer showed that the buckling was also produced at 180°C at low heating rates (2°C/min), but it was

reversed even at $20^{\circ}\text{C}/\text{min}$. the mechanical analysis showed a higher viscosity for the films deposited with varnish, confirming the hypothesis that higher viscosity values during pyrolysis led to an enhanced resistance to permanent buckling formation.

On the other hand, the crack formation was shifted to 300°C .

With the analysis of the mass and thickness evolution for films deposited with $4\text{G } 1\text{M} + 6.6\%_{\text{V/V}} \text{V1}$ we found that part of the varnish decomposed at higher temperatures than the TFA decomposition (we recall that the decomposition of the TFA triggered the film collapsing at $260\text{-}280^{\circ}\text{C}$).

From the in-situ analysis on the thickness evolution, we observed that this non-decomposed part is able to hold the film structure.

Thus, the varnish meets the requirements, postulated during the previous chapter, to avoid the crack formation during the pyrolysis process:

- It forms a polymeric network capable to hold the film structure
- Part of the decomposition of the varnish occurs at higher temperature than the TFA decomposition (where the film collapses if there is no additive), and hence, the film shrinkage is smoother.
- If it is added in a $6.6\%_{\text{V/V}}$, the varnish does not increase too much the organic mass. This avoids an excessive stress generation.

The ramps optimized for the 4C solution were perfectly suited for the pyrolysis of 4G + V1 solution, although faster heating ramps could be used due to the high resistance to permanent buckling and crack formation showed by the films deposited with varnish.

- With all the knowledge generated through this thesis, we could obtain the thickest YBCO films up to now, deposited in one single coating by CSD (1150nm after growth). We could achieve up to 80% of reproducibility on film synthesis around $1\mu\text{m}$ thick for both LAO and metallic substrates.

We also demonstrated that $1.6\mu\text{m}$ thick films after growth could be achieved in just two coatings due to the high reproducibility of the process.

- We also demonstrated the suitability of preparing nanocomposite films with preformed BZO nanoparticles. Furthermore, with the addition of silver in the form of Ag(TFA) on the ink, highly epitaxial films were achieved for $1\mu\text{m}$. The possibility of adding these compounds to the ink demonstrates the robustness of the composition.

The addition of BZO NPs and silver resulted in films and coated conductors with very high superconducting performances for $1.15\mu\text{m}$ thick YBCO films on both LAO ($I_C=240\text{A}/\text{cm}\cdot\text{w}$ at 77K, SF) and buffered metallic substrates ($I_C=100\text{A}/\text{cm}\cdot\text{w}$ at 77K, SF). Excellent J_C – H dependences were also demonstrated in these films.

Conclusions

This thesis has been devoted to the study and optimization of inks, the deposition and the pyrolysis processes for the synthesis of thick YBCO film using the CSD and IJP methodology.

We could design inkjet printing adapted inks using low fluorine YBCO organometallic precursors. Tuning the parameters of the piezoelectric actuator waveform, we achieved stable and reproducible drops.

In order to avoid liquid distribution inhomogeneities during deposition, low volatility solvents (b.p. $> 100^{\circ}\text{C}$) were required.

Since the main source of liquid distribution inhomogeneities is the capillary flow produced during solvent evaporation, the film curing using a UV polymerizable varnish was proposed. The approach consisted of avoiding the liquid movement by generating a polymeric network to fix the film.

Using this approach, we designed an ink with the following characteristics:

80%_{V/V} butanol, 20%_{V/V} propionic acid + 6.6%_{V/V} varnish (V1);
salts concentration = 1M (0.167M Y(TFA)₃ + 0.33M Ba(AcO)₂ + 0.5M Cu(AcO)₂).

With this composition, and by decreasing the drop overlapping in the Y direction to maximize the drop-substrate contact in this direction, we could achieve liquid distribution differences in thickness below 20%, which we considered a very homogeneous film.

This ink composition was designed not only to obtain an optimal deposition, but also to avoid film buckling and cracking during the pyrolysis process.

With an thorough physico-chemical study of the pyrolysis process, most of it carried out by in-situ analytical techniques, we obtained a clear picture of

this CSD stage.

We defined the pyrolysis in 3 thermal zones:

1. From room temperature to 180°C any change can be observed on the film.
2. From 180°C to 240°C we observed film buckling attributed to a compressive stress caused by a density loss: a 50% of the organic mass, all the propionates, was lost while the film thickness remained almost constant; buckling could be reversed if the heating rate was kept below a critical value.

From a novel technique to study the mechanical properties during the pyrolysis, we observed that the buckling formation and reversion were possible due to the liquid-like behaviour of the films during the pyrolysis process.

3. Above 240°C, we observe film cracking due to the huge film shrinkage detected with the in-situ thickness study. Correlating the mass and thickness study, we observed that the film shrinkage is triggered by the TFA decomposition, which acts as the film skeleton. DEA and Varnish can also hold the film structure, avoiding that all the collapsing occurs with the TFA decomposition and thus smoothing the film collapsing.

From these studies we concluded that to enhance the mechanical properties, compounds with the following characteristics should be added:

- The additives should be able to generate chemical networks (e.g. chelating agents such as diethanolamine)
- The additive should decompose at higher temperatures than the TFA ligand
- The additive should not increase too much the organic mass

After the physico-chemical analysis we could design an optimal thermal profile and an ink composition to obtain thick, defect-free films in one single coating. With the 4G 1M + 6.6%_{V/V} V1 ink we could achieve a YBCO with a film thickness of 1μm after growth, in a highly reproducible process for a single

coating. The process could be demonstrated on both LaAlO_3 and buffered metallic substrates.

We could even surpass the $1\mu\text{m}$ barrier, achieving a film thickness of 1150nm after growth, the thickest YBCO film accomplished until now in one single coating and one of the thickest coatings ever achieved for films synthesized following the CSD methodology in other materials.

The knowledge of how to prepare thick homogeneous films by IJP has been now efficiently transferred to the spin-off company of SUNAM (OXOLUTIA), where a continuous reel-to-reel is used to scale-up the process for industrial use.

Finally, the growth of the thick pyrolyzed films was optimized by our group experts on the topic. It was demonstrated that our films could lead to high quality thick films, with excellent superconducting performances, achieving at 77K and self field, a $I_C=240\text{A}/\text{cm}\cdot\text{w}$ on LAO single crystals and a $I_C=100\text{A}/\text{cm}\cdot\text{w}$ on metallic substrates following the coated conductor architecture.

In this last figure 6.1, we display the different goals achieved during this thesis, regarding the film thickness, homogeneity and superconducting properties once they are grown.

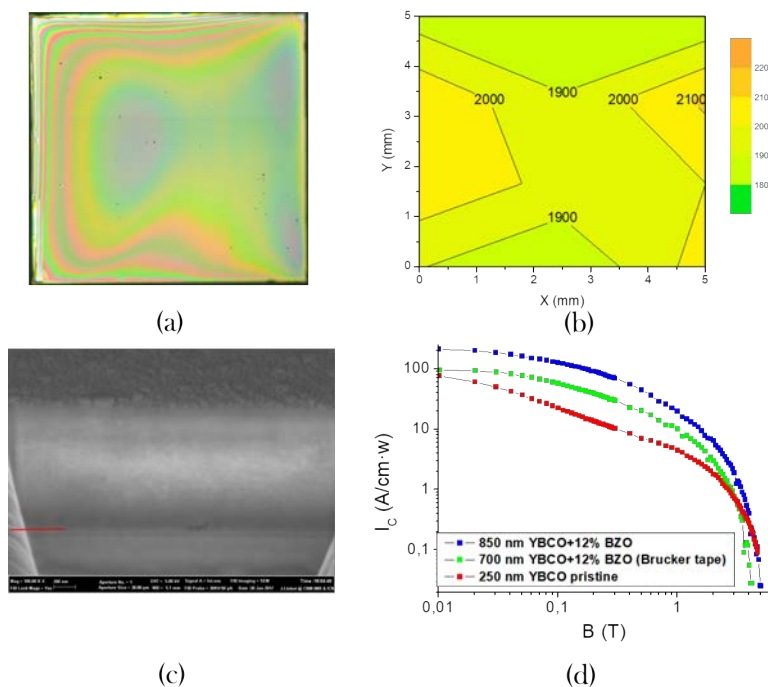


Figure 6.1: This figure summarizes the achievements accomplished on the thick YBCO films on one single coating. (a) Optical image were a 1150nm thick film after growth shows no signs of cracks nor buckling. (b) Thickness mapping of the film displayed in (a), were the thickness homogeneity can be observed. (c) Cross section analysed by SEM-FIB of a pyrolyzed thick film, showing a compact and homogeneous morphology. (d) High superconducting properties displayed by thick nanocomposite films on LAO (blue) and metallic (green) substrates compared with a thin pristine film (red).

Appendix

A.1 Calculations for the TGA theoretical final mass

From the predicted final products mass, we calculated the theoretical mass at the end of the pyrolysis.

For a LF solution 1.5M, assuming only copper and barium propionates, and yttrium trifluoroacetate for a 1.5M concentration, the initial mass after drying will be:

$$Y(CF_3COO)_3 \text{ MW} : 427.95g/mol * 0.25 = 106.98g$$

$$Ba(C_2H_5COO)_2 \text{ MW} : 283.5g/mol * 0.50 = 141.734g$$

$$Cu(C_2H_5COO)_2 \text{ MW} : 209.7g/mol * 0.75 = 157.265g$$

If the final product correspond to YBCO, then the final mass will be:

For 1L solution :

$$\frac{0.25M(YBCO)}{0.25M(Y(TFA)_3) + 0.5M(Ba(prop)_2) + 0.75M(Cu(prop)_2)} = \quad (A.1)$$

$$= \frac{166.55}{406.00} * 100 = 41.02\%$$

If the final product is considered as CuO (MW=79.55g/mol, stoichiometry 1:3 respect Y) and Ba₂YF₇ (MW=496.55g/mol, stoichiometry 1:1 to Y) as the XRD shows, then:

$$\frac{0.75M(CuO) + 0.25M(BYF)}{0.25M(Y(TFA)_3) + 0.5M(Ba(prop)_2) + 0.75M(Cu(prop)_2)} =$$

$$= \frac{183.80}{406.00} * 100 = 45.27\%$$
(A.2)

A.1.1 IR mass determination

A.2 TMA viscosity measurement

Here we describe how the viscosity curves obtained from the thermomechanical analysis were measured.

The calculations are based on the Stoke's equation

Theoretical TMA curve Under several reasonable simplifications of the hydrodynamic problem, one arrives to the following formula relating the velocity of the probe to the experimental conditions and the viscosity of the film:

$$\nu = \frac{F}{6\pi\eta R^2} \frac{(2H - h_0)^2 h_0}{4(H - h_0)^2}$$
(A.3)

where F is the applied load; η , viscosity; H , the film thickness; h_0 , the probe-substrate distance and R the radius of the hemispherical probe end (see figure A.1).

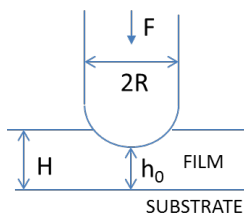


Figure A.1: Geometry of the system

The measured TMA curve is, in fact, the displacement vs time. So to obtain η from these experiments one has to integrate equation A.3 ($\nu \equiv -dh_0/dt$):

$$t = \alpha \left\{ \frac{2}{2 - \frac{h_0}{H} - 2 + \ln[(2 - \frac{h_0}{H})^3 \frac{h_0}{H}]} \right\} \quad (\text{A.4})$$

where:

$$\alpha = \left(\frac{6\pi R^2}{F} \right) \quad (\text{A.5})$$

is a time scale. Notice that when time is normalized to α and h_0 to the film thickness:

$$\tau \equiv \frac{t}{\alpha}; \quad \delta \equiv \frac{h_0}{H} \quad (\text{A.6})$$

the resulting curve has a universal shape:

$$\tau = - \left\{ \frac{2}{2 - \delta} - 2 + \ln[(2 - \delta)^3 \delta] \right\} \quad (\text{A.7})$$

Fitting procedure of the TMA curves Fitting of the experimental curves can be achieved by simply changing the time and displacement scales until the theoretical and experimental curves overlap. In the example of figure A.2, α is the ratio between Δt and $\Delta \tau$, whereas $\delta = 1$ at the point where the probe enters in contact with the film upper surface and $\delta = 0$ when it coincides with the asymptotic value of the displacement.

From the value of α one obtains the viscosity:

$$\eta = \frac{F}{6\pi R^2 \alpha} \quad (\text{A.8})$$

If the film thickness is unknown, as will be the usual case for intermediate temperatures, it is not easy to know exactly when $\delta = 1$ ($h_0 = H$) because of the inertial displacement of the probe in contact with the film before the load is applied (see segment at load = 0 in figure A.2). The decision about the actual value of H is taken by looking at the fitting goodness when H is varied and at the deceleration of the probe seen at the beginning of the region of zero load.

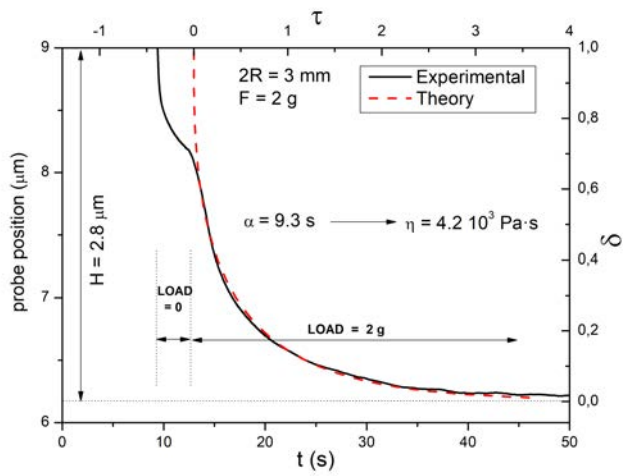


Figure A.2: Fitting of a TMA curve.

Bibliography

- [1] J. R. Waldram. *Superconductivity of metals and cuprates*. CRC Press, 2017.
- [2] H. Rogalla and P. H. Kes. *100 years of superconductivity*. Taylor & Francis, 2011.
- [3] A. L. Solov'ev and R. V. Vovk. On the 30th anniversary of the discovery of high-temperature superconductivity. *Low Temperature Physics*, 42(10):837–839, 2016.
- [4] Y. Shiohara, T. Taneda, and M. Yoshizumi. Overview of materials and power applications of coated conductors project. *Japanese Journal of Applied Physics*, 51(1R):010007, 2011.
- [5] A. Gurevich. To use or not to use cool superconductors? *Nature materials*, 10(4):255, 2011.
- [6] Xavier Obradors and Teresa Puig. Coated conductors for power applications: Materials challenges. *Superconductor Science and Technology*, 27(4):044003, 2014.
- [7] D. Larbalestier, A. Gurevich, D. M. Feldmann, and A. Polyanskii. High- T_c superconducting materials for electric power applications. In *Materials For Sustainable Energy: A Collection of Peer-Reviewed Research and Review Articles from Nature Publishing Group*, pages 311–320. World Scientific, 2011.
- [8] J. L. MacManus-Driscoll, S. R. Foltyn, Q. X. Jia, H. Wang, A. Serquis, L. Civale, B. Maiorov, M. E. Hawley, M. P. Maley, and D. E. Peterson. Strongly enhanced current densities in superconducting coated conductors of $\text{YBa}_2\text{Cu}_3\text{O}_{7-x} + \text{BaZrO}_3$. *Nature materials*, 3(7):439, 2004.
- [9] S. Kang and *others*. High-performance high- T_c superconducting wires. *Science*, 311(5769):1911–1914, 2006.

- [10] J. D. Jorgensen and *others*. Oxygen ordering and the orthorhombic-to-tetragonal phase transition in $\text{YBa}_2\text{Cu}_3\text{O}_{7-x}$. *Physical Review B*, 36(7):3608, 1987.
- [11] D. Dimos, P. Chaudhari, J. Mannhart, and F. K. LeGoues. Orientation Dependence of Grain-Boundary Critical Currents in $\text{YBa}_2\text{Cu}_3\text{O}_{7-\delta}$ Bicrystals. *Physical Review Letters*, 61(2):219, 1988.
- [12] N. F. Heinig, R. D. Redwing, I. Tsu, A. Gurevich, J. E. Nordman, S. E. Babcock, and D. C. Larbalestier. Evidence for channel conduction in low misorientation angle [001] tilt $\text{YBa}_2\text{Cu}_3\text{O}_{7-x}$ bicrystal films. *Applied physics letters*, 69(4):577–579, 1996.
- [13] Y. Iijima, N. Tanabe, O. Kohno, and Y. Ikeno. In-plane aligned $\text{YBa}_2\text{Cu}_3\text{O}_{7-x}$ thin films deposited on polycrystalline metallic substrates. *Applied Physics Letters*, 60(6):769–771, 1992.
- [14] D. P. Norton, A. Goyal, J. D. Budai, D. K. Christen, Donald M Kroeger, Eliot D Specht, Qing He, Bernd Saffian, M Paranthaman, Charles E Klabunde, et al. Epitaxial $\text{YBa}_2\text{Cu}_3\text{O}_7$ on biaxially textured nickel (001): An approach to superconducting tapes with high critical current density. *Science*, 274(5288):755–757, 1996.
- [15] K. Hasegawa, K. Fujino, H. Mukai, M. Konishi, K. Hayashi, K. Sato, S. Honjo, Y. Sato, H. Ishii, and Y. Iwata. Biaxially aligned YBCO film tapes fabricated by all pulsed laser deposition. *Applied Superconductivity*, 4(10-11):487–493, 1996.
- [16] M. W. Rupich, U. Schoop, D. T. Verebelyi, C. Thieme, W. Zhang, X. Li, T. Kodenkandath, N. Nguyen, E. Siegal, D. Buczek, and *others*. YBCO coated conductors by an MOD/RABiTS/spl trade/process. *IEEE transactions on applied superconductivity*, 13(2):2458–2461, 2003.
- [17] J. L. MacManus-Driscoll. Recent developments in conductor processing of high irreversibility field superconductors. *Annual review of materials science*, 28(1):421–462, 1998.

- [18] Y. Iijima, K. Kakimoto, Y. Yamada, T. Izumi, T. Saitoh, and Y. Shiohara. Research and development of biaxially textured IBAD-GZO templates for coated superconductors. *MRS bulletin*, 29(8):564–571, 2004.
- [19] A. Goyal, M. P. Paranthaman, and U. Schoop. The RABiTS approach: Using rolling-assisted biaxially textured substrates for high-performance YBCO superconductors. *MRS bulletin*, 29(8):552–561, 2004.
- [20] D. Dimos, P. Chaudhari, and J. Mannhart. Superconducting transport properties of grain boundaries in $\text{YBa}_2\text{Cu}_3\text{O}_{7-x}$ bicrystals. *Physical Review B*, 41(7):4038, 1990.
- [21] M. W. Rupich and *others*. Advances in second generation high temperature superconducting wire manufacturing and R&D at American Superconductor Corporation. *Superconductor Science and Technology*, 23(1), 2010.
- [22] A. P. Malozemoff. Second-generation high-temperature superconductor wires for the electric power grid. *Annual review of materials research*, 42:373–397, 2012.
- [23] D. P. Norton and *others*. Epitaxial $\text{YBa}_2\text{Cu}_3\text{O}_7$ on biaxially textured nickel (001): An approach to superconducting tapes with high critical current density. *Science*, 274(5288):755–757, 1996.
- [24] J. C. Nie, H. Yamasaki, and Y. Mawatari. Self-assembled growth of CeO_2 nanostructures on sapphire. *Physical Review B*, 70(19):195421, 2004.
- [25] W. Prusseit, R. Nemetschek, C. Hoffmann, G. Sigl, A. Lümke, and H. Kinder. ISD process development for coated conductors. *Physica C: Superconductivity and its applications*, 426:866–871, 2005.
- [26] A. Usoskin and H. C. Freyhardt. YBCO-coated conductors manufactured by high-rate pulsed laser deposition. *MRS bulletin*, 29(8):583–589, 2004.
- [27] X. Palmer, C. Pop, H. Eloussifi, B. Villarejo, P. Roura, J. Farjas, A. Calleja, A. Palau, X. Obradors, T. Puig, and S. Ricart. Solution design for low-fluorine trifluoroacetate route to $\text{YBa}_2\text{Cu}_3\text{O}_7$ films. *Superconductor Science and Technology*, 29(2), 2015.

- [28] M. Biswas and P. Su. Chemical Solution Deposition Technique of Thin-Film Ceramic Electrolytes for Solid Oxide Fuel Cells. In Nikolay N. Nikitenkov, editor, *Modern Technologies for Creating the Thin-film Systems and Coatings*, chapter 16. InTech, Rijeka, mar 2017.
- [29] W. Dong, Y. Guo, B. Guo, H. Liu, H. Li, and H. Liu. Enhanced photovoltaic properties in polycrystalline BiFeO₃ thin films with rhombohedral perovskite structure deposited on fluorine doped tin oxide substrates. *Materials Letters*, 88:140–142, 2012.
- [30] H. Kueppers, T. Leuerer, U. Schnakenberg, W. Mokwa, M. Hoffmann, T. Schneller, U. Boettger, and R. Waser. PZT thin films for piezoelectric microactuator applications. *Sensors and Actuators A: Physical*, 97:680–684, 2002.
- [31] J. Gutiérrez, A. Llordés, J. Gázquez, M. Gibert, N. Romà, S. Ricart, A. Pomar, F. Sandiumenge, N. Mestres, T. Puig, and X. Obradors. Strong isotropic flux pinning in solution-derived YBa₂Cu₃O_{7-x} nanocomposite superconductor films. *Nature Materials*, 6(5):367–373, 2007.
- [32] X. Obradors, T. Puig, Z. Li, C. Pop, B. Mundet, N. Chamorro, F. Vallés, M. Coll, S. Ricart, B. Vallejo, F. Pino, A. Palau, J. Gázquez, J. Ros, and A. Usoskin. Epitaxial YBa₂Cu₃O_{7-x} nanocomposite films and coated conductors from BaMO₃ (M = Zr, Hf) colloidal solutions. *Superconductor Science and Technology*, 31(4):044001, 2018.
- [33] J. L. MacManus-Driscoll, P. Zerrer, H. Wang, H. Yang, J. Yoon, A. Fouchet, R. Yu, M. G. Blamire, and Q. Jia. Strain control and spontaneous phase ordering in vertical nanocomposite heteroepitaxial thin films. *Nature materials*, 7(4):314, 2008.
- [34] K. Matsumoto and P. Mele. Artificial pinning center technology to enhance vortex pinning in YBCO coated conductors. *Superconductor Science and Technology*, 23(1):014001, 2009.
- [35] A. Gupta, R. Jagannathan, E. I. Cooper, E. A. Giess, J. I. Landman, and B. W. Hussey. Superconducting oxide films with high transition temperature prepared from metal trifluoroacetate precursors. *Applied Physics Letters*, 52(24):2077–2079, 1988.

- [36] M. W. Rupich, D. T. Verebelyi, W. Zhang, T. Kodenkandath, and X. Li. Metalorganic deposition of YBCO films for second-generation high-temperature superconductor wires. *MRS bulletin*, 29(8):572–578, 2004.
- [37] X. Obradors, T. Puig, and *others*. Progress towards all-chemical superconducting YBa₂Cu₃O_{7-x} coated conductors. *Superconductor Science and Technology*, 19(3), 2006.
- [38] M. Coll, J. Gàzquez, R. Huhne, B. Holzapfel, Y. Morilla, J. García-López, a. Pomar, F. Sandiumenge, T. Puig, and X. Obradors. All chemical YBa₂Cu₃O₇ superconducting multilayers: Critical role of CeO₂ cap layer flatness. *Journal of Materials Research*, 24(04):1446–1455, 2009.
- [39] X. Obradors, F. Martínez-julián, K. Zalamova, V. R. Vlad, A. Pomar, A. Llordés, and H. Chen. Nucleation and mesostrain influence on percolating critical currents of solution derived YBa₂Cu₃O₇ superconducting thin films. *Physica C*, 482:58–67 Contents, 2012.
- [40] W. Wu, F. Feng, Y. Zhao, X. Tang, Y. Xue, K. Shi, R. Huang, T. Qu, X. Wang, Z. Han, and J. C. Grivel. A low-fluorine solution with a 2:1 F/Ba mole ratio for the fabrication of YBCO films. *Superconductor Science and Technology*, 27(5), 2014.
- [41] C. Apetrii, H. Schlorb, M. Falter, I. Lampe, L. Schultz, and B. Holzapfel. YBCO thin films prepared by fluorine-free polymer-based chemical solution deposition. *IEEE transactions on applied superconductivity*, 15(2):2642–2644, 2005.
- [42] Y. Xu, A. Goyal, N. A. Rutter, D. Shi, M. Paranthaman, S. Sathya-murthy, P. M. Martin, and D. M. Kroeger. Fabrication of high-critical current density YBa₂Cu₃O_{7-δ} films using a fluorine-free sol gel approach. *Journal of materials research*, 18(3):677–681, 2003.
- [43] F. F. Lange. Chemical solution routes to single-crystal thin films. *Science*, 273(5277):903–909, 1996.
- [44] M. Vilardell, J. Fornell, J. Sort, R. Vlad, J. C. Fernández, J. Puig, A. Usoskin, A. Palau, T. Puig, and X. *others*. Obradors. Inkjet-Printed

- Chemical Solution Y₂O₃ Layers for Planarization of Technical Substrates. *Coatings*, 7(12):227, 2017.
- [45] H. Schmidt. Film Preparation by Inorganic-Organic Sol-Gel Synthesis. *MRS Proceedings*, 121:743–755, 1988.
- [46] H. Kozuka and M. Kajimura. Single-Step Dip Coating of Crack-Free BaTiO₃ Films > 1 μ m Thick: Effect of Poly (vinylpyrrolidone) on Critical Thickness. *Journal of the American Ceramic Society*, 83(5):1056–1062, 2000.
- [47] A Llordés i Gill. *Superconducting nanocomposite films grown by chemical solution deposition: synthesis, microstructure and properties*. PhD thesis, 2010.
- [48] B. Derby. Inkjet printing of functional and structural materials: fluid property requirements, feature stability, and resolution. *Annual Review of Materials Research*, 40:395–414, 2010.
- [49] M. Vilardell. *Inkjet printing : a flexible manufacturing of functional ceramic coatings by Chemical Solution Deposition*. PhD thesis, 2014.
- [50] B. J. de Gans, P. C. Duineveld, and U. S. Schubert. Inkjet printing of polymers: State of the art and future developments. *Advanced Materials (Weinheim, Germany)*, 16(3):203–213, 2004.
- [51] A. Teichler, J. Perelaer, and U. S. Schubert. Inkjet printing of organic electronics - comparison of deposition techniques and state-of-the-art developments. *Journal of Materials Chemistry C*, 1(10):1910, 2013.
- [52] I. Van Driessche, J. Feys, S. C. Hopkins, P. Lommens, X. Granados, B. A. Glowacki, S. Ricart, B. Holzapfel, M. Vilardell, A. Kirchner, and others. Chemical solution deposition using ink-jet printing for YBCO coated conductors. *Superconductor Science and Technology*, 25(6):065017, 2012.
- [53] S. Magdassi and others. *The chemistry of inkjet inks*. World scientific Singapore, 2010.

- [54] I. Hutchings, T. Tuladhar, M. Mackley, D. Vaddillo, S. Hoath, and G. Martin. Links between ink rheology, drop-on-demand jet formation, and printability. *Journal of Imaging Science and Technology*, 53(4):41208–1, 2009.
- [55] B. Derby. Inkjet printing ceramics: From drops to solid. *Journal of the European Ceramic Society*, 31(14):2543–2550, 2011.
- [56] R. D. Deegan, O. Bakajin, T. F. Dupont, G. Huber, S. R. Nagel, and T. A. Witten. Capillary flow as the cause of ring stains from dried liquid drops. *Nature*, 389(6653):827–829, 1997.
- [57] B. M. Weon and J. H. Je. Fingering inside the coffee ring. *Physical Review E*, 87(1):013003, 2013.
- [58] K. L. Maki and S. Kumar. Fast evaporation of spreading droplets of colloidal suspensions. *Langmuir : the ACS journal of surfaces and colloids*, 27(18), 2011.
- [59] R. G. Larson. Re-shaping the coffee ring. *Angewandte Chemie (International ed. in English)*, 51(11):2546–8, 2012.
- [60] M. A. Fardad, E. M. Yeatman, E. J. C. Dawnay, M. Green, and F. Horowitz. Effects of H₂O on structure of acid-catalysed SiO₂ sol-gel films. *Journal of Non-Crystalline Solids*, 183(3):260–267, 1995.
- [61] G. W. Scherer. Sintering of sol-gel films. *Journal of Sol-Gel Science and Technology*, 8(1-3):353–363, 1997.
- [62] K. Zalamova, N. Roma, A. Pomar, S. Morlens, T. Puig, A. E. Carrillo, F. Sandiumenge, S. Ricart, and X. Obradors. Smooth Stress Relief of Trifluoroacetate Metal-Organic Solutions for YBa₂Cu₃O₇ Film Growth. *Chem. mater*, 18(14):5897–5906, 2006.
- [63] C. J. Brinker and G. W. Scherer. *Sol-gel science: the physics and chemistry of sol-gel processing*, volume 8. 1990.
- [64] H. Kozuka. Stress evolution on gel-to-ceramic thin film conversion. *Journal of Sol-Gel Science and Technology*, 40(2-3):287–297, 2006.

- [65] K. Ohno, H. Uchiyama, and H. Kozuka. Understanding of the development of in-plane residual stress in sol-gel-derived metal oxide thin films. *Journal of Applied Physics*, 111(1):014901, 2012.
- [66] X. Obradors, T. Puig, S. Ricart, M. Coll, J. Gázquez, A. Palau, and X. Granados. Growth, nanostructure and vortex pinning in superconducting $\text{YBa}_2\text{Cu}_3\text{O}_7$ thin films based on trifluoroacetate solutions. *Superconductor Science and Technology*, 25(12):123001, 2012.
- [67] Y. Yamamoto, K. Kamiya, and S. Sakka. Study on the properties of coating films prepared from metal alkoxides. *Yogyo Kyokaiishi*, 90(6):328–333, 1982.
- [68] M. P. Siegal, P. G. Clem, J. T. Dawley, R. J. Ong, M. A. Rodriguez, and D. L. Overmyer. All solution-chemistry approach for $\text{YBa}_2\text{Cu}_3\text{O}_{7-x}$ coated conductors. *Applied physics letters*, 80(15):2710–2712, 2002.
- [69] R. W. Hoffman. Mechanical properties of non-metallic thin films. In *Physics of nonmetallic thin films*, pages 273–353. Springer, 1976.
- [70] M. F. Doerner and W. D. Nix. Stresses and deformation processes in thin films on substrates. *Critical Reviews in Solid State and Material Sciences*, 14(3):225–268, 1988.
- [71] H. Windischmann. Intrinsic stress in sputter-deposited thin films. *Critical Reviews in Solid State and Material Sciences*, 17(6):547–596, 1992.
- [72] G. Janssen. Stress and strain in polycrystalline thin films. *Thin Solid Films*, 515(17):6654–6664, 2007.
- [73] M. W. Rupich, X. Li, S. Sathyamurthy, C. L. H. Thieme, K. DeMornville, J. Gannon, and S. Fleshler. Second Generation Wire Development at AMSC. *IEEE Transactions on Applied Superconductivity*, 23(3):6601205–6601205, 2013.
- [74] M. Vilardell, X. Granados, S. Ricart, I. Van Driessche, A. Palau, T. Puig, and X. Obradors. Flexible manufacturing of functional ceramic coatings by inkjet printing. *Thin Solid Films*, 548:489–497, 2013.

- [75] W. T. Wang, M. H. Pu, W. W. Wang, H. Zhang, C. H. Cheng, and Y. Zhao. High performance GdBa₂Cu₃O_{7-z} film preparation by non-fluorine chemical solution deposition approach. *Physica C: Superconductivity and its applications*, 471(21-22):951–955, 2011.
- [76] M. C. Fuertes and *others*. Sorption properties of mesoporous multilayer thin films. *The Journal of Physical Chemistry C*, 112(9):3157–3163, 2008.
- [77] M. H. Bartl, S. W. Boettcher, K. L. Frindell, and G. D. Stucky. 3-D molecular assembly of function in titania-based composite material systems. *Accounts of chemical research*, 38(4):263–271, 2005.
- [78] C. M. Stafford and *others*. A buckling-based metrology for measuring the elastic moduli of polymeric thin films. *Nature materials*, 3(8):545, 2004.
- [79] S. P. Lacour, S. Wagner, Z. Huang, and Z. Suo. Stretchable gold conductors on elastomeric substrates. *Applied physics letters*, 82(15):2404–2406, 2003.
- [80] M. Watanabe, H. Shirai, and T. Hirai. Wrinkled polypyrrole electrode for electroactive polymer actuators. *Journal of Applied Physics*, 92(8):4631–4637, 2002.
- [81] D. H. Kim and *others*. Stretchable and foldable silicon integrated circuits. *Science*, 320(5875):507–511, 2008.
- [82] T. Izumi and K. Nakaoka. Control of artificial pinning centers in REBCO coated conductors derived from the trifluoroacetate metal-organic deposition process. *Superconductor Science and Technology*, 31(3):034008, 2018.
- [83] N. Krins, M. Faustini, B. Louis, and D. Grosso. Thick and crack-free nanocrystalline mesoporous TiO₂ films obtained by capillary coating from aqueous solutions. *Chemistry of Materials*, 22(23):6218–6220, 2010.
- [84] L. Wang, W. Ren, K. Yao, P. Shi, X. Wu, and X. Yao. Effects of thickness on structures and electrical properties of K_{0.5}Na_{0.5}NbO₃ thick films derived from polyvinylpyrrolidone-modified chemical solution. *Ceramics International*, 38(SUPPL. 1):S291–S294, 2012.

- [85] Y. Yeshurun and A. P. Malozemoff. Giant flux creep and irreversibility in an Y-Ba-Cu-O crystal: an alternative to the superconducting-glass model. *Physical review letters*, 60(21):2202, 1988.
- [86] G. M. Shin, K. P. Ko, K. J. Song, S. H. Moon, and S. I. Yoo. High-IC YBCO films fabricated by the MOD process. *Physica C: Superconductivity*, 468(15-20):1567–1570, 2008.
- [87] R. T. Morrison and R. N. Boyd. Organic chemistry, 6th, 1992.
- [88] D. Jang, D. Kim, and J. Moon. Influence of fluid physical properties on ink-jet printability. *Langmuir*, 25(5):2629–2635, 2009.
- [89] Y. Rotenberg, L. Boruvka, and A. W. Neumann. Determination of surface tension and contact angle from the shapes of axisymmetric fluid interfaces. *Journal of colloid and interface science*, 93(1):169–183, 1983.
- [90] S. H. Anastasiadis, J. K. Chen, J. T. Koberstein, A. F. Siegel, J. E. Sohn, and J. A. Emerson. The determination of interfacial tension by video image processing of pendant fluid drops. *Journal of colloid and interface science*, 119(1):55–66, 1987.
- [91] A. Calleja, S. Ricart, X. Palmer, R. F. Luccas, T. Puig, and X. Obradors. Water determination of precursor solutions with oxidant cations by the Karl Fischer method: the YBCO-TFA case. *Journal of sol-gel science and technology*, 53(2):347–352, 2010.
- [92] B. J. Kang and J. H. Oh. Geometrical characterization of inkjet-printed conductive lines of nanosilver suspensions on a polymer substrate. *Thin Solid Films*, 518(10):2890–2896, 2010.
- [93] S. Bueble, K. Knorr, E. Brecht, and W. W. Schmahl. Influence of the ferroelastic twin domain structure on the {100} surface morphology of LaAlO₃ HTSC substrates. *Surface science*, 400(1-3):345–355, 1998.
- [94] E. M. Liston. Plasma treatment for improved bonding: a review. *The Journal of Adhesion*, 30(1-4):199–218, 1989.

- [95] M. Tomitori and T. Arai. Tip cleaning and sharpening processes for noncontact atomic force microscope in ultrahigh vacuum. *Applied surface science*, 140(3-4):432–438, 1999.
- [96] P. C. McIntyre, M. J. Cima, and M. F. Ng. Metalorganic deposition of high- J_C YBa₂YCu₃O_{7-x} thin films from trifluoroacetate precursors onto (100) SrTiO₃. *Journal of applied physics*, 68(8):4183–4187, 1990.
- [97] J. Farjas, J. Camps, P. Roura, S. Ricart, T. Puig, and X. Obradors. The thermal decomposition of barium trifluoroacetate. *Thermochimica Acta*, 544:77–83, 2012.
- [98] E. Pretsch, P. Buehlmann, C. Affolter, E. Pretsch, P. Buehlmann, and C. Affolter. *Structure determination of organic compounds*. Springer, 2000.
- [99] M. Born and E. Wolf. *Principles of Optics*. Cambridge University Press, 1999.
- [100] B. Poon, D. Rittel, and G. Ravichandran. An analysis of nanoindentation in linearly elastic solids. *International Journal of Solids and Structures*, 45(24):6018–6033, 2008.
- [101] H. Brenner. The slow motion of a sphere through a viscous fluid towards a plane surface. *Chemical engineering science*, 16(3-4):242–251, 1961.
- [102] L. A. Giannuzzi and F. A. Stevie. A review of focused ion beam milling techniques for tem specimen preparation. *Micron*, 30(3):197–204, 1999.
- [103] B. B. He. *Two-dimensional X-ray diffraction*. John Wiley & Sons, 2011.
- [104] R. C. Jaklevic, J. Lambe, A. H. Silver, and J. E. Mercereau. Quantum interference effects in josephson tunneling. *Physical Review Letters*, 12(7):159, 1964.
- [105] C. P. Bean. Magnetization of hard superconductors. *Physical review letters*, 8(6):250, 1962.
- [106] A. L. Yarin. *drop impact dynamics : splashing, spreading, receding, bouncing Annu. Rev. Fluid Mech.*, 38:159–192, 2006.

- [107] Y. Son, C. Kim, D. H. Yang, and D. J. Ahn. Spreading of an inkjet droplet on a solid surface with a controlled contact angle at low weber and reynolds numbers. *Langmuir*, 24(6):2900–2907, 2008.
- [108] J. E. Fromm. A numerical study of drop-on-demand ink jets. *2d International Colloquium on Drops and Bubbles*, pages 54–62, 1982.
- [109] S. Magdassi. *The Chemistry of Inkjet Inks*. World Scientific, 2009.
- [110] A. Atkinson and R. M. Guppy. Mechanical stability of sol-gel films. *Journal of materials science*, 26(14):3869–3873, 1991.
- [111] Brian Derby. Inkjet Printing of Functional and Structural Materials: Fluid Property Requirements, Feature Stability, and Resolution. *Annual Review of Materials Research*, 40(1):395–414, 2010.
- [112] M. Vilardell, X. Granados, S. Ricart, A. Calleja, A. Palau, T. Puig, and X. Obradors. Patterning of Functional Ceramic Oxides on Metallic Substrates by Inkjet Printing. In *NIP & Digital Fabrication Conference*, volume 2013, pages 503–507. Society for Imaging Science and Technology, 2013.
- [113] X. Granados, S. Ricart, R. Cobas, M. Vilardell, M. Arjona, T. Puig, X. Obradors, S. Hopkins, and B. Glowacki. Ink-jet printing for ceramic functional coating. In *NIP & Digital Fabrication Conference*, volume 2010, pages 194–197. Society for Imaging Science and Technology, 2010.
- [114] J. B. Szczech, C. M. Megaridis, D. R. Gamota, and J. Zhang. Fine-line conductor manufacturing using drop-on demand PZT printing technology. *IEEE transactions on electronics packaging manufacturing*, 25(1):26–33, 2002.
- [115] H. Y. Gan, X. Shan, T. Eriksson, B. K. Lok, and Y. C. Lam. Reduction of droplet volume by controlling actuating waveforms in inkjet printing for micro-pattern formation. *Journal of micromechanics and microengineering*, 19(5):055010, 2009.
- [116] J. Eggers and E. Villermaux. Physics of liquid jets. *Reports on progress in physics*, 71(3):036601, 2008.

- [117] H. Dong, W. W. Carr, and J. F. Morris. An experimental study of drop-on-demand drop formation. *Physics of fluids*, 18(7):072102, 2006.
- [118] J. E. Fromm. Numerical calculation of the fluid dynamics of drop-on-demand jets. *IBM Journal of Research and Development*, 28(3):322–333, 1984.
- [119] P. J. Smith, D.Y. Shin, J. E. Stringer, B. Derby, and N. Reis. Direct ink-jet printing and low temperature conversion of conductive silver patterns. *Journal of Materials Science*, 41(13):4153–4158, 2006.
- [120] C. D. Stow and M. G. Hadfield. An experimental investigation of fluid flow resulting from the impact of a water drop with an unyielding dry surface. *Proceedings of the Royal Society of London A: Mathematical, Physical and Engineering Sciences*, 373(1755):419–441, 1981.
- [121] M. Pasandideh-Fard, Y. M. Qiao, S. Chandra, and J. Mostaghimi. Capillary effects during droplet impact on a solid surface. *Physics of fluids*, 8(3):650–659, 1996.
- [122] D. B. van Dam and C. Le Clerc. Experimental study of the impact of an ink-jet printed droplet on a solid substrate. *Physics of Fluids*, 16(9):3403–3414, 2004.
- [123] S. Schiaffino and A. A. Sonin. Formation and stability of liquid and molten beads on a solid surface. *Journal of Fluid Mechanics*, 343:95–110, 1997.
- [124] G. Ström, M. Fredriksson, and P. E. R. Stenius. Contact angles, work of adhesion, and interfacial tensions at a dissolving hydrocarbon surface. *Journal of colloid and interface science*, 119(2):352–361, 1987.
- [125] W. Ristenpart, P. Kim, C. Domingues, J. Wan, and H. Stone. Influence of Substrate Conductivity on Circulation Reversal in Evaporating Drops. *Physical Review Letters*, 99(23):234502, 2007.
- [126] E. Adachi, A. S Dimitrov, and K. Nagayama. Stripe patterns formed on a glass surface during droplet evaporation. *Langmuir*, 11(4):1057–1060, 1995.

- [127] P. J. Yunker, T. Still, M. Lohr, and G. Yodh. Suppression of the coffee-ring effect by shape-dependent capillary interactions. *Nature*, 476(7360):308–11, 2011.
- [128] H. Hu and R. G. Larson. Marangoni effect reverses coffee-ring depositions. *The journal of physical chemistry. B*, 110(14):7090–4, 2006.
- [129] P. C. Duineveld and *others*. Ink-jet printing of polymer light-emitting devices. In *Organic Light-Emitting Materials and Devices V*, volume 4464, pages 59–68. International Society for Optics and Photonics, 2002.
- [130] K. Tada, J. Yoshida, N. Mori, K. Yamada, R. Teranishi, M. Mukaida, T. Kiss, M. Inoue, Y. Shiohara, T. Izumi, J. Matsuda, and K. Nakaoka. Growth process of Ba-poor YBCO film fabricated by TFA-MOD process. *Physica C: Superconductivity and its Applications*, 468:1554–1558, 2008.
- [131] Y. Chen, W. Bian, W. Huang, X. Tang, G. Zhao, L. Li, N. Li, W. Huo, J. Jia, and C. You. High Critical Current Density of $\text{YBa}_2\text{Cu}_3\text{O}_{7-x}$ Superconducting Films Prepared through a DUV-assisted Solution Deposition Process. *Scientific reports*, 6:38257, 2016.
- [132] I. Bretos, R. Jiménez, J. Ricote, and M. L. Calzada. Low-temperature crystallization of solution-derived metal oxide thin films assisted by chemical processes. *Chemical Society Reviews*, 2018.
- [133] K. Nakaoka, R. Yoshida, K. Kimura, T. Kato, Y. Usui, T. Izumi, and Y. Shiohara. Another approach for controlling size and distribution of nanoparticles in coated conductors fabricated by the TFA-MOD method. *Superconductor Science and Technology*, 30(5):055008, 2017.
- [134] T. Niwa, Y. Shiohara, and *others*. Calcining conditions for $\text{YBa}_2\text{Cu}_3\text{O}_{7-x}$ films by metalorganic deposition using trifluoroacetates. *IEEE transactions on applied superconductivity*, 13(2):2747–2750, 2003.
- [135] T. Araki and I. Hirabayashi. Review of a chemical approach to $\text{YBa}_2\text{Cu}_3\text{O}_{7-x}$ -coated superconductors-metalorganic deposition using trifluoroacetates. *Superconductor Science and Technology*, 16(11):R71, 2003.

- [136] T. Honjo, Y. Nakamura, Y. Shiohara, Y. Iijima, and *others*. Fabrication and growth mechanism of YBCO coated conductors by TFA-MOD process. *Physica C: Superconductivity*, 392:873–881, 2003.
- [137] D. E. Wesolowski, M. Yoshizumi, and M. J. Cima. Trajectory-property relationships in MOD-derived YBCO films. *Physica C: Superconductivity and its applications*, 450(1-2):76–82, 2006.
- [138] T. Schneller, R. Waser, M. Kosec, and D. Payne. *Chemical solution deposition of functional oxide thin films*. Springer, 2013.
- [139] N. Bowden, S. Brittain, and A. G. Evans. Spontaneous formation of ordered structures in thin films of metals supported on an elastomeric polymer. *Nature*, 393:146–149, 1998.
- [140] A. L. Volynskii, S. Bazhenov, O. V. Lebedeva, and N. F. Bakeev. Mechanical buckling instability of thin coatings deposited on soft polymer substrates. *Journal of Materials Science*, 35(3):547–554, 2000.
- [141] Y. Shi, A. H. Bork, S. Schweiger, and J. L. M. Rupp. The effect of mechanical twisting on oxygen ionic transport in solid-state energy conversion membranes. *Nat Mater*, 14(7):721–727, 2015.
- [142] C. Harrison, C. M. Stafford, W. Zhang, and A. Karim. Sinusoidal phase grating created by a tunably buckled surface. *Applied Physics Letters*, 85(18):4016–4018, 2004.
- [143] H. Jiang, D. Y. Khang, J. Song, Y. Sun, Y. Huang, and J. A. Rogers. Finite deformation mechanics in buckled thin films on compliant supports. *Proceedings of the National Academy of Sciences*, 104(40):15607–15612, 2007.
- [144] A. Llordés, K. Zalamova, S. Ricart, A. Palau, A. Pomar, T. Puig, A. Hardy, M. K. Van Bael, and X. Obradors. Evolution of Metal-Trifluoroacetate Precursors in the Thermal Decomposition toward High-Performance $\text{YBa}_2\text{Cu}_3\text{O}_7$ Superconducting Films. *Chemistry of Materials*, 22(5):1686–1694, 2010.

- [145] L. A. Chow, B. Dunn, K. N. Tu, and C. Chiang. Mechanical properties of xerogel silica films derived from stress versus temperature and cracking experiments. *Journal of Applied Physics*, 87(11):7788–7792, 2000.
- [146] S. Morlens, N. Roma, S. Ricart, A. Pomar, T. Puig, and X. Obradors. Thickness control of solution deposited YBCO superconducting films by use of organic polymeric additives. *Journal of materials research*, 22(8):2330–2338, 2007.
- [147] V. R. Vlad, K. Zalamova, M. Coll, A. Pomar, A. Palau, J. Gutierrez, T. Puig, X. Obradors, and A. Usoskin. Growth of Chemical Solution Deposited $^{TFA}YBCO/^{MOD}(Ce,Zr)O_2/^{ABAD}YSZ/SS$ Coated Conductors. *IEEE Transactions on Applied Superconductivity*, 19(3):3212–3215, 2009.
- [148] P. Cayado, M. Erbe, S. Kauffmann-Weiss, C. Bühler, A. Jung, J. Hänisch, and B. Holzapfel. Large critical current densities and pinning forces in CSD-grown superconducting $GdBa_2Cu_3O_{7-x}BaHfO_3$ nanocomposite films. *Superconductor Science and Technology*, 30(9):094007, 2017.
- [149] G. W. Scherer. Recent progress in drying of gels. *Journal of non-crystalline solids*, 147:363–374, 1992.
- [150] X. Li and B. Bhushan. A review of nanoindentation continuous stiffness measurement technique and its applications. *Materials characterization*, 48(1):11–36, 2002.
- [151] W. C. Oliver and G. M. Pharr. An improved technique for determining hardness and elastic modulus using load and displacement sensing indentation experiments. *Journal of materials research*, 7(6):1564–1583, 1992.
- [152] L. Morales, J. Parlange, M. Wu, F. J. Pe, W. Zhang, W. Sang, and T. S. Steenhuis. Surfactant-Mediated Control of Colloid Pattern Assembly and Attachment Strength in Evaporating Droplets Vero n. *Langmuir*, 2013.
- [153] E. Tekin, B. J. de Gans, and U. S. Schubert. Ink-jet printing of polymers—from single dots to thin film libraries. *Journal of Materials Chemistry*, 14(17):2627–2632, 2004.

- [154] L. Cui, J. Zhang, X. Zhang, L. Huang, Z. Wang, Y. Li, H. Gao, S. Zhu, T. Wang, and B. Yang. Suppression of the coffee ring effect by hydrosoluble polymer additives. *ACS Applied Materials and Interfaces*, 4(5):2775–2780, 2012.
- [155] D. Zhai, T. Zhang, J. Guo, X. Fang, and J. Wei. Water-based ultraviolet curable conductive inkjet ink containing silver nano-colloids for flexible electronics. *Colloids and Surfaces A: Physicochemical and Engineering Aspects*, 424:1–9, 2013.
- [156] T. Robert. "green ink in all colors" - Printing ink from renewable resources. *Progress in Organic Coatings*, 78:287–292, 2015.
- [157] M. Miura, H. Ichikawa, Y. Sutoh, K. Nakaoka, M. Yoshizumi, Y. Yamada, T. Izumi, and Y. Shiohara. Development of multi-turn reel-to-reel crystallization large furnace for high production rate of YBa₂Cu₃O_ycoated conductors derived from TFA-MOD process. *Physica C: Superconductivity and its Applications*, 469(15-20):1336–1340, 2009.
- [158] A. Llordes, A. Palau, J. Gázquez, M. Coll, R. Vlad, A. Pomar, J. Arbiol, R. Guzmán, S. Ye, V. Rouco, F. Sandiumenge, S. Ricart, T. Puig, M. Varela, D. Chateigner, J. Vanacken, J. Gutiérrez, V. Moshchalkov, G. Deutscher, C. Magen, and X. Obradors. Nanoscale strain-induced pair suppression as a vortex-pinning mechanism in high-temperature superconductors. *Nature materials*, 11(4):329–36, 2012.
- [159] M. Coll, R. Guzman, P. Garcés, J. Gazquez, V. Rouco, A. Palau, and *others*. Size-controlled spontaneously segregated Ba₂YTaO₆ nanoparticles in YBa₂Cu₃O₇ nanocomposites obtained by chemical solution deposition. *Superconductor Science and Technology*, 27(4):044008, 2014.
- [160] P. Cayado, K. De Keukeleere, A. Garzón, L. Perez-Mirabet, A. Meledin, J. De Roo, F. Vallés, B. Mundet, H. Rijckaert, G. Pollefeyt, and *others*. Epitaxial YBa₂Cu₃O_{7-x} nanocomposite thin films from colloidal solutions. *Superconductor Science and Technology*, 28(12):124007, 2015.
- [161] A. Palau, F. Valles, V. Rouco, M. Coll, Z. Li, C. Pop, B. Mundet, J. Gazquez, R. Guzman, J. Gutierrez, X. Obradors, and T. Puig. Dis-

- entangling vortex pinning landscape in chemical solution deposition superconducting $\text{YBa}_2\text{Cu}_3\text{O}_{7-x}$ films and nanocomposites. *Superconductor Science and Technology*, 2018.
- [162] C. Pop, B. Villarejo, F. Pino, B. Mundet, S. Ricart, M. de Palau, T. Puig, and X. Obradors. Growth of all-chemical high critical current $\text{YBa}_2\text{Cu}_3\text{O}_{7-\delta}$ thick films and coated conductors. *Superconductor Science and Technology*, Manuscript accepted for publication on 2018.